CHALMERS

Monte-Carlo Simulations of Nuclear Reactions at
Relativistic Energies

Bachelor Thesis in Engineering Physics

STEFAN BULLER
JOEL MAGNUSSON
TORBJÖRN RATHSMAN

Department of Fundamental Physics
CHALMERS UNIVERSITY OF TECHNOLOGY
Gothenburg, Sweden 2013

Monte-Carlo Simulations of Nuclear Reactions at Relativistic Energies

BACHELOR THESIS

BY

Stefan Buller, Joel Magnusson, and Torbjörn Rathsman

SUPERVISORS:

Andreas Heinz
Håkan Johansson
Ronja Thies

EXAMINERS:

Christian Forssén
Daniel Persson

Department of Fundamental Physics
Chalmers University of Technology
Gothenburg, Sweden 2013

Cover: An event created by using GGLAND. A ^{14}B nucleus is fired into a partial setup of the *S393* experiment. The colour coding is as follows: traces of electrons (e$^-$) are red, positrons (e$^+$) blue, photons (γ) green, protons (p) cyan, neutrons (n) yellow and pions (π) magenta. Traces of all other particles are gray.

Abstract

This thesis describes Monte-Carlo simulations of the *S393* light exotic-ion beam experiment that was carried out at GSI Helmholtz Centre for Heavy Ion Research, using the simulation software GEANT4 via the wrapper program GGLAND. Specifically, it focuses on the fragment arm of the detector setup in Cave C and the ability of the RALF'S TRACKER software to track and identify simulated ions.

Two separate cases are considered. Firstly, the trackers ability to identify particles ejected forward along the beam-axis with incorrect information of the magnetic field in ALADiN (A LArge DIpole magNet). Secondly, the trackers ability to identify particles ejected with an angle α from the beam-axis is studied. The simulations were carried out by firing single, neutron rich $4 \leq Z \leq 9$ nuclei with a magnetic rigidity of $8.8\,\mathrm{Tm}$ from the target location, corresponding to particles bending off along the fragment arm at a $15°$ deflection angle.

It is found that the tracker, calibrated in accordance with a predescribed routine[1], is able to correct for the incorrect magnetic field by effectively rotating the fragment arm for the cases simulated. The resulting errors are small enough as not to affect identification of the simulated ions. The tracker is also able to identify most particles fired at an angle α as long as all detectors along the trajectory are hit. The size of the GFIs (Großer FIber detektor) is the first limiting factor for detecting particles with $\alpha \gtrsim 2.5°$. However, some non-geometric effects cause some particles to miss the TFW (Time of Flight Wall) at roughly the same angle. These effects remain unidentified.

In addition, the geometry of detectors defined in GGLAND together with algebraic approximations for, in the simulations, choosing an appropriate magnetic rigidity for a given ALADiN current and for determining the charge of particles, given the energy deposits in the TFW, are presented in appendices.

Sammandrag

Denna tes beskriver Monte-Carlo simuleringar av *S393*-experimentet utfört på *GSI Helmholtz Centre for Heavy Ion Research* med en stråle av lätta exotiska nuklider, utnyttjande simulerings-mjukvaran GEANT4 genom wrapper-programmet GGLAND. Fokus ligger på fragmentarmen hos detektoruppställningen i *Cave C* och förmågan hos mjukvaran RALF'S TRACKER att spåra och identifiera simulerade joner.

Två separata fall har undersökts. Det första av dessa är trackerns förmåga att identifiera partiklar utskjutna framåt längs strålaxeln då den matas med felaktig information om ALADiNs (A LArge DIpole magNet) magnetfält. Det andra fallet är trackerns förmåga att identifiera partiklar som skjutits ut med en vinkel α från strålaxeln. Simuleringarna utfördes med enskilda, neutronrika $4 \leq Z \leq 9$ nuklider med en magnetisk rigiditet på $8.8\,\mathrm{Tm}$, avfyrade från strålmålets position. Med denna magnetiska rigiditet böjdes jonerna av längs med fragmentarmen, med en avböjningsvinkel på $15°$.

Resultaten är att trackern, kalibrerad för fragment enligt en föreskriven rutin[1], kan korrigera för ett felaktigt magnetfält genom att effektivt rotera fragmentarmen för de fallen som simulerats. De resulterande felen är små nog att inte påverka identifieringen av den avfyrade jonen. Trackern identifierar även stora delar av partiklar avfyrade med en vinkel α, såvida alla detektorer träffas. Storleken på GFI:erna (Großer FIber detektor) fanns vara den första begränsande faktorn för att detektera partiklar med $\alpha \gtrsim 2.5°$, men oidentifierade icke-geometriska effekter får vissa partiklar att missa TFW:n (Time of Flight Wall) vid ungefär samma vinkel.

Utöver detta presenteras, i appendix, geometri för detektorer definerade i GGLAND samt med algebraiska approximationer för att, i simuleringar, välja ett lämpligt $b\rho$ för en given ALADiN ström och för att avgöra laddningen hos partiklar, givet energidepositioner i TFW:n.

---

[1] http://ralfplag.de/tracker/calibration/ (19-05-2013)

Acknowledgements

Contents

Notations Throughout the Report

Term	Type	Definition
$\boldsymbol{u},\boldsymbol{x},\boldsymbol{b}$	geometric object	Three-vectors
$\boldsymbol{U},\boldsymbol{X},\boldsymbol{P}$	geometric object	Four-vectors
$\boldsymbol{P},\boldsymbol{Q},\boldsymbol{N}$	physical quantity	Four-momentum
u,v,v', etc.	physical quantity	Speed
c	physical constant	The speed of light
E	physical quantity	Energy
p	physical quantity	Linear momentum
m,M	physical quantity	Mass
m_0,M_0	physical quantity	Rest mass, also known as invariant mass
m_e,m_X	physical quantity	Rest mass of the electron/particle "X"
Z	physical quantity	Atomic number, the number of protons in a nucleus
A	physical quantity	Mass number, the number of nucleons in a nucleus.
α	statistics	Acceptance, the ratio between the expectation value of observed events and the expectation value of all events
β	physical quantity	Beta, the quotient $\frac{v}{c}$
γ	particle	Gamma, a photon, a quantum of energy
γ	physical quantity	Lorentz gamma factor. $\gamma = (1 - v^2/c^2)^{-1/2}$
α	physical quantity	Opening angle, the angle between the particles initial direction and the beam axis.
$\boldsymbol{b}$	physical quantity	Magnetic field
T	physical quantity	Kinetic energy
θ, ϕ, φ	physical quantity	Angles; θ often being taken as the angle from the z-axis (the beam axis); φ often from the x-axis
ρ	physical quantity	Bending radius of a particle due to a magnetic field
$b\rho$	physical quantity	Magnetic rigidity of a particle. $b\rho = p/q$
I	physical quantity	Current
z	direction	The direction of the beam axis
y	direction	The direction towards the ceiling
x	direction	Direction chosen to yield a right-hand coordinate system together with y and z
q	physical quantity	Charge

1. Introduction

All of the elements around us are made out of atoms, consisting of electrons and different nuclei. These nuclei are in turn made out of nucleons, which have been bound to each other through fusion of lighter elements in astrophysical processes. While the stability of elements may be understood in terms of minimising energy, their relative abundance can only be understood by looking at how they were formed in these processes.

A large part of understanding how elements are synthesised is to determine how likely certain reactions are to take place. These likelihoods are often given in terms of cross sections, σ, defined by

$$\sigma = \frac{R}{N\Phi} \quad , \tag{1.1}$$

where Φ is the intensity of an incoming beam of particles ([number of particles]/[area $\times$ time]), R is the number of reactions r per unit of time and N is the amount of particles being illuminated by the beam. In order to measure σ, the numbers of reactions r have to be measured. If the reaction r results in a set of reaction products, this is often done in practice by detecting and counting these particles. To determine σ with absolute accuracy, each and every one of these particle of must be detected or otherwise accounted for.

In order to detect the results of various interactions, experimentalists have often come to rely on increasingly complex detector setups. This has the benefit of allowing more particles to be detected with increased resolution, but the additional data require more elaborate analysis techinques. Moreover, the physical quantities of interest may not be directly retrievable from the data of a single detector, and heuristic methods must be used to figure out which event in different detectors are caused by the same particle.

Nevertheless, it is not feasible to detect every single produced particle. In order to still be able to determine cross sections, the experimental setup needs to be evaluated to get a grasp on how often a particle is not detected.

To evaluate the experimental setup, the setup may be tested with known reactions. This makes the experiment take longer time and may not always reveal what actually happened. Another way to evaluate the setup is to simulate it by using computer programs. In this case, all particles can be traced, since the particle track is just represented by bits in readable memory. This difference is illustrated by Figure 1.1.

Once the experimental setup is evaluated, the ratio of the detected and undetected events, the acceptance α of the setup, may be used to compensate for the particles that

avoid detection. The acceptance may be formally defined as

$$\alpha = \frac{\mathrm{E[N_{detected\ events}]}}{\mathrm{E[N_{events}]}} \quad ,$$

(1.2)

where $\mathrm{E}[X]$ denotes the expected value of X [1]. Generally, the acceptance will depend on several variables, such as the momentum of the detected particle. Another thing to note is that since the relevant physical parameters for identifying certain particles only may be determined by extensive analysis of the experimental data, α must take the analysis methods into account.

1.1. Scope

This bachelor thesis describes Monte-Carlo simulations of parts of the *S393* experiment performed at *GSI Helmholtz Centre for Heavy Ion Research*, Darmstadt, Germany. The main focus has been on how well the analysis tools behave under different circumstances with single ions fired forward, from the target location, and with a magnetic rigidity (defined in Section 2.1.2) of 8.8 Tm when trying to calculate what kind of particle hit the detector. This information may then be used as a step towards determining the acceptance of the setup.

One part of the analysis chain is a tool used to evaluate particle paths and find their speed, mass, and charge. It has been investigated how many detector events it can identify correctly and if there are some situations when it will fail, by delivering an incorrect value. An important part of the experimental setup is a magnetic field, which causes charged particles to deviate from their original path.

One of the presented results is how the setup with analysis tools is able to detected and identify forward travelling ions depending on differences between the real magnetic field and the field used in the analysis. Another result is how the initial angle between the particles trajectory and the beam axis affects the amount of detected particles.

Apart from the aforementioned results, there are also results in the form of detector definitions, which was created in the scope of this project. These definitions have been thoroughly used in, and were crucial for, the simulations that generate the data that were eventually analysed.

Figure 1.1.: *By simulating the experiment, the experimental data can be related to the inputs of the simulation, giving a better understanding of the behaviour of the experimental setup. This in turn makes it easier to disentangle the underlying physics.*

1.2. Outline

In order to understand the experiment, a brief background in detector physics is necessary. A short introduction on that subject is found in Section 2. After that, in Section 3, the *S393* experiment is described detector by detector. Then follows a survey of the tools used for our simulations and analyses in Section 4 and, in Section 5, it is described how these tools were used. The results are presented in Section 6 and discussed in Section 7. Possible future investigations and challenges are discussed in the concluding section, Section 7.3.

2. Theoretical Background

In the following section, a few mechanisms useful for understanding the principles of radiation detection are presented. Section 2.1 provides a theoretical basis for understanding the principles behind certain detectors, which is the focus of Section 2.2.

2.1. Particle Interaction Processes

This section describes how particles interact with other particles and external fields. This is mostly done within the framework of special relativity and the underlying mechanics for the interactions are not considered.

2.1.1. Photons

The most common interaction processes of photons — photoelectric absorption, Compton scattering and pair production — are presented in this section. Different interaction processes dominate within different energy ranges, as seen in Figure 2.1. Pair production and Compton scattering both yield photons of lower energy, and therefore energetic photons are able to trigger a cascade of events, until the produced photons are at sufficiently low energy to be likely to be absorbed.

Photoelectric Absorption

A photon in the vicinity of an atom may be absorbed by transferring all of its energy to a bound electron. The probability for this to occur is highly dependent on the charge of the atomic nucleus and the shell of the electron, with more tightly bound electrons being more likely to receive the energy [3], and the interaction not occurring at all with free electrons. At sufficiently high energies, the electron is emitted from the atom.

Compton Scattering

Compton scattering is due to a photon scattering on a charged particle (often an electron). The energy of the photon after the collision, assuming the particle was initially at rest, can be expressed as

$$E' = \frac{E}{1 + \frac{E}{m_0 c^2}(1 - \cos\theta)} \quad ,$$
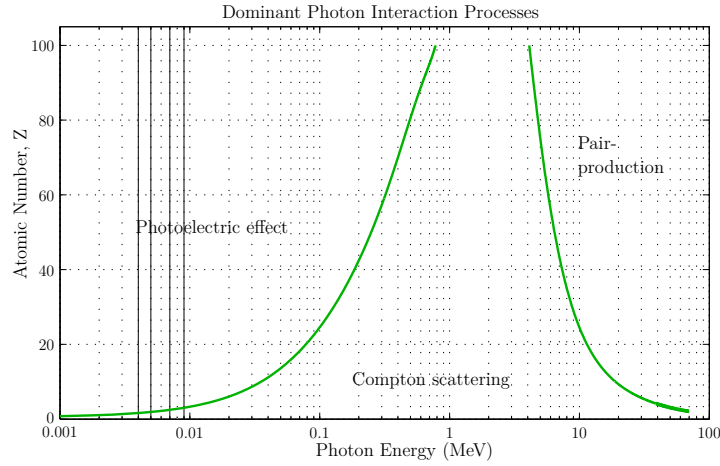
Figure 2.1.: *Representation of the relative predominance of the main photon interaction processes with an atom. Data were calculated using the NIST XCOM database [2].*

where E is the initial energy of the photon, m_0 is the rest mass of the particle initially at rest and θ is the scattering angle in the initial rest frame of the particle, as illustrated in Figure 2.2.

Pair Production

A photon with sufficient energy can in the presence of a nucleus spontaneously create an electron-positron pair, as illustrated in Figure 2.3. This may occur if

$$E > 2m_e c^2 \quad ,$$

where m_e is the rest mass of the electron (and positron), c the speed of light and M_N the rest mass of the nucleus. However, it is only at still higher energies, a few MeV, that pair production makes a notable contribution to the energy depositions of photons in matter, as can be seen in Figure 2.1. More detailed calculations take the binding energy of atomic electrons into account.

2.1.2. Charged particles

Bremsstrahlung

Bremsstrahlung is the result of acceleration or decaleration of a charged particle. As such, it occurs in the simulation when a particle is decelerated through interaction with other particles. For this case, a collision between a pair of particles is considered, in which an incoming particle gets decelerated and a photon is emitted. This can be understood from 4-momentum conservation. The energy of the emitted photon is given by

$$E = \frac{m_o M_o c^2 \left(\gamma(u) - \gamma(u')\gamma(v')(1 - u'v'\cos\theta/c^2) \right)}{M_0 + m_0\gamma(u)(1 - u\cos\phi/c)} \quad ,$$
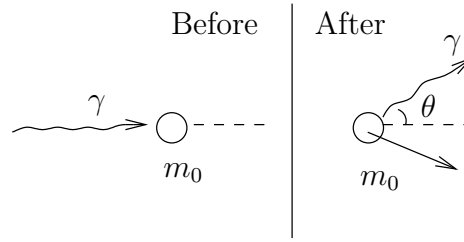
Figure 2.2.: *A photon is scattered by a massive particle initially at rest.*
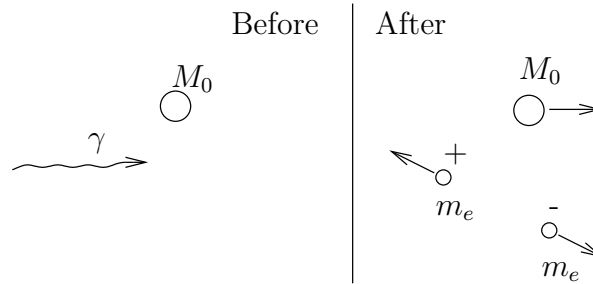
Figure 2.3.: *A photon creates an electron-positron pair near a stationary massive particle.*

with notations as in Figure 2.4 and with u' being the speed of the incoming particle and v' being the speed of the initially stationary particle, both after the collision.

Response to a Magnetic Field

A charged particle with a constant velocity $\boldsymbol{v}$ travelling in a magnetic field $\boldsymbol{b}$ will experience a force $\boldsymbol{f} = q\boldsymbol{v} \times \boldsymbol{b}$. Due to this force a particle moving with a velocity perpendicular to a homogeneous magnetic field, as illustrated in Figure 2.5, will be deflected in a circular arc with the radius ρ given by

$$\rho = \frac{T}{qbc}\sqrt{1 + \frac{2m_0c^2}{T}} \quad , \tag{2.1}$$

where T is the kinetic energy of the particle, q its charge, b the strength of the magnetic field, and m_0 its rest mass. Equation 2.1 can alternatively be written as

$$b\rho = \frac{p}{q}, \tag{2.2}$$

where $p = \gamma m_0 v$ is the momentum of the particle. From this it can be concluded that particles with the same $\frac{p}{q}$ will bend off with the same radius in a given homogenous magnetic field. For this reason, $\frac{p}{q}$ is known as the *magnetic rigidity* of a particle.

Another way of formulating Equation 2.1 is

$$\beta = \sqrt{\frac{(Zeb\rho)^2}{(Zeb\rho)^2 + (cm)^2}} \quad . \tag{2.3}$$
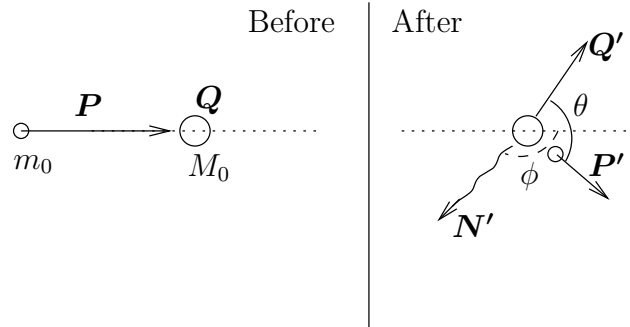
Figure 2.4.: *Deceleration and deflection of a charged particle with rest mass m_0, initial 4-momentum P and speed u. The angle θ is the angle between the directions of the two massive particles after the collision. The angle ϕ is the angle between the direction of the emitted photon and the original velocity of the incoming particle. Everything takes place in the original rest frame of the M_0 particle.*
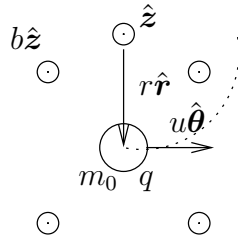
Figure 2.5.: *A particle with constant velocity moving through a magnetic field perpendicular to the plane of motion.*

Energy Loss of a Charged Particle Passing Through Matter

When a charged particle passes through matter, it excites or knocks nearby electrons into motion, whereas the several orders of magnitude heavier nuclei are mostly left unaffected. By conservation of energy, the charged particle loses energy equal to the energy given to the electrons. Since the interaction is mainly due to the Coulomb force, the particle continuously interacts with the surrounding matter. If the charged particle is much heavier than the electron, then the energy loss of the particle due to Coulomb interactions as a function of travelled distance through matter is given by the Bethe

formula

$$-\frac{\mathrm{d}E}{\mathrm{d}x} = \frac{4\pi}{m_e c^2} \frac{nz^2}{\beta^2} \left(\frac{e^2}{4\pi\epsilon_0}\right)^2 NZ \left[\ln\left(\frac{2m_e c^2 \beta^2}{I(1-\beta^2)}\right) - \beta^2\right] \quad , \qquad (2.4)$$

where β is the dimensionless speed relative to the speed of light, and ze is the charge of the particle. The parameters NZ is the charge density of the medium and I is the ionisation energy of the atoms in the medium. The Bethe formula is mainly valid for high energies and low z, which is the case in the *S393* experiment.

A consequence of charged particles passing through matter, and ionizing nearby atoms, is that the particles travelling through give rise to scores of freed electrons. These electrons will trace paths originating and branching off from the path of the original particle, but only rarely straying far from that path due to their low kinetic energy. However, among these are some with a sufficiently high energy to in turn ionize additional atoms. These more energetic electrons are referred to as δ-electrons, or δ-rays.

2.2. Detector Principles

The information about radiation detection found in this section is based on *Radiation detection and measurement* by G.F. Knoll [3].

It is often desirable to convert measured quantities into electronic signals, since those can easily be manipulated and later digitized. This can be achieved in various ways, depending on the properties of the particles to be detected.

Charged particles, like protons and ions, can be detected directly through their interactions with the active volume[1] of a detector [4]. On the other hand, uncharged particles, like neutrons, are detected indirectly when they interact with individual nuclei through the resulting motion of other (charged) particles [4].

2.2.1. Scintillators

In an inorganic crystalline scintillator, the valence electrons in the detector medium closest to the passing particle will occasionally get excited to a higher energy band [5]. The excited electrons will eventually return to the conduction band by spontaneous relaxation, with a photon being emitted in accordance to $\Delta E = \hbar\omega$. Due to additional energy levels between the bands, introduced by defects in the scintillator-material, electrons may deexcite in several steps, emitting photons with energies that are not able to excite electrons in the valence band and are thus unlikely to be absorbed. These photons can then be detected by photomultiplier-tubes (PM-tubes), producing an electric signal [5].

By conservation of energy, the charged particles passing the detector medium must deposit energy equal to the energy used to excite the electrons, whereby the energy deposition of the particle can be measured. These are the basic principles behind scintillation detectors [5].

---

[1]The active volume of a detector is the volume which is able to transforms energy deposits within itself into read-out signals.

The same principles apply to other types of scintillators as well, such as organic scintillators, where the energy-level structure of the molecules allows an excited molecule to emit photons not absorbable by molecules in the ground state [5].

3. The *S393* Experiment

The *S393* experiment is a nuclear physics experiment which was conducted at *GSI Helmholtz Centre for Heavy Ion Research* in 2010. Its purpose is to increase the knowledge about astrophysical reaction rates for the synthesis of neutron-rich nuclei and about the structure of the exotic nuclei in that region. In the experiment, unstable, neutron rich $4 \leq Z \leq 10$ nuclei were shot at light target nuclei. [6]

3.1. Source of Unstable Nuclei

The accelerator facility at GSI is illustrated in Figure 3.1. In order to produce a beam of unstable nuclei, stable ions are accelerated in a linear accelerator (UNILAC) before injection into a synchrotron accelerator *SIS* (SchwerIonenSynchrotron, heavy ion synchrotron). In SIS, the stable ions are accelerated to relativistic energies. After the ions have gained sufficient energy in the SIS, they are directed at a light, but thick, production target in the *FRS* (FRagment Separator). In *S393*, the stable ion of the beam was ^{40}Ar and the production target used was made of ^{9}Be with a density of $4.011\,\mathrm{g/cm^2}$ [8, 9].

The collisions in the FRS can result in many fragments. Among these fragments are the interesting unstable $4 \leq Z \leq 10$ nuclei. In order to filter out all but a specific kind of nuclei from the different fragments, a combination of magnetic fields and degraders are used [10]. The magnetic fields will filter out ions depending on their velocity and charge-to-mass ratio [10]. The degraders consist, in principle, of a layer of matter with adjustable thickness, allowing ions to be filtered depending on the energy lost in the material, in accordance with Equation 2.4 [10]. With this setup, ions with specific charge and mass can be selected from the fragments [10].

3.2. Cave C Setup

The experimental setup, as illustrated in Figure 3.2, is located in Cave C. Additional details about the geometry of the detectors can be found in Appendix C and on the *land02 unofficial site* [11].

Ions from the FRS are sent into Cave C, typically at energies on the order of a few hundred MeV/nucleon. As the ions enter Cave C, they hit the *POS* (POSition) detector, which starts a timer used to measure the velocity of the particles. It also stops a timer started in the FRS, which gives a measurement of the speed of the incoming particle.
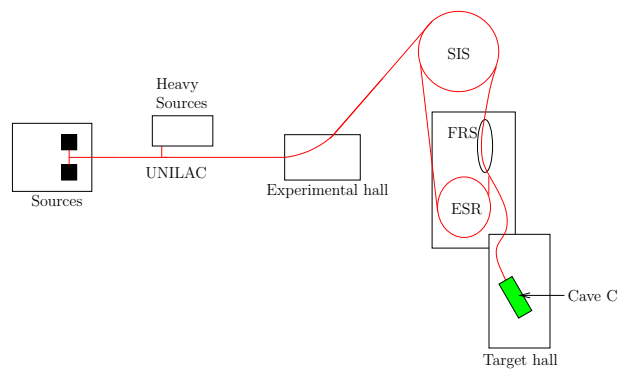
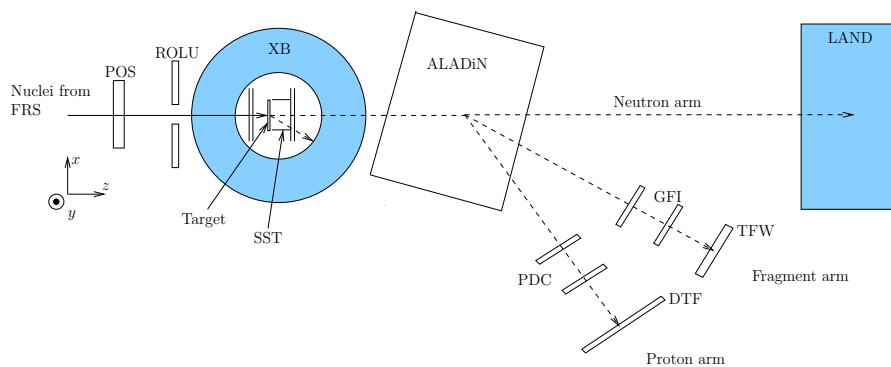Figure 3.1.: *A sketch of the accelerator facility at GSI [7].*

Figure 3.2.: *The experimental setup for* S393 *in Cave C at GSI [7]. The filled obstacles were already defined in* GGLAND *(see Section 4.2), while the others were implemented as part of this project.*

POS is a thin sheet of scintillator material with lightguides and PM-tubes at all four sides perpendicular to the ion-beam.

After the ion-beam has passed through POS, it passes through *ROLU* (Rechts, Oben, Links, Unten), which measures the spread[1] of the beam and can be used as a veto-trigger, that tells the data acquisition to reject coming events, if the beam particles are too far off the beam axis. ROLU consists of four plastic scintillators defining a rectangular opening. By moving the scintillators, the position and size of the opening can be adjusted, and only events related to ions passing through it are recorded and used for analysis.

After ROLU and POS, the ions arrive at the target located inside the *XB* (Crystal Ball) detector. The XB has a 4π-coverage with blind spots along the beam axis for the incoming beam and outgoing forward reaction products. The detector consists of 159 removable pentagonal and hexagonal NaI crystals placed in a spherical shell (there is room for 162 crystals, although 3 are removed). The XB is mainly used to detect photons and protons, since these often are emitted at large angles relative to the beam axis.

Inside XB are the *SSTs* (Silicon STrip detectors), consisting of planar silicon detectors divided into many sections by the segmentation of the read-out electrodes. There are eight of these detectors in total: two are positioned before the target to determine the angle of the incoming beam. Likewise, two are positioned behind the target determine the angle of the outgoing beam, whereas the remaining four surround the target in directions orthogonal to the beam axis.

The particles, resulting from the collisions with the target, that continue in the forward direction, may reach *ALADiN* (A LArge DIpole magNet). Inside this magnet, charged particles are bent in almost circular arcs due to a nearly-constant magnetic field in the y-direction, defined as pointing upwards, orthogonal to the floor. Although the field is almost constant within the magnet, there is a notable fringe-field, which simulations need to take into account. The actual magnetic field experienced by particles passing through ALADiN is presented in Section A.3. The field in ALADiN is used to separate different particles depending on their mass-to-charge ratio. Most particles entering ALADiN travel at approximately the same speed as the ions of the beam, which together with the mass-to-charge ratio and the magnetic field determines the path the particles take.

- **Proton arm:** Protons, which have a low mass-to-charge ratio, are heavily affected by the magnetic field and their paths are bent into the *PDCs* (Proton Drift Chamber). The PDCs are basically a collection of vertical and horizontal charged wires, generating an electric field, allowing charged particles to be detected by collecting freed electrons in their tracks. After passing through the PDCs, the protons hit the *DTF* (Dicke ToF-wall), a detector made out of scintillator-bars.

- **Fragment arm:** Heavier ions are bent to somewhere between LAND and the PDC, and hit the two *GFIs* (Großer FIberdetektor). A GFI is a collection of vertical scintillating fibers packed closely together into one layer. Around and

---

[1]The maximum angle between the beam axis and a particles trajectory.

between the fibers is a thin layer of wrapping material to keep the light from leaking into adjacent fibers.

After passing the GFIs, the ions hit the final detector, *TFW* (Time of Flight Wall), which consists of 2 planes. Each plane in turn consists of multiple vertical or horizontal paddles of scintillating material.

- **Neutron arm:** Neutrons, which are uncharged particles, are not affected by the magnetic field of ALADiN and thus continue forward into *LAND* (Large Area Neutron Detector) where they may be detected.

The final steps for all three paths measure the time since the incoming ion passed the POS-detector, which gives the speed of the particle. In real life, things are not always as simple as described above, as particles behave stochastically and may stray from their paths or interact with matter in an unintended way. This is one of the reasons why ROLU and other veto-triggers are in place. This is also why simulations need to be performed, to better understand the influence of these effects.

4. Simulation and Analysis Tools

When simulating a nuclear physics experiment like *S393*, there are primarily two software solutions available: FLUKA and GEANT. The software chosen for this project was GEANT. Reasons for this choice include the fact that the Subatomic Physics Group at Chalmers University of Technology has experience with GEANT, ease of acquiring the source-code and the more permissive license. GEANT4 was chosen over GEANT3 since GEANT4 is under active development, and as a consequence has more up-to-date physics models. A wrapper library and program called GGLAND was used to access the functionality of GEANT4.

After generating data using GGLAND, the data have to be analysed. This was done by using various tools including ROOT, RALF'S TRACKER and MATLAB.

4.1. GEANT

GEANT is a toolkit for Monte-Carlo simulations of particles [12]. Monte-Carlo simulations are stochastic methods for simulating physical processes using random numbers. Depending on the physical process, different probability distributions are used. Using a large set of data points, the method should converge to the expectation value in the same way as for the real process.

While GGLAND may be used both together with GEANT3 and GEANT4, this section focuses on details in GEANT4. Particle tracking (navigation) in GEANT4 is based on a tree structure of volumes. Such a structure is illustrated in Figure 4.1. The outermost volume is called the world volume. Within the world volume, a set of daughter volumes are declared and placed, which in turn may contain other daughter volumes [12]. A "shadow world" can also be specified where a set of daughter volumes can be declared correspondingly. GEANT4 will then, in addition to the physics and geometries of the world volume together with its sub volumes, also consider the boundaries of the shadow world. This is useful, since volumes in the same world may not overlap. The tree structure makes it less complex to track particles, making the simulations faster. This is because GEANT4 does not need to check for collisions in more complex subvolumes if the mother-volume has not been hit. A special case of such world subdivision approaches are also used in real time 3d engines such as *id tech 1-3*, which suggests that such trees provide an efficient solution for location look-up [13].

GEANT4 uses different models for various physics events and effects. The models to

be used are specified in a *physics list*. From the *physics list* models, GEANT4 generates random time steps at which discrete physical events take place for each particle, given certain conditions, and then it determines what will actually happen and moves the particle along its track until the first event is scheduled to occur or the particle reaches a geometric boundary [14]. In addition, GEANT4 takes into account specified continuous interactions during the steps, such as Bremsstrahlung or interactions with external fields; and interactions that take place when a particle is approximatily at rest, such as a positron annihilation [14].

Some of the processes included in GEANT4, for example Bremsstrahlung, give rise to an infrared divergence, in which an infinite number of massless particles with infinitesimal energies are created. These particles, although infinitely many, sum up to finite energies, and are thus not a problem physically. However, since it is impossible to simulate an infinite number of particles, GEANT4 has a lowest energy for which to generate particles. This lowest energy is determined by a *range-cut*. The range-cut is specified as a length, and particles with energy too low to travel longer than this length are not generated.

The physics in GEANT4 is not fully validated [15], and since the underlying physics itself is not completely understood, there are limitations on what GEANT4 is capable of simulating. For example, the experiments running at the LHC are not fully evaluated and hence, one cannot expect correct results in such cases, as of now. This is also the case for the reactions studied in the *S393* experiment, which is why we have to start simulating reaction products after the target. As an added benefit, since the reaction products are known, we know what to look for in the simulation output. This is in contrast to having GEANT4 randomly generate them according to a model.

4.2. GGLAND

GGLAND is designed to allow for command line simulations of subatomic particle experiments [16]. In order to simulate an experiment with GEANT4 through GGLAND, the obstacles[1] must first be specified in GGLAND. This is done by adding modules to the GGLAND source tree and recompiling the program. For a short example of a C++ source file defining a detector, see Appendix B. When all obstacles necessary for the planned simulation are defined, they can be placed in the world volume by providing appropriate command line options to GGLAND, specifying the position and rotation of each detector, among other things such as detector material.

As mentioned in the paragraph about delta-electrons in Section 2.1.2, a particle travelling through matter is often accompanied by several short-range electrons. Due to these electrons, a particle hitting a detector is usually accompanied by several electrons, also hitting the detector, giving rise to multiple energy deposits. To deal with this, GGLAND will cluster nearby energy deposits within the same segment and store information on which particle made the biggest contribution to each of the clustered hits.

For a more detailed description of GGLAND, including a quick reference on how to define detectors, see Håkans Johansson's GGLAND write-up [16].

---

[1]An obstacle is a part of the experimental setup that the particle has to pass through

4.3. RALF'S TRACKER

As part of the event reconstruction, the trajectory of a particle, its track, needs to be calculated. RALF'S TRACKER, hereafter called "the tracker", is a tool under development used to calculate particle tracks from experimental data. As input, besides a ROOT file (see Section 4.4) containing measurement data, the tracker takes a special configuration file describing detector positions and the ALADiN current.

The tracker tries to find the path for individual particles through the experimental setup that best matches detector hits in input data. From this track, the mass number can be determined for a particle with a given charge, as indicated by Equation 2.1. The charge can be identified, independently of the track, be identified by, for example, energy deposits in the TFW and prior to tracking, thereby allowing the tracker to identify both the mass and charge of the particle.

By using the tracker with simulated data, the methods used to analyse actual experimental data can be evaluated. Since the analysis plays a large part in identifying events, this is essential in order to determine the acceptance of a setup. A version of RALF'S TRACKER, modified by Håkan Johansson to accept simulated data, was used for tracking.

4.3.1. Configuration

To tailor the tracker for the needs of a specific experiment, the user is to make changes to a specific source-file, known as `experiment_specific.hh`, by default. These changes are made to tell the tracker to skip events which fulfill certain conditions. For example, events with energy depositions outside a set of intervals may not correspond to the expected energy deposition of particles of any Z, as predicted by Equation 5.3, and thus the charge cannot be identified. The tracker can be told to discard such events rather then trying to identify them.

After compiling the tracker, configuration files are used to describe different experimental setups. These files also contain calibration data (see Section 5.3.2) such as detector position offsets in the detector coordinate system, as well as customly defined variables.

4.3.2. Outline of a Possible Tracking Algorithm

The algorithm outlined in this section is intended to explain the needed inputs and inner workings of a fully realised tracking algorithm, as implemented in, for example, RALF'S TRACKER. It is an interpretation of the algorithm outlined in a presentation given by Ralf Plag at the *S393/land02 Workshop 2011* [17].

This algorithm assumes that the particle travels straight when not affected by any external field, that is, the magnetic field from ALADiN. This is not the case in reality or in our GEANT4 simulations, since the particles interact with the surrounding medium at random. Nevertheless, the track given by this algorithm may be thought of as an approximate mean trajectory.

In order to solve the problem of a particle travelling through the magnetic field of ALADiN, β, m_0 and Z of the particle need to be determined. The β can be measured from the time it takes for a particle to travel to the TFW relative to a reference time. With an approximate β, Z is determined from the energy depositions in the TFW using Equation 2.4. Given the β and Z approximations, the tracker numerically solves the equation describing a particle travelling through the magnetic field of ALADiN, for different A [17]. The A corresponding to the track yielding detector hits best matching to the hits of the input data is then used.

The tracker can calculate the tracks both forward (defining the direction via the intersections at the SSTs), or backwards (defining the direction via the intersections at the GFIs), or a combination of both (using all four intersections). This corresponds to the different tracking modes used by RALF'S TRACKER [18].

4.4. ROOT

ROOT is a CERN developed C++ framework well suited for data analysis involving large amounts of list-mode data from nuclear and particle physics experiments [19]. The native ROOT file format is used by both GGLAND and the tracker, which makes ROOT suitable for extracting information from these programs. Files in ROOTs native format are hereafter called ROOT files. ROOT can be used interactively through an interpreter, CINT, which allows the user to make quick histogram and scatter plots, as well as to apply various filters (known as "cuts") to the data. It is also possible to use the ROOT libraries from a C++ program or script to extract information.
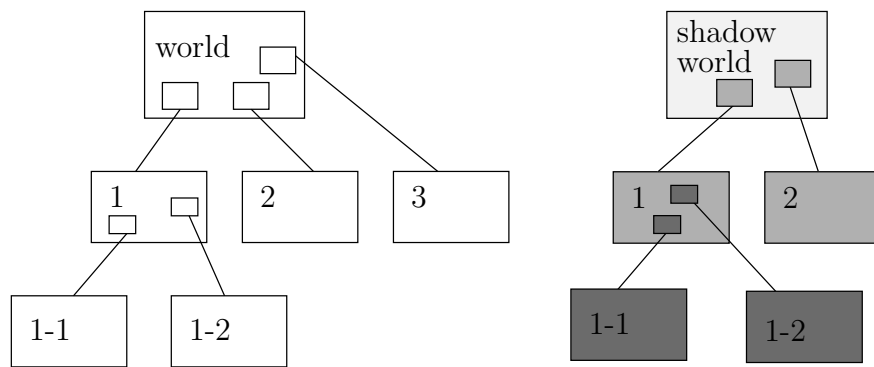
Figure 4.1.: *An illustration on how GEANT4 divides the world volume into several daughter volumes. A "shadow world" can be created which can be divided correspondingly.*

5.   Simulation and Analysis Procedure

The only part of the *S393* experiment that was simulated were the obstacles used to identify outgoing fragments. Namely: the fragment arm (GFIs and TFW), ALADiN and the 2 forward SSTs. The obstacle positions used in the simulation are listed in Table 5.1.

When analysing the outputs of the simulations, we exclusively looked at the clustered hit with the highest energy contribution, the primary hit, for a given event and detector. This will, in most cases, correspond to energy depositions by the original particle. It is also the standard procedure in the tracker at the moment. In rare cases, however, the original particle will just barely miss a detector, while one of the created δ-electrons will hit the detector, thus giving the major energy contribution. Such events are rare and easily filtered with appropriate energy cuts, since they give a low energy deposition.

Table 5.1.: *Obstacle positions used in simulations. The positions are given as (x, y, z) coordinates relative to the beam target. The rotations are made around the obstacles' internal negative y axes.*

Obstacle	Position/cm	Rotation/deg
ALADiN	$(0, 0, 255)$	7
FTF	$(-232.94, 0, 1124.33)$	15
GFI1	$(-56.94, 0, 467.504)$	15
GFI2	$(-72.469, 0, 525.450)$	15
SST1	$(0, 0, 11)$	0
SST2	$(0, 0, 14)$	0

5.1. Determining an Approriate $b\rho$

According to Equation 2.1, charged particles with a constant magnetic rigidity, $b\rho = p/q$, are equally affected by a homogenous magnetic field. While the magnetic field generated by ALADiN is not perfectly homogenous, it may nevertheless be used as an approximation to predict the outgoing angle of charged particles after ALADiN.

To ensure that the particles fired in the simulation hit the fragment arm, an appropriate $b\rho$ needs to be determined. In Appendix A, an expression for determining a $b\rho$ for a desired outgoing angle and a given magnetic field is derived. The resulting expression is

$$b\rho = \frac{bd_z}{\sin(\theta_A) + \sin(\nu - \theta_A)} \,,\tag{5.1}$$

where ν is the angle of the outgoing fragment relative to the initial beam direction, $\theta_A = 7°$ the orientation of ALADiN's gas tube relative to the beam axis and $d_z = 2.42\,\mathrm{m}$ the length of ALADiN's gas tube.

The magnetic field b is controlled by the ALADiN current I. Therefore, different I result in a different fields. Given I is in amperes, I can be approximated by

$$b = 2.187 \cdot 10^{-4}\,\frac{\mathrm{T}}{\mathrm{A}} I + 0.402 T \tag{5.2}$$

This relation is also derived in Appendix A.

5.2. Configuring and Running GGLAND

Before any simulation could be done, it was first necessary to define the geometry of all obstacles used in the simulation. This was done by following the procedure described in Section 4.2. The obstacles added to GGLAND as part of this project, the non-filled obstacles in Figure 3.2, are documented in Appendix C.

We used the GEANT4 physics list `QGSP_BERT` (Quark, Gluon, String Precompound with Bertini cascade) in our simulations (the default in GGLAND). This is expected to give results which are in better agreement with experiments than with just the `QGSP` list for lower energies, but does not employ the *data driven high precision neutron package* of `QGSP_BERT_HP` [20]. The choice to use `QGSP_BERT` instead of `QGSP_BERT_HP` reflects the fact that the part of the setup that was simulated is unable to detect neutrons.

The range-cut for particles used in the simulations were the GGLAND defaults: 1 cm for the world-volume and 0.1 cm for other volumes.

5.3. Preparing and Running RALF'S TRACKER

As mentioned in Section 4.3, some tasks has to be performed before the tracker can be used. This section describes the steps taken to get the tracker work as intended.

5.3.1. Configuration

The changes made to the file `experiment_specific.hh` was the addition of a method for extracting the particle charge from the energy deposited in the TFW, and support for some extra variables used in communication with external sources. For the modified source file, see Appendix E.

Charge determination

To be able to extract the correct Z, we used Equation 2.4 with the assumption that β is approximately constant, which is a valid assumption for sufficiently thin detectors. By using this approximation Equation 2.4 gives

$$-\Delta E \approx \Delta x \frac{4\pi}{m_e c^2} \frac{z^2}{\beta^2} \left(\frac{e^2}{4\pi\epsilon_0}\right)^2 NZ \left[\ln\left(\frac{2m_e c^2 \beta^2}{I(1-\beta^2)}\right) - \beta^2\right] \quad,$$

where the derivative has been replaced by $\frac{\Delta E}{\Delta x}$. In order to determine the detector specific constants, N and I, this equation was rewritten as

$$-\Delta E \approx C \left[\ln\left(\frac{2m_e c^2}{I(1/\beta^2 - 1)}\right)/\beta^2 - 1\right] z^2 \quad. \tag{5.3}$$

The values of C and I were found by minimising the 2-norm of the difference between vectors of the most likely energy deposits in the detector of interest (in our case the TFW) for given pairs (Z, β), and the values predicted by Equation 5.3. For the TFW, this resulted in $C = 0.060319339946223\,\text{MeV}$ and $I = 9.352906073747982 \times 10^{-7}\,\text{MeV}$. For more details on how these values were found, see Appendix F.

In the tracker, $-\Delta E$ is known. To calculate Z, we rewrote Equation 5.3 to yield the formula

$$Z = \sqrt{\frac{-\Delta E}{C \left[\ln\left(\frac{2m_e c^2}{I(1/\beta^2 - 1)}\right)/\beta^2 - 1\right]}} \quad. \tag{5.4}$$

In order to reject particles depositing energies far from the predicted peaks, the additional condition that $|Z - Z_{\text{int}}| \leq \frac{1}{4}$, where Z_{int} is the "nearest" interger to Z [1], was imposed on the calculated Z. If the calculated Z passed this condition, it was identifed as Z_{int}.

In addition, if $-\Delta E \leq 10\,\text{MeV}$, the event is rejected. This mostly filters δ-electrons and perhaps protons and helium, thus it should not have a significant impact on the results. This cut is a remnant from an earlier `experiment_specific.hh` that was not noticed until after some time.

Extra communication variables

The extra communication variables were used to control which β to use as tracker input. These variables are listed together with other variables in Table 5.2.

5.3.2. Calibration

In order to work optimally, the tracker needs to be calibrated with input data. The calibration procedure, whose output depends on the given ALADiN current and detector positions, aims to minimise the difference between tracked data and input data.

---

[1] "nearest" is here defined as floor $(Z + 0.5)$

Below follows a description of the calibration procedure. The calibration steps essentially follow the steps for calibrating the tracker with real experimental data, currently presented on the tracker website [18]. Some alterations had to be made in order to account for the differences between our simulations and the situation in a real experiment. Therefore, we simulated only one kind of ion in a single simulation and no angular calibration was carried out by comparing the angles of fragments, protons and neutrons. For the time calibration of the TFW, the actual β of the simulated particle was used as a first approximation, while a real first approximation would need to contain errors.

In the following list, text written in `teletype font` refers to variables listed in Table 5.2, or command line arguments to the tracker. The algorithm is represented graphically in Figure 5.1. The C++ implementation used in this project is found in Appendix D.

1. To calibrate the time offset, the tracker is run with `--ignore-tof` and `--track-forward`. The β, entered as `Inbeta`, used for time calibration, is the same as the simulated one. Forward mode is used since the β for incoming ions is known. The value of `Truebeta` is set to β since we know that this is the real β. The resulting mean difference between the time of impact of the simulation and the calculations of the tracker (that is, the mean value of `offset_ftft`) is then added to the `OFFSET_FTFT` variable in the configuration file of the tracker, to compensate for the difference. This procedure is repeated until the resulting mean difference is less than 10^{-5} ns; or until a maximum of four iterations is reached, at which point the calibration procedure is aborted and the calibration is considered to have failed.

2. After the time calibration, the x coordinate of the TFW is calibrated. The goal in this step is to bring the mean value of `fres_ftfx` close to 0. To achieve this, the tracker is run with the `--track-backward` option and adding the mean of `fres_ftfx` to the x offset of the TFW until the absolute value of the mean of `fres_ftfx` is less than 10^{-5} cm. If this criterion is not fulfilled in 4 iterations, the procedure is aborted and the calibration is considered to have failed.

3. The final step is to calibrate the mass identification of the tracker. Using the output file from the previous step, the mass-histogram given by the tracker is shifted to yield a peak-value matching the known mass of the simulated particle. This is done by having the tracker calculate the track of a particle with the mass identified by the tracker during the previous step, and a particle with the correct mass. The tracker then identifies x-offsets to adjust the positions of the GFIs and the TFW within the tracker calibration in order to make a particle with the correct mass hit the detectors where the particle with the identified mass hit. This procedure is refered to as playing the *have/want game* on the tracker website [18]. These offsets were then added in the calibration file to the corresponding offset-vector for the involved detectors. The tracker is now considered to be calibrated.

After calibration, a new experiment configuration file was created for the tracker, containing the adjusted detector positions together with calibration data.
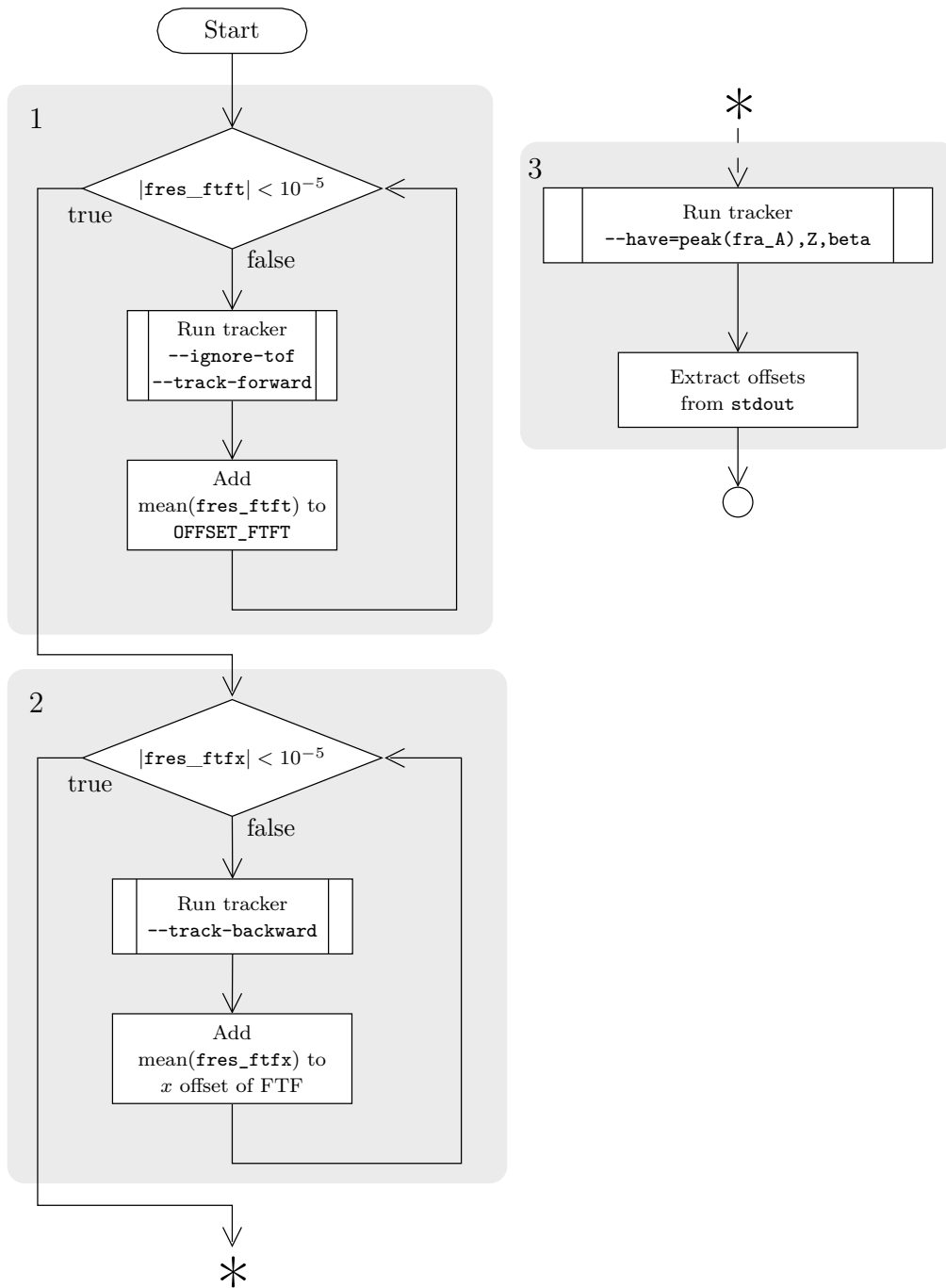
Figure 5.1.: *Flowchart of the calibration procedure for the tracker. Numbers in shadowed boxes reffers to items in the list in Section 5.3.2*

Table 5.2.: *Configuration variables used by the tracker. The symbol $\rightarrow$ indicates that the variable is used as an input to the tracker and is defined in the experiment configuration file. While, $\leftarrow$ indicates that the variable is an output of the tracker.* **`Bold-face`** *variables are variables added for the simulation task.*

	Name	Description
$\rightarrow$	**`Inbeta`**	Used to determine the time of flight when using `--ignore-tof`
$\rightarrow$	**`Truebeta`**	The actual β. This value is used to determine Z from the energy deposited in the TFW.
$\rightarrow$	**`Truebeta_valid`**	A Boolean that is true if and only if the value of `Truebeta` is deemed correct. When `Truebeta_valid` is true, the tracker uses `Truebeta` to identify the Z of the particles using Equation 5.3.
$\rightarrow$	`OFFSET_FTFT`	The time offset added to the time of flight to make the time of flight approximated with `Inbeta` match with the time of flight in the input data.
$\leftarrow$	`fres_ftft`	The difference between tracked time of flight and time of flight in the input data.
$\leftarrow$	`fres_ftfx`	The difference between tracked x position in TFW and x position in TFW in the input data

5.3.3. Running the tracker

When analysing data, the tracker was run twice. The first time with `Truebeta_valid` set to false to get an approximation of the β of the simulated particle, and a second time with `Truebeta_valid` set to true and `Truebeta` to the mean β returned, to identify Z of the particles as described in Section 5.3.

5.4. Angular Dependency in Detected Events

In order to find how the spread of the beam affects the setup's ability to identify fired particles, a simulation with detector positions according to Table 5.1, firing 2^{20} ^{14}B particles with $b\rho = 8.8\,\text{Tm}$ with a spread of 8°, was carried out.

The tracker was not calibrated since the detector positions in the simulation are exactly known, negating the need to adjust detector positions to get good results. Time calibration was also omitted since it was not needed, although it could in principle be used to compensate for the additional physics processes considered in the simulation. Tracking was still done twice, first in order to get a more realistic value for β, as identified by the tracker, to use for Z identification during the second run.

Per event information regarding what kind of particle caused the major energy depositions in the TFW could be retrived from the simulation output ROOT file. This data could then be used together with the ROOT file generated by the tracker to determine whether a particle was correctly identified or not.
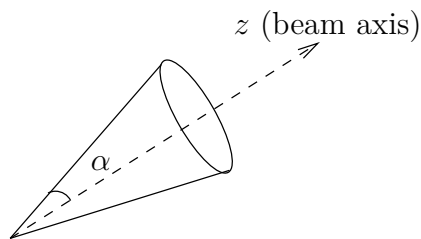
Figure 5.2.: *The opening angle, α, is used as a measurement of the spread of the beam and the initial direction of the fired particle.*

To obtain the dependence of the number of identified particles on the angle between the particles' initial trajectory of the particles and the beam axis, α, illustrated in Figure 5.2, a histogram of $\cos\alpha$ was plotted with appropriate cuts. More specifically, $\cos\alpha$ was plotted for particles having been identified by the tracker as having mass m satisfying $|m - 14\,\text{u}| < 0.5$ and $Z = 5$, corresponding to particles having been identified as ^{14}B. This was done with additional cuts on the type of particles causing the major energy deposit in the TFW to see how often the tracker made a correct or incorrect identification.

Due to the way the α of the fired particle is generated, if the spread had no bearing on the acceptance, the events would have an even distribution over $\cos\alpha$. According to Equation 1.2, the histogram then immediately gives an unnormalised acceptance as a function of α.

5.5. Mass Deviations for Tracker Calibrated With Incorrect Current

One of the goals of the experiment is to identify the particle that left the target according to mass and proton number. The actual magnetic field is only roughly known due to, among other things, magnetic hysteresis. Therefore, it was investigated how well the tracker calibrated with an incorrect ALADiN current works. The process is described below and illustrated in Figure 5.3. All simulations were done using 2^{15} events. The number of bins used for mass peak extraction were floor $\left(100\sqrt{2^{15}}\right) = 18101$ on the interval $[0, 30]$. The peak was detected by looking for the largest peak in an associated `TSpectrum` object with at most 1000 peaks and a resolution of 1.

To have simulated data for analysis as well as to calibrate the tracker, known input data were generated by GGLAND. The isotopes

$$S_B = \{^{10}\text{B}, {}^{11}\text{B}, {}^{12}\text{B}, {}^{13}\text{B}, {}^{14}\text{B}, {}^{15}\text{B}, {}^{17}\text{B}, {}^{19}\text{B}\}$$

were simulated with a current of $I_0 = 2500\,\text{A}$ and $b\rho = 8.8\,\text{Tm}$. The reason for excluding ^{16}B and ^{18}B is that these isotopes do not survive the flight time to the TFW because they are unbound.
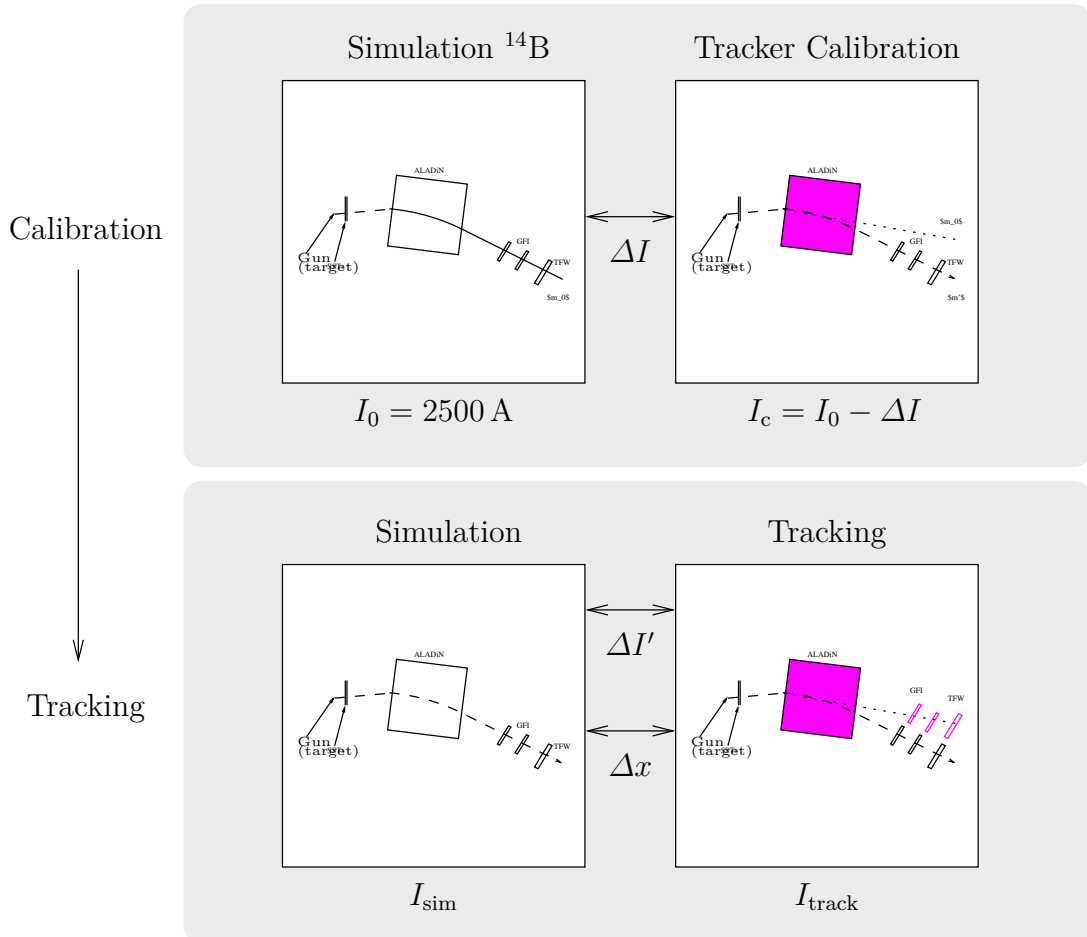
Figure 5.3.: *A procedure to investigate the effects of an incorrect tracker current during calibration. The simulation is run with a current I_0. The tracker, which has its own experimental setup with an incorrect current I_c, is then given the output from the simulation and is calibrated by manipulating detector positions of its experimental setup. The calibrated tracker is then used for tracking outputs from various simulations, often but not necessarily with the same currents as was used during calibration.*

After the simulations mentioned above were done, the tracker was calibrated using the procedure outlined in Section 5.3.2, with the data from the ^{14}B simulation. The tracker was calibrated 8 times, every time given a different current I_c, the currents being the following: 2500 A, 2462.5 A, 2425 A, 2387.5 A, 2350 A, 2312.5 A, 2275 A, and 2237.5 A, with $I_0 = 2500$ A being the actual ALADiN current used in the simulation and the others being increasingly incorrect. A calibration profile was created for each of these currents.

Given the created calibration profiles, the simulation output for each of the nuclides in S_B were tracked. This was done for each calibration profile. The calibration profiles created for S_B were also used for different elements with a fixed mass number; the nuclei ^{22}C , ^{22}N , and ^{22}F were simulated and tracked.

Deviations might also occur when the tracker has been calibrated as above, but is given data acquired with a different current than the current used in the calibration experiment. Therefore, simulations for S_B were done with current $I_{sim} = 2300$ A. Then, the output data were tracked by using each calibration profile, but giving the tracker a current

$$I_{track} = I_c \left(1 - \frac{I_0 - I_{sim}}{I_0} \right) \quad , \qquad (5.5)$$

where I_c is the current given to the tracker during calibration and I_0 is the current used when creating the calibration data. The quantity I_{track} was chosen so that

$$\frac{I_{track}}{I_c} = \frac{I_{sim}}{I_0} \quad .$$

6. Results

6.1. Angular Dependence of Detected Events

As can be seen from the "over $0\,\mathrm{MeV}$ in all" histogram in Figure 6.2a, the number of events hitting all the relevant detectors is constant for low angles, only to drop at $\cos\alpha \approx 0.9988$, corresponding to $\alpha \approx 2.5°$. This behaviour is slightly modified when more strict energy cuts are applied for the signals of the detectors, as can be seen from the other histograms in Figure 6.2a. Most notably, the cut at $3\,\mathrm{MeV}$ for the SSTs greatly reduces the amount of particles detected, while the number of events is here dependent on the spread for low α. The $3\,\mathrm{MeV}$ cuts in the SSTs roughly corresponds to the beginning of a high peak in the energy deposition spectrum of the primary hits, as seen in Figure 6.3. However, the cuts exclude numerous events below the peak value that would be included in the less strict $2\,\mathrm{MeV}$ cut. This gives a plausible explanation for the drops in the number of accepted events.

In Figure 6.2b, the number of particles hitting the different detectors for various $\cos\alpha$ is presented. It can be seen that particles start to miss the GFI2 at an angle that corresponds to the drop in the amount of detected events in Figure 6.2a, suggesting that missing the GFI2 is a cause for the decrease in the amount of events hitting all the detectors.

From Figure 6.2b, it may be seen that more particles should be eligible for forward tracking than mixed or backward. Figure 6.2c shows that this is indeed the case.

Figure 6.2d shows the particles that contributed mostly to the major energy deposits in the TFW. It can be seen that not all of the simulated $^{14}\mathrm{B}$ nuclei reach the TFW as $^{14}\mathrm{B}$. This indicates that some particles undergo reactions along their flightpath resulting in new fragments. From Figure 6.2d, it is possible to determine the maximum tracking efficiency of the experimental setup with analysis methods rejecting fragments that decay during the flight.

Also revealed by Figure 6.2d is that at sufficiently large α, almost no ions give a primary contribution to the energy deposits in the TFW. On the other hand, the fired $^{14}\mathrm{B}$ ion dominates for low spread angles.

The histogram of the successfully mixed-mode tracked particles, presented in Figure 6.2, largely follows the same trends as the histograms of simulated events in Figure 6.1. This suggests that the tracker is efficient in handling trackable events.

Tracking with some of the stricter energy cuts seemingly offers no advantages for the

28

Figure 6.1.: *Histograms with 150 bins depicting the number of particles in a simulation with 2^{20} ^{14}B simulated for $b\rho = 8.8$ Tm with a maximum spread of $8°$ for different $\cos\alpha$ that...*
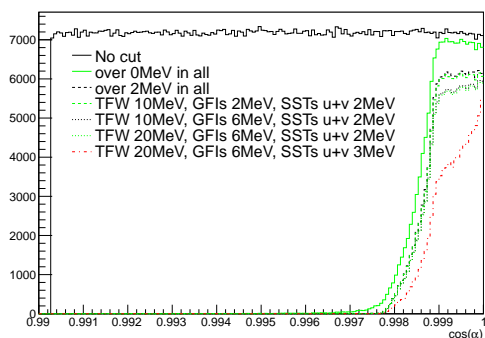
(a) ...caused energy deposits above certain values in the detectors. "No cut" shows every particle fired.
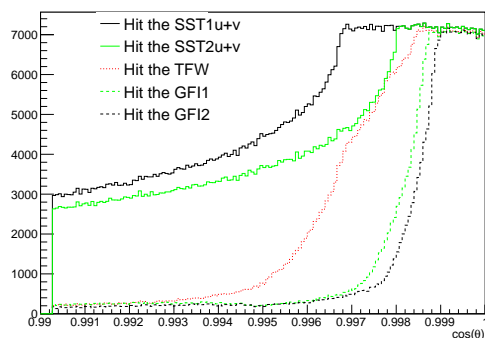
(b) ...hit the different detectors.
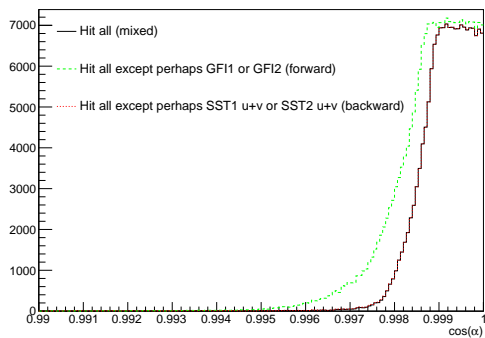
(c) ...were eligible for the different tracking modes in RALF'S TRACKER.
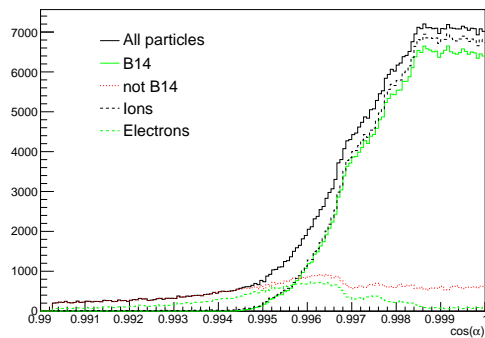
(d) ...caused primary deposits in the TFW attributed to different particles.

29

(a) Over 0 MeV in all detectors

(b) Over 2 MeV in all detectors

(c) Over 20 MeV in TFW, 6 MeV in the GFIs 3 MeV in the SSTs (u+v)

(d) Over 0 MeV in all and $|A - 14| < 0.1$
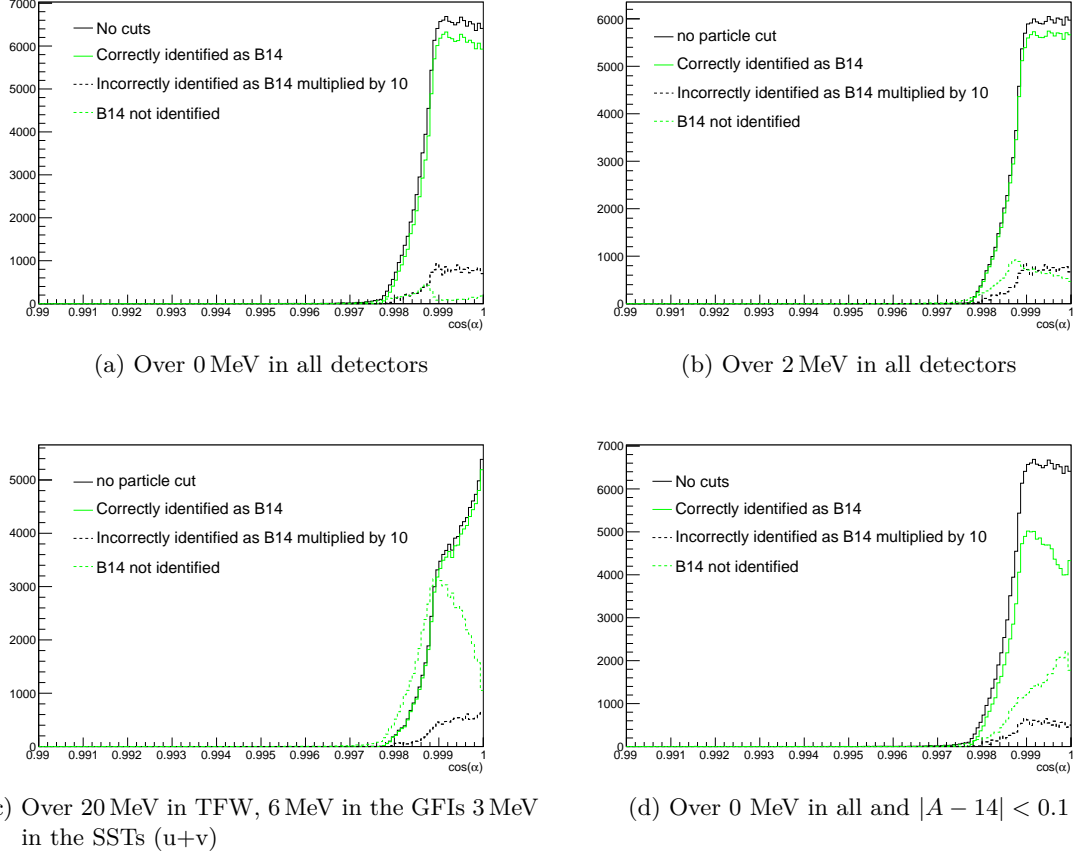
Figure 6.2.: *Histograms with 150 bins depicting the number of particles identified as various particles by RALF'S TRACKER from a simulation with 2^{20} ^{14}B nuclei simulated for $b\rho = 8.8$ Tm with a maximum spread of $8°$ for different $\cos \alpha$. Different parts of the figure corresponds to additional cuts on the energy deposits in various detectors. The histogram labeled "No cuts" corresponds to every particle the tracker managed to track for the given additional the energy cuts, as in "no cuts" in applied to particle type. The "B14 not identified" histogram includes ^{14}B nuclei, which where not included in the energy cut. The energy cuts of the different parts of the figure correspond to different the histograms in Figure 6.2a. Figure (d) is with a stricter condition for A to be considered correctly identified, otherwise the condition $|A - 14| < 0.5$ was used.*

Figure 6.3.: *Number of primary energy deposits with certain energies in the SST1u from a simulation with ^{14}B nuclei fired at $b\rho = 8.8\,\text{Tm}$ with a spread of $8°$. The peak around 0 can most likely be attributed to δ-electrons, while the other peak is due to ^{14}B passing through the detector.*

given simulation, since the amount of incorrectly identified ^{14}B hardly decreases, while the numbers of unidentified ^{14}B notably increases for both cuts. The same can be said about a stricter A identification, shown in Figure 6.2d, where particles not fired exactly straight along the z-axis seemingly are easier to identify.

6.1.1. Reasons for the Decrease in Events with Spread

Figure 6.4a together with Figure 6.5 gives a plausible explanation for the drops in events in the GFI2 for $\cos\alpha < 0.9988$, as seen in, for example, Figure 6.2a. Figure 6.4a depicts the number of events as a 2D-histogram with respect to the spread $\cos\alpha$ and the y coordinate of the GFI2. For a given spread, the particles are expected to be distributed approximately homogeneously on a circle, as can be seen in Figure 6.5a. This explain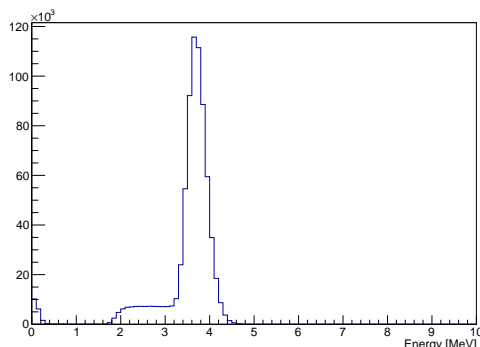s the fact that the events for a given spread in Figure 6.4a are found within intervals around $y = 0$, with most events at the end-points. The points where the bright curve, defined by the edge of the event-interval for different $\cos\alpha$, intersects with the edge of the plot corresponds to particles on the expected circle missing the GFI2 in the y direction, which can be seen in Figure 6.5b. Plots corresponding to Figure 6.4a and Figure 6.5a display the same characteristics for the other detectors, with one notable exception: the TFW. As can be seen in Figure 6.4b and Figure 6.5, particles with a $\cos\alpha < 0.9988$ in the negative y-direction, as well as particles with $\cos\alpha < 0.9982$ in the positive y-direction seem to have trouble reaching the TFW.

From this it can be concluded that at $\cos\alpha \approx 0.9988$, particles start to miss the GFI2 due to passing beyond the limiting dimensions of the detector. In the same way, it can be seen that at $\cos\alpha \approx 0.9987$ and $\cos\alpha \approx 0.9985$, GFI1 is frequently missed in the y and/or x direction, followed by SST2 at $\cos\alpha \approx 0.9979$, SST1 at $\cos\alpha \approx 0.9969$, both only in the y direction, and finally the particles that miss the TFW at $\cos\alpha \approx 0.9966$ in the x direction.
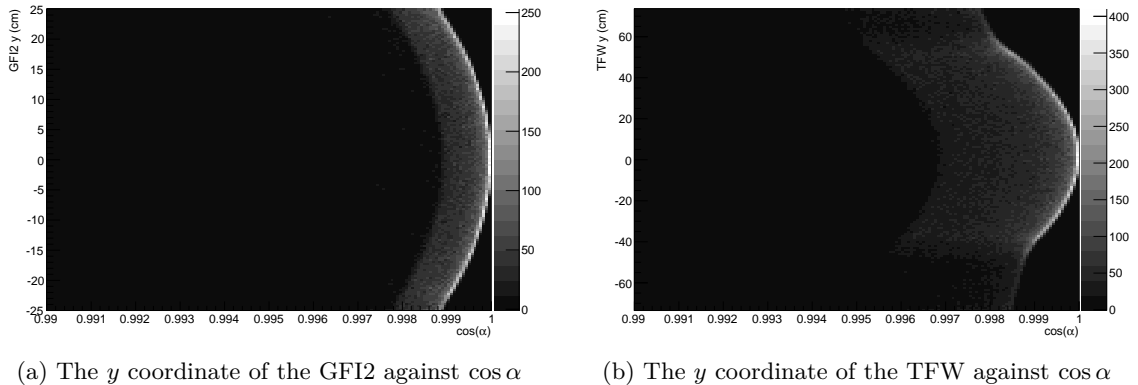
(a) The y coordinate of the GFI2 against $\cos \alpha$

(b) The y coordinate of the TFW against $\cos \alpha$

Figure 6.4.: *Histograms with 150×150 bins depicting the number of primary energy deposits at different y-coordinates in different detectors in a simulation with 2^{20} ^{14}B nuclei fired at $b\rho = 8.8\,\mathrm{Tm}$ with a spread of 8°. $\cos \alpha$ refers to the trajectory fired particles initial angle with the beam axis. Brighter bins indicate more events.*

6.2. Effects of Incorrect Currents on Tracking

Let $\Delta m = m_{\mathrm{det}} - m_{\mathrm{sim}}$, where m_{det} is the mass peak detected by the tracker and m_{sim} is the actual mass of the ion used in the simulations. The notations used for currents are the same as those in Section 5.5, with ΔI refering to the difference in the current of the simulation and tracker *during* calibration, not necessarily during tracking.

The graphs in Figure 6.6 show the results when using different calibration profiles on the simulation output files with $I_{\mathrm{sim}} = 2500\,\mathrm{A}$ for the isotopes in S_B defined in Section 5.5. It is clear that all isotopes have been identified correctly, and that the absolute value of the mass deviation is less than $0.04\,\mathrm{u}$, regardless of the current used when calibrating the tracker. If instead, as in Figure 6.7, A is shown on the x-axis, the mass deviation seems to increase as A increases.

By trying to track the output from simulations for $A = 22$ on $Z \in \{6, 7, 8, 9\}$ with the same I, the results in Figure 6.8 were obtained. Also in this case, all isobars are correctly identified with a maximum mass deviation less than $0.06\,\mathrm{u}$. In Figure 6.9 the same output is plotted as a function of Z. In this figure, the mass deviation seems to decrease as Z increases.

When using a different simulation with a different current, and running the tracker on that simulation output, using the old calibration profiles together with a current according to Equation 5.5, the results in Figure 6.10 were obtained. Still, all isotopes are identified correctly, but now the absolute value of the mass deviation exceeds $0.09\,\mathrm{u}$.

As illustrated in Figure 6.11, during the calibration procedure, the tracker moves the detectors in a way that the line from the center of ALADiN through the detectors'

(a) GFI2: $0.9988 \leq \cos\alpha < 0.9989$

(b) GFI2: $0.9987 \leq \cos\alpha < 0.9988$

(c) TFW: $0.9988 \leq \cos\alpha < 0.9989$

(d) TFW: $0.9986 \leq \cos\alpha < 0.9987$

Figure 6.5.: *Histogram wih 150×150 bins depicting the number of primary energy deposits for x and y-coordinates at different $\cos\alpha$ ranges in different detectors in a simulation with 2^{20} ^{14}B nuclei fired at $b\rho = 8.8\,\mathrm{Tm}$ with a spread of $8°$. $\cos\alpha$ refers to the trajectory fired particles initial angle with the beam axis. Brighter bins indicate more events.*

Figure 6.6.: *Mass deviation, $\Delta m = m_{det} - m_{sim}$, between the simulated and tracked mass for $Z = 5$ and different A, plotted against the difference, $\Delta I = I_0 - I_c$, between the current used to generate calibration data and the current used when calibrating the tracker. The data was acquired by running the tracker, using all different calibration profiles, on simulation data with the same current as the input used for calibration. The quanties I_0 and I_c are defined in Section 5.5. The quanties I_0 and I_c are defined in Section 5.5.*
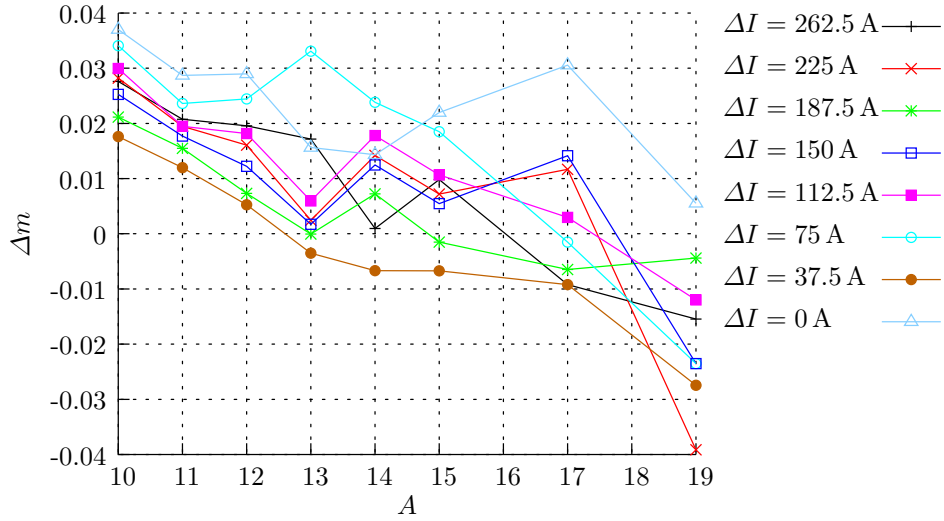
Figure 6.7.: *The same data as in Figure 6.6, plotted against A.*

Figure 6.8.: *Mass deviation, $\Delta m = m_{det} - m_{sim}$, between the simulated and tracked mass for a $A = 22$ and different Z, plotted against the difference, $\Delta I = I_0 - I_c$, between the current used to generate calibration data and the current used when calibrating the tracker. The data was acquired by running the tracker, using all different calibration profiles, on simulation data with the same current as the input used for calibration. The quanties I_0 and I_c are defined in Section 5.5.*
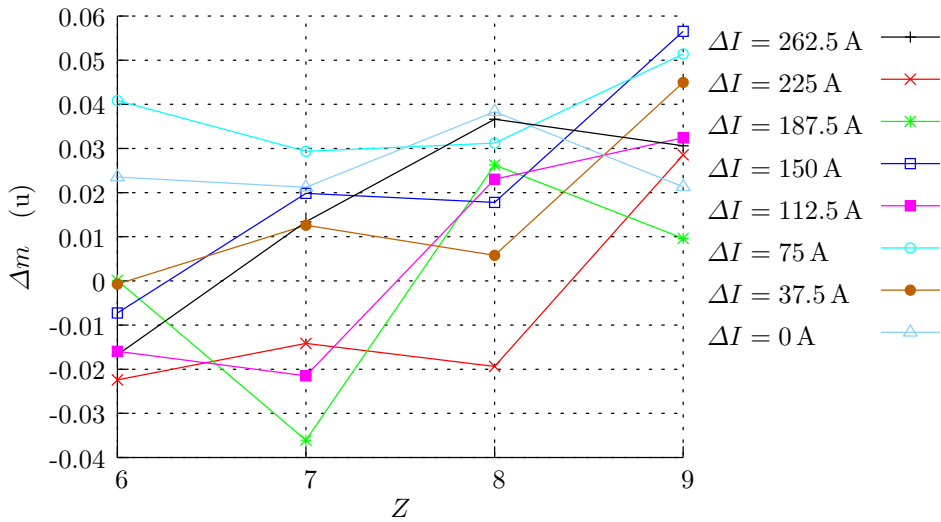
Figure 6.9.: *The same data as in Figure 6.8, plotted against Z.*

becomes rotated by an amount that compensates for the deviation in current. Since the tracker only modifies the x coordinate of the detectors, this makes the arm slightly longer or shorter, and the detectors themselves are not rotated. This effect of an incorrect current is in agreement with what Ralf Plag presented at the *S393/land02 Workshop 2011* [17]. A visualisation of this is presented in Figure 6.12, where z_{dist} is the distance from the detector to the center of ALADiN, x_{off} is the x-offset of the detector, and

$$\theta_{\mathrm{off}} = \arctan\left(\frac{x_{\mathrm{off}}}{z_{\mathrm{dist}}}\right) \tag{6.1}$$

is the resulting effective rotation.

Additional parameters of interest, such as the initial direction of the outgoing fragment, presented in Figure 6.13, are not as easily identified by the tracker. As seen in Figure 6.13b and Figure 6.13d, there is a large discrepancy in the y-component of the reconstructed direction-vector and the y-component of the fragments initial momentum p in the simulation. However, this behaviour does not seem to depend on the current given to the tracker, as can be seen by comparing Figure 6.13b and Figure 6.13d.
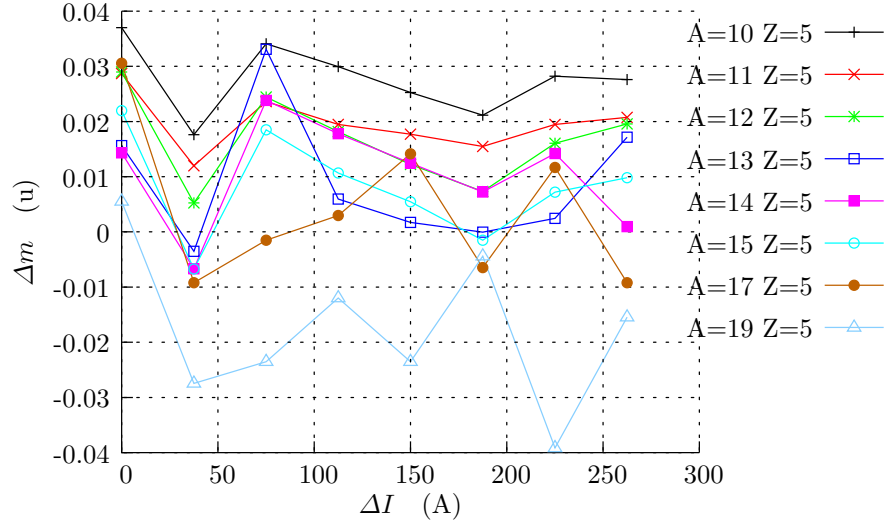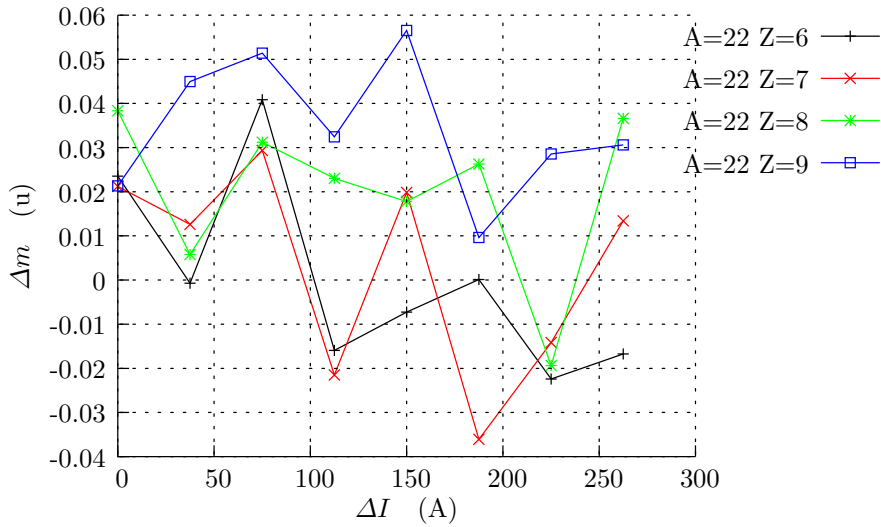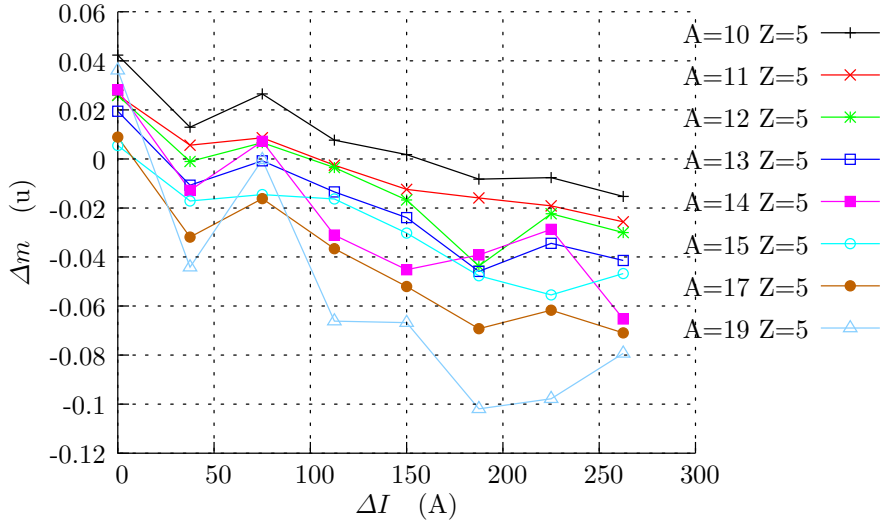
Figure 6.10.: *Mass deviation, $\Delta m = m_{det} - m_{sim}$, between the simulated and tracked mass for different A and $Z = 5$, plotted against the difference, $\Delta I = I_0 - I_c$, between the current used to generate calibration data and the current used when calibrating the tracker. The simulations were done with a current of 2300 A and the current given to the tracker was calculated from Equation 5.5. The quanties I_0 and I_c are defined in Section 5.5.*
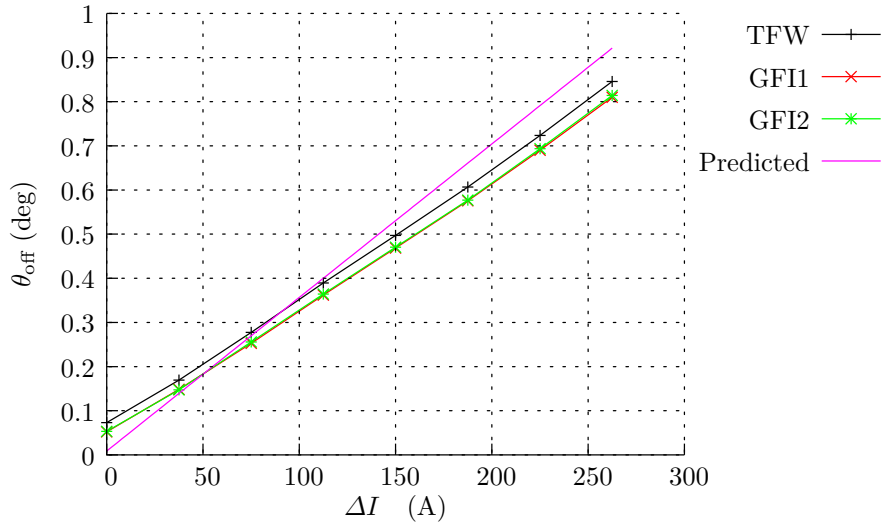
Figure 6.11.: *Fragment arm rotation after tracker calibration, as a function of the difference, $\Delta I = I_0 - I_c$, between the current used to generate calibration data and the current used when calibrating the tracker. The angle was calculated using Equation 6.1. The "expected" line is the predicted difference between the angle of the outgoing fragment and the fragment arm for the trackers incorrect current, as given by Equation 5.1. The quanties I_0 and I_c are defined in Section 5.5.*

37

6. Results
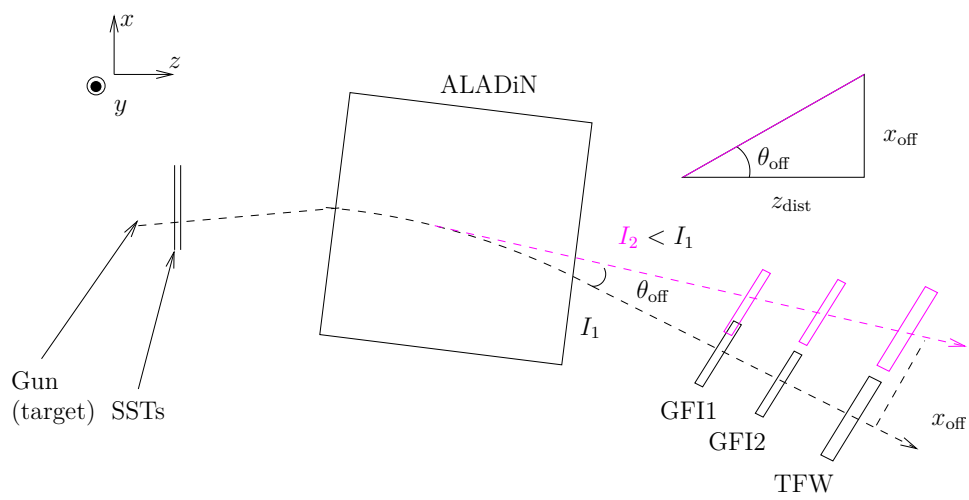
Figure 6.12.: *The effect of different currents on a particles track. Since the tracker uses the incorrect current I_2, it must move the detectors of the fragment arm during calibration step 3 in order to get the desired mass.*

(a) x direction, $I_{\text{track}} = 2500\,\text{A}$

(b) y direction, $I_{\text{track}} = 2500\,\text{A}$

(c) x direction, $I_{\text{track}} = 2237.5\,\text{A}$

(d) y direction, $I_{\text{track}} = 2237.5\,\text{A}$
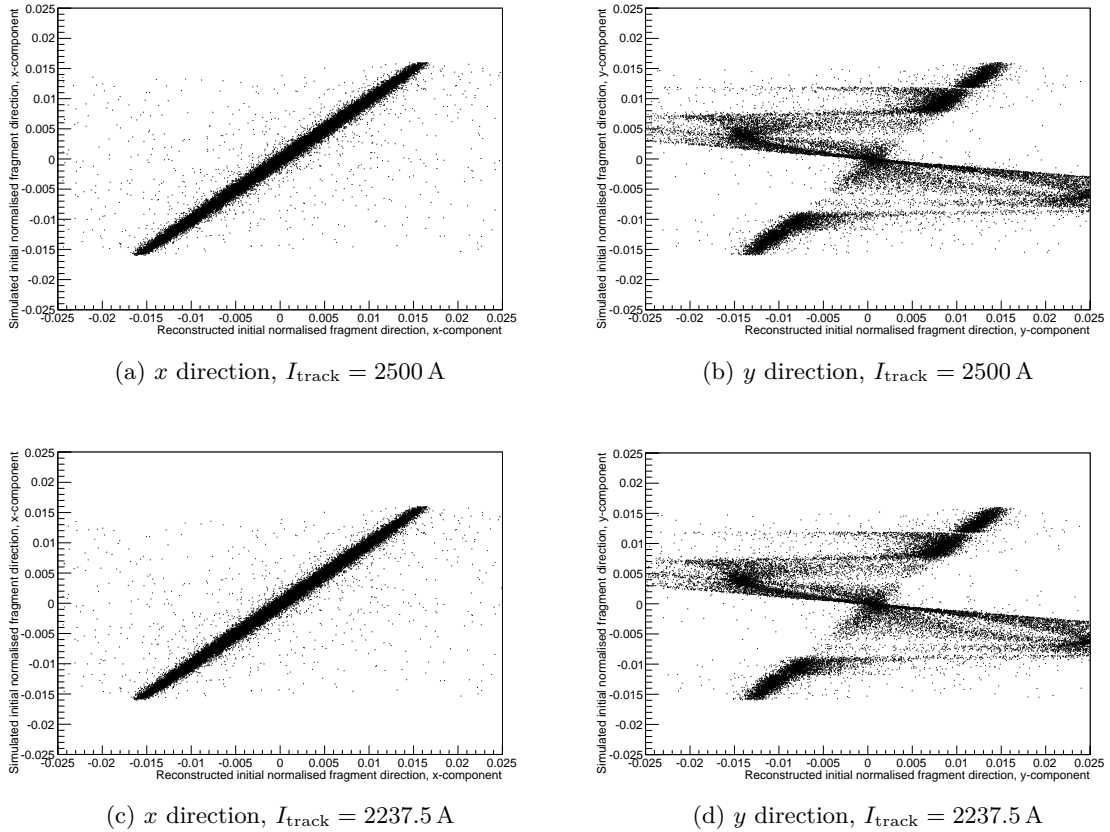
Figure 6.13.: *Reconstructed x and y-components of the direction of the outgoing fragments at the target plotted against the initial normalised x and y-components momentum of the outgoing fragment in the simulation. I_{track} refers to the current given to the tracker. The data presented is from a simulation with ^{14}B fired at $b\rho = 8.8\,\text{Tm}$ with a spread of $16\,\text{mrad}$ and an ALADiN current of $I = 2500\,\text{A}$.*

7. Discussion

7.1. Angular Spread, Detected Events

From comparing Figure 6.2 with Figure 6.1, it is clear that the tracker is efficient at identifying fired $^{14}\mathrm{B}$ hitting the detectors for the $|A-14| < 0.5$ identification condition. However, Figure 6.2d indicates that the tracker has problems identifying the mass of the particle to high precision, but this surprisingly gets better for moderate α. This might be due to the slightly incorrect energy deposits in the TFW predicted by Equation 5.3, or perhaps the slightly incorrect mass or differences in how the tracker and GEANT4 calculate tracks. Increased precision will probably not be necessary for simulations where single particles are fired, as done in this project, but it may needed to cut down the number of incorrectly identified particles in simulations where more than one particle is fired simultaneously.

7.1.1. Energy Cuts

Although it was concluded in Section 6.1 that energy cuts do not improve the efficiency of the tracker, some energy cut above zero should be used to simulate the fact that the detectors within the experimental setup have a threshold energy. The $2\,\mathrm{MeV}$ cut is possibly too harsh, but it indicates that such cuts need not distort the dependence of the spread on the number of detected hits. There is still a danger though, since particles with lower Z and higher β would deposit lower energy, thus bringing the peak closer to the threshold energy, which may give rise to behaviour similar to the one seen in the strictest cut in Figure 6.2a. To determine when and if this could become a problem, values for the constants in Equation 5.3 for the SSTs would be required, as well as a value of the threshold energy.

There are also other, "hidden", energy cuts in the simulation. For one, the Z-identification described in Section 5.3 will only identify particles depositing energies in the TFW around the values predicted by Equation 5.3. These cuts make the Z-identification more well-behaved, but systematically reject outliers. It may thus be worth trying out other ways to identify Z. The energy deposits of charged particles for medium-thick detectors and certain energy ranges supposedly follow a Landau-distribution [21]. This may be useful to define a more sophisticated method to determine the most likely charge of a particle given its energy distribution, without rejecting any particles.

Another "hidden" energy cut is due to the range-cut. As mentioned in Section 4.1,

40

GEANT4 will not generate particles with too low energy to travel a certain distance. This will bring the effective energy cut to somewhere above zero. A comparison between different range-cuts can be found in the *GGLAND write-up* [16]. The primary effects of different energy cuts seems to be that a lower range-cut increases the amount of secondary hits in the detectors [16]. Since the secondary hits were not considered in the analysis, as described in the introduction in Section 5, this should not affect the results considerably.

In any case, the tracker is often able to track most of the particles after the cuts and the output histograms closely reflect the input simulated data, as can be seen from the similarity of the histograms in Figure 6.2 with corresponding histograms in Figure 6.2a.

7.1.2. Dip in Detected Events

As was seen in Section 6.1.1, the dip in the amount of events detected when $\alpha \gtrsim 2.5°$ ($\cos \alpha \lesssim 0.9988$) can probably be attributed to particles starting to miss the GFI2 and then other detectors. However, the fact that particles stop hitting the TFW in an ellipse for a given α at $\cos \alpha \approx 0.9988$ cannot be explained by the geometry. Some plausible explanations could be

1. Particles with a certain θ and ϕ are bent off in ALADiN in a way that gives rise to the effects observed in Figure 6.4b.

2. GGLAND treats particles missing the GFIs differently, since they do not cross boundaries as often as the ones which hit the GFIs, making them miss the TFW as well as the GFIs.

The first explanation could be investigated by looking at the particles fired with $\cos \alpha \approx 0.9988$. By plotting the number of hits in the TFW against $\arctan(p_{y0}/p_{x0})$ of the fired particles, problematic ϕ-angles could be identified. For these angles, a GGLAND-simulation could be run with ALADiN compiled to dump the field-strength at the points the particle travel. These would reveal if there are anomalies in the ALADiN fieldmap causing a loss of particles. Even without anomalies, the possibility of the field of ALADiN causing particles to miss the TFW cannot be ruled out, as even comparatively small initial differences in particle trajectories in ALADiN could give a notable spread in the distant TFW.

The second explanation is less likely, since the fact that the world volume is made out of air would be the primary factor limiting the step-length used by GEANT4. The additional boundaries presented by the GFIs would probably not make a notable difference. This would also not explain why Figure 6.4b is asymmetric. This could be investigated by changing the size of the GFIs, to see if the angles where the amount of hits in the TFW drips follow the angles for which particles will start to miss the GFI.

Although interesting, the particles missing the TFW are not the primary constraints to the ability of the simulated setup to detect particles with a $\alpha \gtrsim 2.5°$, as this is due to particles missing the GFI2.

7.2. Compensating for Incorrect Current

As can be seen from Figure 6.11, the tracker is able to compensate for an incorrect current by moving the detectors of the fragment arm in a way that roughly corresponds to rotating the entire fragment arm around the center of ALADiN. Since the tracker does not really rotate the fragment arm, there are a at least two errors introduced, disregarding the incorrect detector positions:

1. The detectors of the fragment arm will be further away from the center of ALADiN.

2. The detectors of the fragment arm will not face the center of ALADiN.

Since the particles move at a considerable fraction of the speed of light, the resulting time-offset from moving the TFW will be negligible compared to the time resolution of the TFW and can be recalibrated. Orders of magnitude larger time-offsets would cause problems in determining β, making the tracker unable to correctly identify particles, but such errors in the ALADiN current would be unrealistic.

Likewise, the fact that the detectors are not directly facing ALADiN anymore could cause problems, but even for an error of 10% in current, the detectors would be merely a degree off, just barely distorting the beam area of intersection with the detectors.

Thus, neither of these errors should considerably impact ability of the trackers to identify particles. The fact that the tracker is using incorrect detector positions after ALADiN is still worrying, and it may introduce other errors that perhaps could be revealed by other, less idealistic, simulations. Less idealistic as in with spreads in all parameters, and with more than one particle fired at once.

A possibly better solution for calibration would perhaps be to adjust the current instead of detector positions in cases where this would lead to a good fit. A simple way to implement this for our simulation and tracking scheme would be to look at how many degrees the tracker effectively has rotated the fragment arm with, and use that angle instead. with the by-the-tracker given $b\rho$ to find a current corresponding to the offsets of the detectors.

A typical indication that it is time to adjust the current would be if each detector of the fragment arm have been approximately rotated with respect to the center of ALADiN by the same angle, that is, if

$$\theta_{\text{off}} = \arctan\left(\frac{\text{x offset}}{\text{distance from ALADiN center}}\right)$$

for the different detectors are roughly the same. If this is the case, we can get an approximation for the difference in I by using Equation 5.1 for both the real and tracked current and outgoing angle of the particles. This yields:

$$\frac{d_z}{b\rho}(b_{\text{real}} - b_{\text{track}}) = \sin\left(\nu_{\text{real}} - \theta_{\text{A}}\right) - \sin\left(\nu_{\text{track}} - \theta_{\text{A}}\right) \approx \nu_{\text{real}} - \nu_{\text{track}} \equiv \theta_{\text{off}} \quad . \quad (7.1)$$

Inserting Equation 5.2 together with numerical values for $d_z = 2.42\,\text{m}$ gives

$$I_{\text{off}} = (I_{\text{real}} - I_{\text{track}}) = Cb\rho\theta_{\text{off}} \quad , \tag{7.2}$$

where $C = 1888.80350899349 \frac{\text{A}}{\text{Tm}}$, $b\rho$ is given in Tm and θ_{off} in radians. This gives an approximation of the real current from the x-offsets of the detectors given by the tracker and the current specified in the trackers config-file. As a quick verification, $\theta_{\text{off}} = 1°$ for $b\rho = 8.8 \, \text{Tm}$ gives $I_{\text{off}} \approx 230 \, \text{A}$, which is reasonably close to the actual I_{off} at approximately $250 \, \text{A}$, as seen in Figure 6.11. This first-order approximation does not rely on any measurements from the real experimental setup. It should be possible to track again after adding the current offset and iterate until the real current is known.

Equation 5.1 should be used with care, since it relies on approximating the effective magnetic field felt by the particle with a homogeneous field within ALADiN. Since the real field felt by the particle will vary depending on the particles trajectory, the formula may not be valid for particles with a large α or a $b\rho$ far away from the $b\rho$ predicted by Equation 5.1 ($8.8 \, \text{Tm}$ for $I = 2500 \, \text{A}$). It has nevertheless successfully predicted $b\rho$ for different currents, and particles with a α up to about $2.5°$ do on average end up hitting ellipses aligned around the center of the detectors of the fragment arm. This suggests that the field felt by the particle does not change too drastically for particles well behaved enough to hit the detectors of the fragment arm, which is a condition for Equation 5.1 to remain valid.

Other parameters of interest, such as the angle of the outgoing fragment at the target, are more problematic to reconstruct. This can be seen in Figure 6.13, where the tracker fails to reconstruct the direction of particles with a low momentum in the y direction. This behaviour has been observed in all investigated tracked files, which indicates that this is due to a bug or a limitation in RALF'S TRACKER, or how GGLAND exports data to the tracker.

This effect does not seem to be related to the current given to the tracker, as also can be seen in Figure 6.13. This is reasonable, since the tracker does not move the SSTs during any of the steps in the calibration scheme. This is well motivetad, since uncertanties in the magnetic field mostly would effect the track after ALADiN, those uuncertainties should be compensated for by either moving the detectors after ALADiN or adjusting the current. Trying to compensate for these errors by moving the SSTs could cause these uncertainties to negatively affect the determination of the outgoing fragment at the target, which carries the actual information about the reaction at the target.

Thus, if the strange output from the tracker could be understood and remedied, the tracker might be able to reconstruct the angles of the outgoing fragments.

7.3. Outlook

On the 22th of May, the deadline for handing in the report, it was found out that the tracker had a hidden default $180°$-rotation of the SST2 around its x-axis, resulting in an effectively mirrored y-axis. Due to this rotation, the tracker was unable to correctly reconstruct the y-component of the direction taken by the outgoing fragment, as seen in Figure 6.13.

Because of this, the y-component of the initial trajectory of all tracked particles have
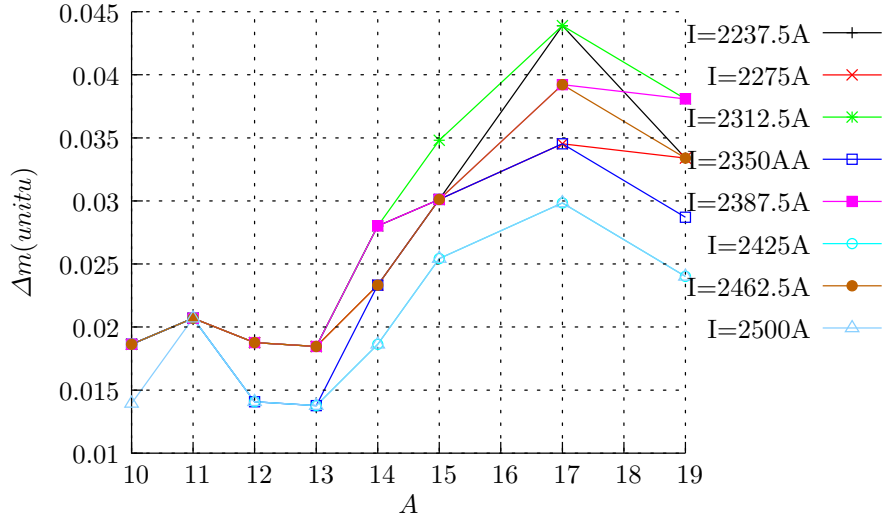
Figure 7.1.: *The mass deviation $\Delta m = m_{det} - m_{sim}$ for different isotopes of boron induced by an incorrect calibration current I_c. ΔI is defined as $I_0 - I_c$, where I_0 is the current used in the simulation. This figure can be considered a corrected version of Figure 6.7. The reason for the identical mass deviation for a different datapoints is due to the fact that the number of bins in the histogram used to identify the mass peak is scaled according the number of events, yielding poor resolution for the 4096 events used in this calibration.*

been distorted, due to the the way the tracker calculates it from hit data in the TFW and the SSTs. Therefore, the results presented in this report contain unnecessary errors. However, these errors can be expected, and have somewhat been confirmed, to have a small impact on the identifications of particles. This can be attributed to the fact the the y-component of the fragments velocity will not considerably effect the deflection angle due to the magnetic field, since the field is comperatively weak in the x and z direction, as seen in Figure A.2.

To confirm that the errors do not considerably affect the identification of particles, quick tracking was done with the rotation of the SST2 corrected. Using only the first 4096 trackable events from a previously generated simulation output, mass deviations introduced by calibrating the tracker with an incorrect current were retrieved. These are presented Figure 7.1, in which it can be clearly seen that the values are well within the limits to distinguish two different mass numbers, just as in Figure 6.7. As such, the conclusion that the tracker is able to compensate for the incorrect calibration current still remains valid. The fact that many of the datapoints in Figure 6.7 is due to the fact that the number of bins in the histogram used to find the mass-peak is scaled according to the number of events.

In addition, the same data that was tracked to yield the results in Figure 6.2 were tracked once again with the SST2 rotation corrected for, and the results can be seen in

Figure 7.2. By comparing the 2 Figures, it is clear that the conclussions in this report regarding the trackers ability to identify particles depending on their α remains valid.

Of course, the other results of Section 6.2 will have to be reconfirmed individually. With the simulation and analysis infrastructure used during this project, this can be done within a day or two.

Apart from these errors, there is still work to be done before GGLAND and RALF'S TRACKER will be applicable to the entire experimental setup used in *S393*. The PDC, XB and LAND detectors as defined in GGLAND currently do not give output data compatible with RALF'S TRACKER, preventing tracking of off the full setup.

Related to defining detector geometries in GGLAND, there is still work to be done. The most apparently problematic detector is the PDC, for which the planes used to identify the x and y coordinates of a passing charged particle currently have to be placed as seperate detector and rotated relative to one another. More details of the detectors, such as read-out electronics, could always be added, although this has the downside of making the detectors very specific.

Related to the analysis of the *S393* experiment, the acceptance of fragment arm together with the other arms and the XB needs to be investigated in order to determine the acceptance of the setup. With the acceptance, cross sections of the studied reactions could be determined.

In the far future, as part of the expansion of GSI into FAIR (Facility for Antiproton and Ion Research), new detectors such as NeuLand, will eventually need to be implemented if GGLAND is to remain a useable tool for simulating future experiments.

(a) Over 0 MeV in all detectors

(b) Over 2 MeV in all detectors

(c) Over 20 MeV in TFW, 6 MeV in the GFIs 3 MeV in the SSTs (u+v)

(d) Over 0 MeV in all and $|A - 14| < 0.1$
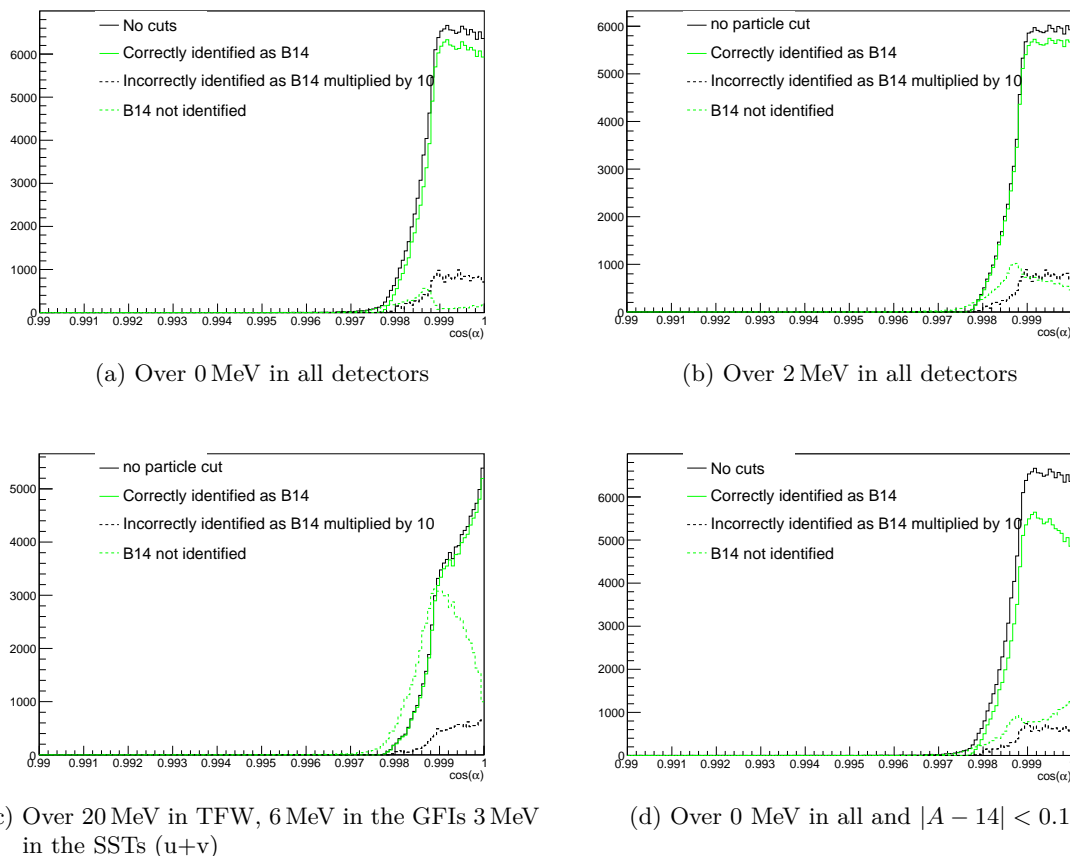
Figure 7.2.: *Results from a tracker with the SST2 rotated, corresponding to Figure 6.2 with an unrotated SST2. The histograms, with 150 bins each, depicts the number of particles identified as various particles by RALF'S TRACKER from a simulation with 2^{20} ^{14}B nuclei simulated for $b\rho = 8.8$ Tm with a maximum spread of $8°$ for different $\cos \alpha$. Different parts of the figure corresponds to additional cuts on the energy deposits in various detectors. The histogram labeled "No cuts" corresponds to every particle the tracker managed to track for the given additional the energy cuts, as in "no cuts" in applied to particle type. The "B14 not identified" histogram includes ^{14}B nuclei, which where not included in the energy cut. The energy cuts of the different parts of the figure correspond to different the histograms in Figure 6.2a. Figure (d) is with a stricter condition for A to be considered correctly identified, otherwise the condition $|A - 14| < 0.5$ was used.*

Glossary

CINT A relaxed C++ interpreter used in ROOT, page 17

GEANT A toolkit for Monte-Carlo simulation of particles, page 14

GGLAND A wrapper library and program used to communicate with GEANT3 or GEANT4, page 14

RALF'S TRACKER A program used to find particle tracks best matching input data from detectors., page 16

ROOT A C++ framework for data analysis, page 17

experiment_specific.hh A file used by RALF'S TRACKER where to user can add extra conditions for rejecting events and identifying Z, page 16

Active volume The volume of a detector able to detect energy deposits of particles., page 8

Clustered hit Nearby energy depositions within a detector segment are grouped in a cluster, a clustered hit, page 15

Command line option Value given to a program at start-up, page 15

Cut A filter on a dataset that yields a data subset satisfying the filter conditions., page 17

Daughter volume A volume located inside another volume in GEANT4, page 14

Delta-electron Freed electron due to a passing charged particle with enough energy to ionize nearby atoms, page 8

GSI GSI Helmholtz Centre for Heavy Ion Research, a research center in Darmstadt, Germany, page 2

Heuristic method A method for finding good enough solutions to problems that may lack exact solutions., page 1

Magnetic rigidity The magnetic rigidity of a particle, $b\rho = p/q$, determines how it will travel through a magnetic field, page 6

Monte-Carlo simulations Stochastic methods for simulating processes using random numbers, page 14

obstacle A part of the experimental setup that the particle has to pass through., page 15

Primary hit The clustered-hit with the highest energy contribution, page 19

Range-cut A threshold energy for generation of particles in GEANT4, given by how far the generated particle is likely to travel, page 15

ROOT file A file used by ROOT, page 17

S393 An experiment with neutron rich $4 \leq Z \leq 10$ nuclei conducted at GSI, page 2

Spread The maximum angle between the beam axis and a particles trajectory, page 12

Wrapper A function or library that simplifies calls to other more elementary functions, page 14

Bibliography

[1] R. K. Bock. Acceptance — The Particle Detector Brief Book, 1998.
`http://rkb.home.cern.ch/rkb/PH14pp/node3.html`. (accessed 26 Feb. 2013).

[2] M. J. Berger, J. H. Hubbell, S. M. Seltzer, et al. XCOM: Photon cross sections database. National Institute of Standards and Technology, 2010.
`http://www.nist.gov/pml/data/xcom/index.cfm`. (accessed 17 Apr. 2013).

[3] G. Knoll. *Radiation detection and measurement*. Wiley, 2000.

[4] G. Knoll. *Radiation detection and measurement*, chapter 2. Wiley, 2000.

[5] G. Knoll. *Radiation detection and measurement*, chapter 8. Wiley, 2000.

[6] PIANO. S393 Details, oct 2010.
`http://controls.gsi.de/forschung/kp/kp2/piano/s393_print.html`. (accessed 5 Mars 2013).

[7] R. Thies. Prototype tests and pilot experiments for the R^{3}B scintillator-based detection systems. Master's thesis, Chalmers University of Technology, 2011.

[8] Expert team. Status report after exp. S393/S306 (25 Aug-17 Sep 2010), sep 2010.
`http://www-wnt.gsi.de/frs/experiments/new/images/S393-S306_status.pdf`. (accessed 24 Apr. 2013).

[9] FRS website: S393/S306.
`http://www-w2k.gsi.de/frs/experiments/new/s393.asp`.
(accessed 24 Apr. 2013).

[10] H. Geissel, P. Armbruster, K. Behr, et al. The GSI projectile fragment separator (FRS): a versatile magnetic system for relativistic heavy ions. *Nuclear Instruments and Methods in Physics Research Section B: Beam Interactions with Materials and Atoms*, 70(1–4):286 – 297, 1992.
`http://www.sciencedirect.com/science/article/pii/0168583X9295944M`.

[11] The land group. land02 — the unofficial guide, 2013.
`http://web-docs.gsi.de/~rplag/land02/index.php`. (accessed 16 May 2013).

[12] J. Allison, K. Amako, J. Apostolakis, et al. Geant4 developments and applications. *IEEE Transactions on Nuclear Science*, 53(1):270 –278, Feb. 2006.

[13] Wikipedia. Binary space partitioning — Wikipedia, The Free Encyclopedia, 2013.
`http://en.wikipedia.org/w/index.php?title=Binary_space_`
`partitioning&oldid=542008108`. (accessed 5 March 2013).

[14] H. Kurashige. How to Specify Physics Processes.
`http://geant4.web.cern.ch/geant4/G4UsersDocuments/UsersGuides/`
`ForApplicationDeveloper/html/GettingStarted/physicsDef.html`.
(accessed 6 May 2013).

[15] A. Ribon. Geant4 physics: issues, progress, development. Presented at LPCC Detector Simulation Workshop, Oct 2011.
`http://indico.cern.ch/getFile.py/access?contribId=24&sessionId=`
`2&resId=0&materialId=slides&confId=144956`. (accessed 4 Mars 2013).

[16] H. Johansson. ggland - command-line simulation wrapper, Apr 2013.
`http://fy.chalmers.se/~f96hajo/ggland/`.

[17] R. Plag. Current status of: Tracking at the LAND/R3B setup. Given as talk at the S393/land02 November 2011 workshop, nov 2011.
`http://web-docs.gsi.de/~rplag/land02/docs/workshop_1111/`
`tracking-land02-workshop2011-pdf.pdf`.
(accessed 18 May 2013).

[18] R. Plag. Some documentation on Ralf's tracker, apr 2013.
`http://ralfplag.de/tracker/`.
(accessed 6 May 2013).

[19] The ROOT Team. ROOT | A Data Analysis Framework, 2013.
`http://root.cern.ch/drupal/`. (accessed 8 May 2013).

[20] Reference Physics Lists, mar 2013.
`http://geant4.cern.ch/support/proc_mod_catalog/physics_lists/`
`referencePL.shtml`.
(accessed 6 May 2013).

[21] J. Beringer, J. F. Arguin, R. M. Barnett, et al. Review of Particle Physics. *Phys. Rev. D*, 86:010001, Jul 2012. http://link.aps.org/doi/10.1103/PhysRevD.86.010001.

[22] ALADiN Collaboration, 2000.
`http://www-aladin.gsi.de/www/pictures/s114/s114_col.gif`. (accessed 19 May 2013).

[23] NUSTAR Collaboration, 2013.
`http://www.fair-center.eu/typo3temp/pics/4f8a5fd757.jpg`. (accessed 19 May 2013).

50

[24] The land group. land02 — the unofficial guide, 2010.
`http://web-docs.gsi.de/~rplag/land02/index.php?page=detectors/dtf/`
`dtf`. (accessed 19 May 2013).

[25] J. Cuba, G. Stengel, A. Gtinschlofiß, et al. A large-area scintillating fibre detector
for relativistic heavy ions. *Nuclear Instruments and Methods in Physics Research
A*, 402:010001, Jan 1998.
`http://dx.doi.org/10.1016/S0168-9002(97)01078-4`.

[26] The land group. land02 — the unofficial guide, 2011.
`http://web-docs.gsi.de/~rplag/land02/index.php?page=detectors/ntf/`
`ntf`. (accessed 19 May 2013).

[27] Christine. PDC_LAND02_workshop-2, 2009.
`http://web-docs.gsi.de/~rplag/land02/workshop_0509/PDC_LAND02_`
`workshop.ppt`. (accessed 19 May 2013).

[28] The land group. land02 — the unofficial guide, 2008.
`http://web-docs.gsi.de/~rplag/land02/index.php?page=detectors/pos/`
`pos`. (accessed 19 May 2013).

[29] The land group. land02 — the unofficial guide, 2012.
`http://web-docs.gsi.de/~rplag/land02/index.php?page=detectors/rolu/`
`rolu`. (accessed 19 May 2013).

[30] The land group. land02 — the unofficial guide, 2009.
`http://web-docs.gsi.de/~rplag/land02/index.php?page=detectors/ssd/`
`ssd`. (accessed 19 May 2013).

A. Approximating the Magnetic Rigidity

This section is dedicated to the calculation of the constant $b\rho$, the magnetic rigidity, used in the simulations to get the fragments into the fragment arm. The correlation between the current put into ALADiN and $b\rho$ is also calculated here, for currents ranging from $2300\,\text{A}$ to $2500\,\text{A}$.

A.1. Analytical Solution

To make analytical calculations feasible, the magnetic field generated by ALADiN is taken to be enclosed in a cuboid. The magnetic field is also taken to be homogenous and only acting in the (positive) y-direction, for simplicity. For the full geometry considered, see Figure A.1. A good starting point is to get a grip on what it is we are looking for. We want to be able to express the angle of deflection of a positively charged particle in terms of the known parameters. For a full list of these, see Table A.1.

As previously stated, the magnetic field we consider is

$$\boldsymbol{b} = b\hat{\boldsymbol{y}} \tag{A.1}$$

with b being the magnetic field strength. The magnetic field is centred along the z-axis, at z_0 and the enclosing cuboid is rotated around the negative y direction by the angle θ_A. To avoid having to take heed to a large number of restrictions, and the tedious work of calculating these, we assume that the cuboid is only limited in the z direction (before

Table A.1.: *A list of the known parameters. They are described in the text and some of them can also be found in Figure A.1.*

Parameters		
z_0	ϕ_A	θ_A
θ	ϕ	v
m	q	b

rotation) with a length of d_z. The consideration of other fields such as gravitation is omitted.

The considered particle emerges from the target located in the origin with a (known) initial velocity

$$\boldsymbol{v} = v(\cos\phi\sin\theta\hat{\boldsymbol{x}} + \sin\phi\sin\theta\hat{\boldsymbol{y}} + \cos\theta\hat{\boldsymbol{z}}) \tag{A.2}$$

where θ and ϕ are the standard spherical angles (θ being the polar angle and ϕ the azimuthal angle) whereas v is the velocity of the particle. The particle is hereafter considered to be massive and carry a charge, as a neutral particle would be unaffected by the magnetic field. Relativistic effects are taken into account as the speed of the particles considered is close to the speed of light (that is $v \gtrsim 0.1c$)

Given the geometry of the problem, it is easiest to consider it in the xz plane and only afterwards calculate the y components, as the velocity of the particles along the y-axis will remain unchanged throughout the entire trace. We therefore make use of the angle of emergence of the particle projected on the xz plane, φ, defined by

$$\tan\varphi = \cos\phi\tan\theta \,. \tag{A.3}$$

The first step is now to aquire the point of entry into the magnetic field. We do this by first calculating a few geometric distances marked in Figure A.1. Namely z_1, the distance from target to the magnetic field along the z-axis, and x_0, the distance along the field border between the point of entry and the z-axis.

It is easily shown that

$$z_1 = z_0 - \frac{d_z}{2\cos\theta_A} \tag{A.4}$$

and with some trigonometry

$$x_0 = \frac{\sin\varphi}{\cos(\varphi + \theta_A)}z_1 \,. \tag{A.5}$$

The point of entry, $\boldsymbol{x}_0$, can thus be written as

$$\boldsymbol{x}_0 = x_0\cos\theta_A\hat{\boldsymbol{x}} + y_0\hat{\boldsymbol{y}} + (z_1 + x_0\sin\theta_A)\hat{\boldsymbol{z}} \,. \tag{A.6}$$

We can quickly determine the y_0 component by multiplying the particles travelled distance in the xz plane with a scaling factor, which has a θ and ϕ dependence. This factor can be extracted from the particles angle of emergence (eq. A.2) and we yield

$$y_0 = \frac{\sin\phi\sin\theta}{\sqrt{1 - \sin^2\theta\sin^2\phi}}\sqrt{x_0^2 + z_1^2 + 2x_0z_1\sin\theta_A} \,, \tag{A.7}$$

where the fraction is the scaling factor after simplifications and the square root comes from the travelled distance.

The next step is to aquire the particles trajectory within the magnetic field. Given that the speed remains constant, the trajectory is fully determined by a radius, ρ, and the centre of the circular motion. As the magnitude of the force acting on the particle by the magnetic field equals the centripetal force, we aquire both the radius of the motion
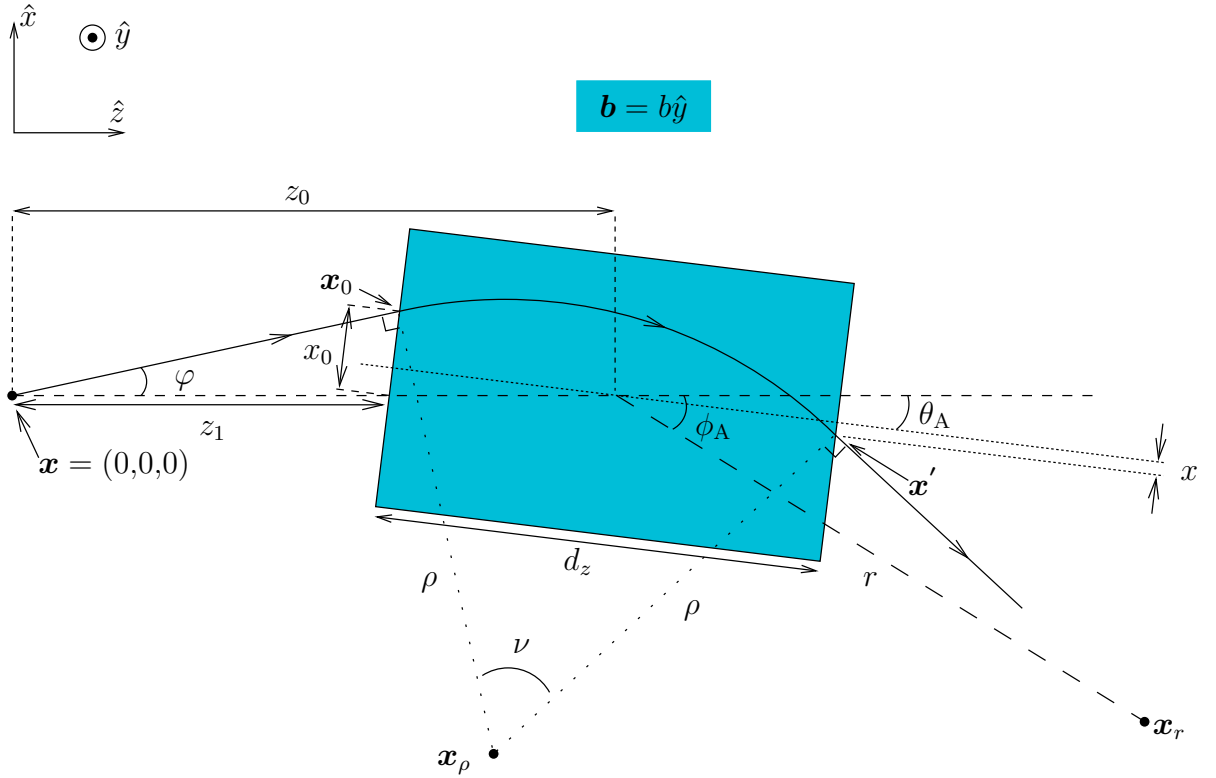
Figure A.1.: *A schematic drawing of a charged particle travelling from the target through a magnetic field. The magnetic field is enclosed in a cuboid, rotated about its centre by an angle θ_A, the centre being located a distance z_0 away from the target along the z-axis. The particle bends off in the magnetic field by an angle ν and with a radius of curvature ρ. The fragment arm is located along the line with long dashes, ending with the TFW at $\boldsymbol{x}_r$. The arm is rotated around the centre of the cuboid, making an angle, ϕ_A, with the z-axis.*

as well as the direction towards the centre (from the point of entry). Keep in mind, however, that the speed we have to consider is the speed projected on the xz plane. We do as follows

$$|\boldsymbol{F}| = qb|\boldsymbol{v} \times \boldsymbol{\hat{y}}| = qbv| - \cos\theta\boldsymbol{\hat{x}} + \cos\phi\sin\theta\boldsymbol{\hat{z}}| =$$

$$qbv\sqrt{1 - \sin^2\theta\sin^2\phi} = m\frac{v^2}{\rho}(1 - \sin^2\theta\sin^2\phi) \Rightarrow$$

$$\rho = \frac{mv}{qb}\sqrt{1 - \sin^2\theta\sin^2\phi}\,, \tag{A.8}$$

where q is the charge of the particle and m its relativistic mass. Hereafter, we require q to be positive. We now also get the centre of motion, $\boldsymbol{x}_\rho$, in the xz plane by the following translation.

$$\begin{aligned} \boldsymbol{x}_\rho &= \boldsymbol{x}_0 + \rho \frac{\boldsymbol{F}}{|\boldsymbol{F}|} \\ &= (x_0 \cos\theta_A - \frac{mv}{qb}\cos\theta)\hat{\boldsymbol{x}} + (z_1 + x_0\sin\theta_A + \frac{mv}{qb}\cos\phi\sin\theta)\hat{\boldsymbol{z}} \\ &= x_\rho \hat{\boldsymbol{x}} + z_\rho \hat{\boldsymbol{z}}\,, \end{aligned} \qquad (A.9)$$

where we have introduced the parameters x_ρ and z_ρ to simplify further calculations.

To calculate the point of exit, $\boldsymbol{x}'$, we need an expression for the backmost boundary of the magnetic field, still in the xz plane. By remembering that the magnetic field is rotated about $z_0\hat{\boldsymbol{z}}$ by the angle θ_A, this can be achieved by applying a proper rotational matrix to the straight line $x\hat{\boldsymbol{x}} + dz/2\hat{\boldsymbol{z}}$ and then translating, where x is a parameter along the boundary which needs to be determined. The rotational matrix, A, is written as

$$A = \begin{pmatrix} \cos\theta_A & \sin\theta_A \\ -\sin\theta_A & \cos\theta_A \end{pmatrix}. \qquad (A.10)$$

This will rotate a vector of the form $\begin{bmatrix} x & , & z \end{bmatrix}^{\mathrm{T}}$ counterclockwise. Applying it to the already mentioned line will rotate it about the centre of the magnetic field. The necessary translation is thus only $z_0\hat{\boldsymbol{z}}$ and we have

$$\begin{aligned} \boldsymbol{x}' &= A \begin{bmatrix} x \\ dz/2 \end{bmatrix} + \begin{bmatrix} 0 \\ z_0 \end{bmatrix} \\ &= (x\cos\theta_A - \frac{d_z}{2}\sin\theta_A)\hat{\boldsymbol{x}} + (z_0 + \frac{d_z}{2}\cos\theta_A + x\sin\theta_A)\hat{\boldsymbol{z}} \\ &= x'\hat{\boldsymbol{x}} + z'\hat{\boldsymbol{z}}\,, \end{aligned} \qquad (A.11)$$

where we again have introduced two new parameters, x' and z', for later convenience.

The next step is to decide what value x has, which then will give us the point of exit through Equation A.11. We do this by requiring that the distance between the point of exit and the centre of motion is the radius ρ. That is

$$|\boldsymbol{x}' - \boldsymbol{x}_\rho| = \rho \qquad (A.12)$$

$$\Rightarrow \rho^2 = (x' - x_\rho)^2 + (z' - z_\rho)^2\,. \qquad (A.13)$$

By defining

$$x'_\rho = x_\rho + \frac{d_z}{2}\sin\theta_A, \quad z'_\rho = z_\rho - z_0 - \frac{d_z}{2}\cos\theta_A \qquad (A.14)$$

we get

$$\begin{aligned} (A.13): \qquad 0 &= (x\cos\theta_A - x'_\rho)^2 + (x\sin\theta_A - z'_\rho)^2 - \rho^2 \\ &= x^2 - 2(x'_\rho\cos\theta_A + z'_\rho\sin\theta_A)x + x'^2_\rho + z'^2_\rho - \rho^2 \end{aligned} \qquad (A.15)$$

with the solutions

$$x = x'_\rho \cos\theta_A + z'_\rho \sin\theta_A \underset{(\mp)}{\pm} \sqrt{(x'_\rho \cos\theta_A + z'_\rho \sin\theta_A)^2 + \rho^2 - (x'^2_\rho + z'^2_\rho)}\,. \qquad \text{(A.16)}$$

The negative solution, for our case of a positive particle, corresponds to the re-entry into the magnetic field if the particle continues on the circular path even after exiting the field, and is therefore neglected.

The total angle of deflection, ν, from the particles initial trajectory is now calculated by utilizing the scalar product between the two vectors $(\boldsymbol{x}_0 - \boldsymbol{x}_\rho)$ and $(\boldsymbol{x}' - \boldsymbol{x}_\rho)$. That is, the vectors stretching from $\boldsymbol{x}_\rho$ to the point of entry and the point of exit respectively. We have

$$\begin{aligned}
\cos\nu &= \frac{(\boldsymbol{x}_0 - \boldsymbol{x}_\rho) \cdot (\boldsymbol{x}' - \boldsymbol{x}_\rho)}{\rho^2} \\
&= \frac{1}{\rho^2}\frac{mv}{qb}(\cos\theta\hat{\boldsymbol{x}} - \cos\phi\sin\theta\hat{\boldsymbol{z}}) \cdot ((x' - x_\rho)\hat{\boldsymbol{x}} + (z' - z_\rho)\hat{\boldsymbol{z}})\,.
\end{aligned} \qquad \text{(A.17)}$$

Using Equation A.9 and A.11, and simplifying, we aquire

$$\begin{aligned}
\cos\nu = \frac{1}{\rho^2}\frac{mv}{qb}\Big(&\cos\theta\big((x - x_0)\cos\theta_A + \frac{mv}{qb}\cos\theta - \frac{d_z}{2}\sin\theta_A\big) \\
&- \cos\phi\sin\theta\big((x - x_0)\sin\theta_A - \frac{mv}{qb}\cos\phi\sin\theta + \frac{d_z}{2}(\cos\theta_A + \frac{1}{\cos\theta_A})\big)\Big)
\end{aligned} \qquad \text{(A.18)}$$

where x is taken as the positive root from Equation A.16. One quickly sees that writing out the full expression will not bring us any joy and since everything in the expression is known, we wont need to.

Only a few short steps remain. We can, similarly to what we did before, get the y coordinate of $\boldsymbol{x}'$ as a scaling factor (same as before) and the length of the curved path, which is simply the angle of deflection, ν, multiplied by the radius of curvature. This will then have to be added to the y coordinate of the entry point, $\boldsymbol{x}_0$,

$$y' = y_0 + \frac{\sin\phi\sin\theta}{\sqrt{1 - \sin^2\theta\sin^2\phi}}\nu\rho = y_0 + \frac{mv}{qb}\nu\sin\phi\sin\theta\,, \qquad \text{(A.19)}$$

where Equation A.8 was used in simplifying the expression.

To wrap things up, we also write down an expression for the particles velocity after it has exited the magnetic field. This is done similarly to what we did in getting Equation A.11. However, we need to take the angle to be the angle of deflection, ν, and we end up with

$$\begin{aligned}
\boldsymbol{v}' = v\Big(&(\cos\nu\cos\phi\sin\theta - \sin\nu\cos\theta)\hat{\boldsymbol{x}} + \sin\phi\sin\theta\hat{\boldsymbol{y}} \\
&+ (\cos\nu\cos\theta + \sin\nu\cos\phi\sin\theta)\hat{\boldsymbol{z}}\Big)\,,
\end{aligned} \qquad \text{(A.20)}$$

where ν can be found from Equations A.18 and A.16. Given the length of our final expression, some approximations are in order to aquire something useful. We proceed with this in the continuing sections.

A.2. Angular Approximations

In the S393 experiment, the spread of the beam is around $0.016\,\mathrm{rad}$. With this, we can make a large number of simplifications to the expressions in the previous section by the following approximation

$$\theta \approx 0 \Rightarrow \sin\theta \approx 0,\ \cos\theta \approx 1,\ \tan\theta \approx 0\,. \tag{A.21}$$

If we apply this, rather crude, approximation to Equation A.3 through A.6 we get

$$\tan\varphi = 0,\quad \varphi = 0,\quad x_0 = 0 \tag{A.22}$$

and

$$\boldsymbol{x}_0 = z_1\hat{\boldsymbol{z}} = z_0 - \frac{d_z}{2\cos\theta_A}\hat{\boldsymbol{z}}\,. \tag{A.23}$$

The radius, from Equation A.8, is now simply written as

$$\rho = \frac{mv}{qb} \tag{A.24}$$

along with the centre of motion, Equation A.9,

$$\boldsymbol{x}_\rho = -\frac{mv}{qb}\hat{\boldsymbol{x}} + \left(z_0 - \frac{d_z}{2\cos\theta_A}\right)\hat{\boldsymbol{z}} = x_\rho\hat{\boldsymbol{x}} + z_\rho\hat{\boldsymbol{z}} \tag{A.25}$$

and the point of exit, Equation A.11,

$$\boldsymbol{x}' = \left(x\cos\theta_A - \frac{d_z}{2}\sin\theta_A\right)\hat{\boldsymbol{x}} + \left(z_0 + \frac{d_z}{2}\cos\theta_A + x\sin\theta_A\right)\hat{\boldsymbol{z}} = x'\hat{\boldsymbol{x}} + z'\hat{\boldsymbol{z}}\,. \tag{A.26}$$

We get the equivalent of Equation A.14

$$x'_\rho = -\frac{mv}{qb} + \frac{d_z}{2}\sin\theta_A,\quad z'_\rho = -\frac{d_z}{2}\left(\frac{1}{\cos\theta_A} + \cos\theta_A\right) \tag{A.27}$$

and can now calculate the value of x from Equation A.16 by utilising the following simplified expression.

$$x'_\rho\cos\theta_A + z'_\rho\sin\theta_A = -\left(\frac{d_z}{2}\tan\theta_A + \frac{mv}{qb}\cos\theta_A\right)\,. \tag{A.28}$$

With this we get

$$x = -\left(\frac{d_z}{2}\tan\theta_A + \frac{mv}{qb}\cos\theta_A\right) \overset{(+)}{(-)} \sqrt{-d_z^2 + \left(\frac{mv}{qb}\cos\theta_A\right)^2 + 2d_z\frac{mv}{qb}\sin\theta_A}\,, \tag{A.29}$$

where Equation A.27 and A.24 were used in getting the final expression. As before, we only consider the positive root for our case of a particle, carrying a positive charge.

It can now also be shown that

$$
\begin{aligned}
\cos \nu &= \frac{(\boldsymbol{x}_0 - \boldsymbol{x}_\rho) \cdot (\boldsymbol{x}' - \boldsymbol{x}_\rho)}{\rho^2} \\
&= \sin^2 \theta_A - d_z \frac{qb}{mv} \sin \theta_A + \frac{qb}{mv} \cos \theta_A \sqrt{-d_z^2 + (\frac{mv}{qb} \cos \theta_A)^2 + 2d_z \frac{mv}{qb} \sin \theta_A} \\
&= \sin^2 \theta_A - \frac{d_z}{\rho} \sin \theta_A + \cos \theta_A \sqrt{-(\frac{d_z}{\rho})^2 + \cos^2 \theta_A + 2\frac{d_z}{\rho} \sin \theta_A} \ ,
\end{aligned}
\tag{A.30}
$$

by using Equation A.18 together with the positive root from Equation A.29.

We can now aquire a final expression for the required radius ρ to get the particle to deflect from its initial trajectory by an angle ν, in the approximation that the angular spread from target is very small.

$$
\rho = \frac{d_z}{\sin \theta_A + \sin \left((\underset{(-)}{\pm}) \nu - \theta_A \right)} \ .
\tag{A.31}
$$

The calculations in getting this expression from Equation A.30 are elementary but tedious, which is why the intermediate steps have been omitted. The two solutions come from the fact that the angle ν can be both positive and negative. If we require the angle to be positive and that the radius be positive as well, we end up with

$$
\rho = \frac{d_z}{\sin \theta_A + \sin (\nu - \theta_A)} \ .
\tag{A.32}
$$

A.3. Linear Correlation Between the Current and the Magnetic Field Strength

In the previous sections we acquired an expression for the ρ part of the magnetic rigidity, $b\rho$. In this Section we will finish up the calculations by establishing a linear relation between the current fed to ALADiN, I, and the magnetic field strength, b, from the previous sections.

The magnetic field felt by a particle, fired from target along the z-axis, as it passes through ALADiN can be seen in Figure A.2 for two different currents, 2500 A and 2300 A. It is in this interval that we will assume a linear relationship. The reason for this comes from the fact that field maps exist for these two currents and both the tracker and GGLAND use the very same assumption.

The particle used in the case presented in the figure was a ^{15}B nucleus, with the mass $m_0 = 15.00307$ u and charge $Ze = 5e$, e being the elementary charge. The speed of the particle, v_0, was in both cases calibrated as to give it an exit angle equal to ϕ_A, set to $15\,°$. This was easily done by simply having it centre on the TFW, located at $\boldsymbol{x}_r$ in Figure A.1. The radial distance between the centre of ALADiN and the centre of the TFW, r, was taken to be large enough as to make the angular discrepancy $\nu - \phi_A$ negligible.

The first step will be to correlate the current to some representative values of the magnetic field in ALADiN. We take these to be the maximum values of the magnetic field in the y direction experienced by the particle, shown in Figure A.2 as b_{2500} and b_{2300} for the respective currents. That is, we assume the entire magnetic field to scale the same way as these maximum values for varying currents. Thus, we get the relation

$$b_{\text{ALADiN}}(I) - b_{2500} = \left(\frac{b_{2500} - b_{2300}}{2500 - 2300}\right) \cdot (I - 2500) \Rightarrow$$

$$b_{\text{ALADiN}}(I) = \left(\frac{b_{2500} - b_{2300}}{200}\right) \cdot (I - 2500) + b_{2500} \,. \tag{A.33}$$

where $b_{\text{ALADiN}}(I)$ signifies the discussed maximum value at a given current. The parameters b_{2500} and b_{2300} are found to be

$$b_{2500} = 1.6593\,\text{T} \quad \text{and} \quad b_{2300} = 1.5828\,\text{T} \tag{A.34}$$

from the calibration runs shown in Figure A.2.

We now want to relate the magnetic field strength from ALADiN to the homogenous field strength, b from the previous sections. We do this by assuming that they are proportional with respect to each other. In doing this, we only need to calculate b from the known values for one of the calibration currents, using Equations A.32 and A.24. We end up with

$$b_{\text{hom}} = \frac{m_0 v_0}{Ze} \frac{\sin\theta_A + \sin(\nu - \theta_A)}{d_z} \tag{A.35}$$

where, apart from the aforementioned values, we use values from the 2500 A calibration. These are

$$v_0 = 0.6855c\,, \quad \nu \approx \phi_A = 15\,^\circ\,, \quad \theta_A = 7\,^\circ\,, \quad \text{and} \quad d_z = 2.42\,\text{m}\,, \tag{A.36}$$

where c is the speed of light and d_z has been taken to be the full length of ALADiN. Using these values we aquire

$$b_{\text{hom}} = 0.9487\,\text{T}. \tag{A.37}$$

Given that we used the values from the 2500 A calibration, we now get the relation between the homogenous magnetic field and the current

$$b(I) = \frac{b_{\text{hom}}}{b_{2500}} b_{\text{ALADiN}}(I) = \frac{b_{\text{hom}}}{b_{2500}}\left(\left(\frac{b_{2500} - b_{2300}}{200}\right) \cdot (I - 2500) + b_{2500}\right)$$

$$= \left(\left(1 - \frac{b_{2300}}{b_{2500}}\right)\frac{I - 2500}{200} + 1\right)b_{\text{hom}}\,. \tag{A.38}$$

We finally arrive at our final expression for the magnetic rigidity $b\rho$

$$b\rho = \frac{d_z}{\sin\theta_A + \sin(\nu - \theta_A)} \cdot \left(\left(1 - \frac{b_{2300}}{b_{2500}}\right)\frac{I - 2500}{200} + 1\right)b_{\text{hom}}. \tag{A.39}$$

By putting in values for the various constants in the equation we yield

$$b\rho = \frac{5.2925 \cdot 10^{-4}\,\frac{\text{T}}{\text{A}}I + 0.9728\,\text{T}}{\sin\theta_A + \sin(\nu - \theta_A)}. \tag{A.40}$$

A.4. The Magnetic Field of ALADiN

Given that the magnetic field is a vector field, there is no obvious way to present the magnetic field of ALADiN in the three spatial dimensions. However, what is of primary importance is the magnetic field felt by a particle travelling through ALADiN, which is what is presented in this section.
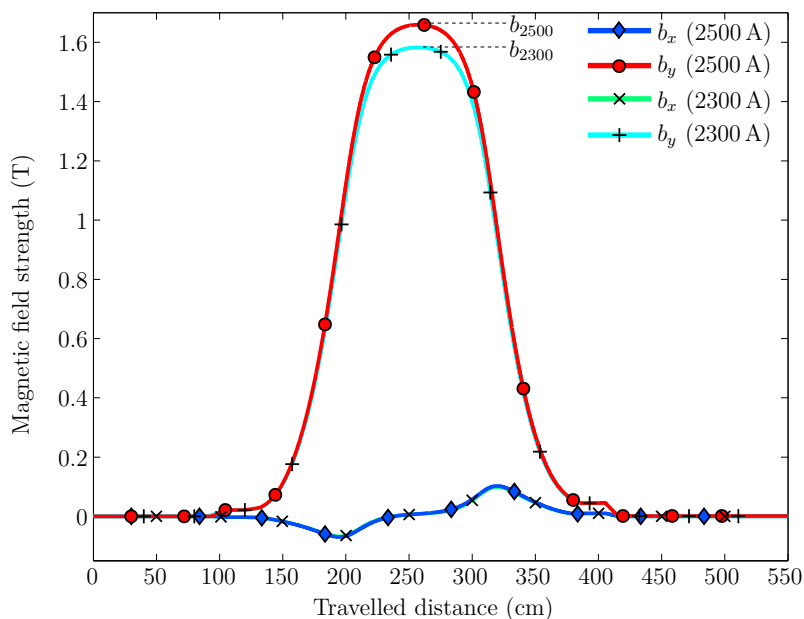
The magnetic field in the x-, y- and z-directions are presented in Figure A.2, as felt by a ^{15}B nucleus that travels through ALADiN, for the two currents, 2500 A and 2300 A. The nucleus initially trace the z-axis, where the axes are equivalent to those defined in Figure 3.2, and ALADiN is rotated $7°$. The initial speed of the nucleus is such that it hits the centre of the TFW located at the end of the fragment arm, which makes an angle of $15°$ with the z-axis.

It is, from the figures, possible to extract that the experienced field is not homogenous and that ALADiN actually generates quite notable fringe fields. Another important result is that the field in the x-direction is not negligible, whereas the field in the z-direction is several orders of magnitude smaller than that of the other two directions. However, as the integral over the magnetic field in the x-direction gets rather small, due to its change of sign and especially compared to the integral over the field in the y direction, it will not affect the particle's direction by much (again compared to that caused by the field in the y-direction).

Two equivalent simulations were made, but with ^{14}B nuclei with a magnetic rigidity of 6.56 Tm and 13.24 Tm respectively. These values were chosen so as to make the nuclei barely miss one detector while travelling through the others in the setup and it turns out that the detector it misses first is GFI2. This is, in a way, seen as the two extremes of when the particle traces a much desirable path, one that includes all detectors in the fragment arm.

The, by the particles, experienced magnetic fields in these two simulations are similar to the field shown in Figure A.2. In fact, they are so similar that they can not be told apart when drawn in the same figure. In light of this, the difference between the magnetic fields over travelled distance for the two simulations are presented in Figure A.3. Comparing these with Figure A.2 it is discovered that the experienced magnetic field hardly changes at all, as the difference is several orders of magnitude smaller than the corresponding fields.

Figure A.2.: *Magnetic field strength experienced by a ^{15}B nucleus travelling through AL-ADiN, for two different currents. The nucleus initially traces the z-axis. ALADiN is rotated $7°$ and the initial speed of the nucleus is such that it hits the centre of the TFW, located at a radial distance of $9\,m$ from ALADiN's centre. The fragment arm makes an angle of $15°$ with the z-axis. ...*

(a) ... The axes are equivalent to those defined in Figure 3.2.
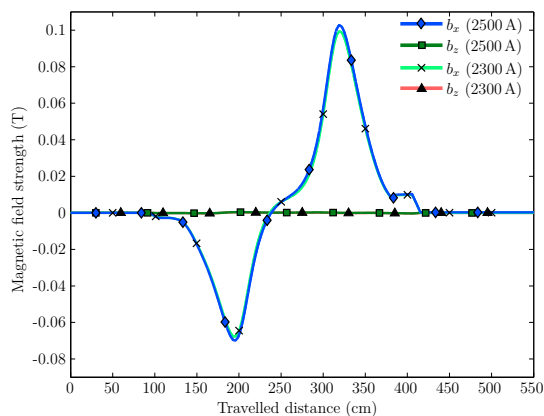
(b) ... The axes are equivalent to those defined in Figure 3.2 and it is a zoomed version of Figure A.3a but now looking at the magnetic field in the x and z directions.
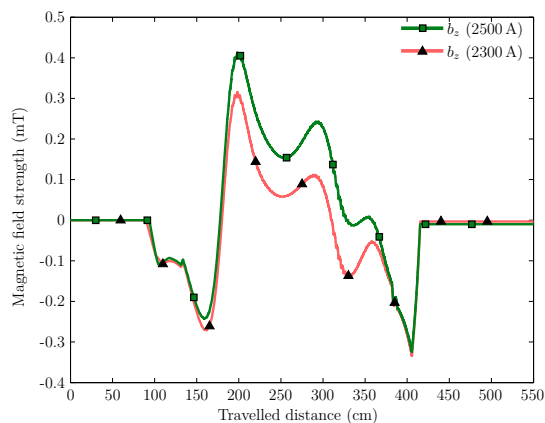
(c) ... The axes are equivalent to those defined in Figure 3.2 and it is a zoomed version of Figure A.3b but only looking at the magnetic field in the z direction.

Figure A.3.: *Difference between the magnetic field strengths experienced by two ^{14}B nuclei travelling through ALADiN, with a current of 2500 A. The geometry is the same as that specified in Figure 3.2. The magnetic field, b, felt by the particle with a bρ of 6.56 Tm and 13.24 Tm is given the index 1 and 2 respectively. The figure presents ...*
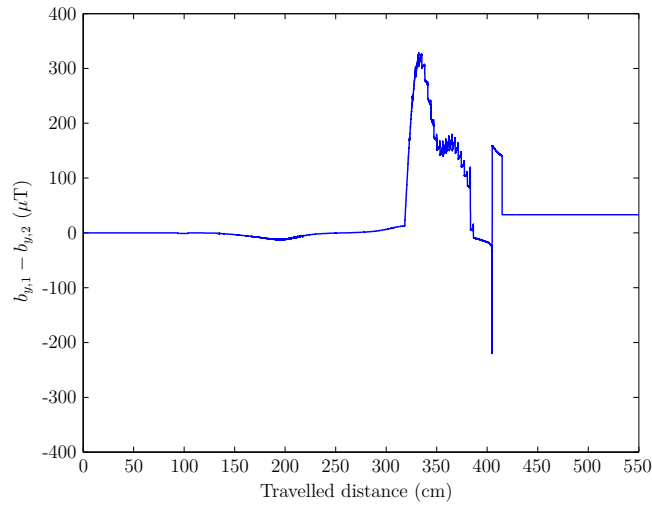
(a) ...the difference in the y component of the magnetic field.
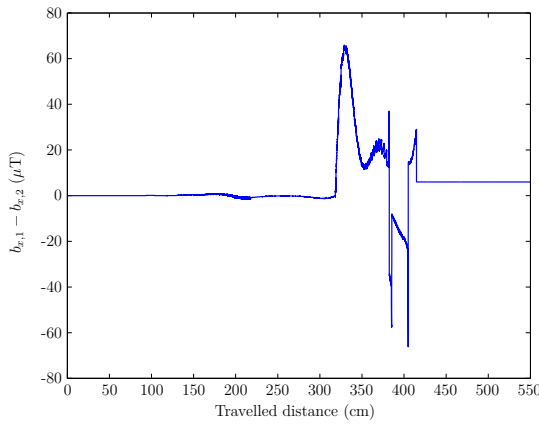
(b) ...the difference in the x component of the magnetic field.
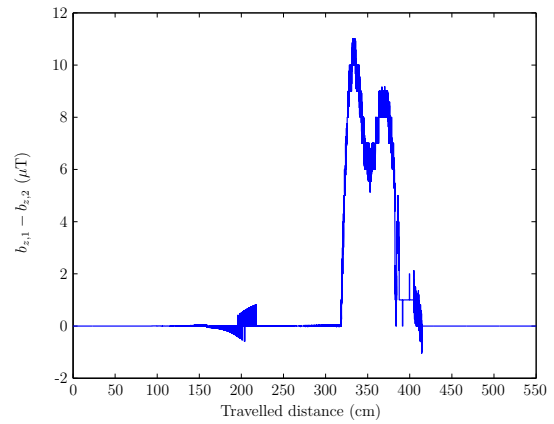
(c) ...the difference in the z component of the magnetic field.

B.   An Example Detector: POS

This appendix shows how to implement a simple but not trivial detector in GGLAND. The example given is the POS detector, the first detector we implemented. The source file for the detector should be saved as `geom_pos.cc`. Also, the `geom_pos.o` dependency needs to be added to the GGLAND makefile.

```
#define __STDC_FORMAT_MACROS
#include <inttypes.h>

#include "gg_geom_help.hh"
#include "detector_hit.hh"

#include "gg_tree.hh"      b2500  bx  (2500 A)
1.6  b2300
              by  (2500 A)

#include "gg_step.hh"
```

The detector parameters are declared inside a struct.

```
struct spec_POS_t
{
  SPEC_FLOAT(_dx,                2.5,"cm","full width x of active volume")
      ;
  SPEC_FLOAT(_dy,                2.5,"cm","full width y of active volume")
      ;
  SPEC_FLOAT(_dz,            0.03,"cm","full width z of active volume");
  SPEC_FLOAT(_lgheight,       2,"cm","lightguide height over active
      volume");
  SPEC_FLOAT(_lgheadd,      0.70,"cm","size of square-shaped lightguide-
      heads");
  SPEC_MEDIA(_type,     "plastic",""   ,"POS active volume material.");
  SPEC_MEDIA(_lgtype,  "plastic",""   ,"Lightguide material");
};


#include "auto_gen/spec_info_pos.hh"

#define UNUSED_PARAM(x)
```

This function is called when GGLAND creates the detector.

```
gg_geom_obj *make_POS(void *vspec, uint32_t UNUSED_PARAM(mask_set)
                      ,const transform_matrix *loc_rot
```

```
                            ,det_name_no_info *name_no)
  {
```

The vspec points to a `sepc_POS_t` object allocated by GGLAND.

```
    spec_POS_t *spec = (spec_POS_t *) vspec;
```

In order to place our volumes, we need to create a volume "mother volume" to contain daughter volumes. The `d_full` class is used to tell GGLAND that we are dealing with "diameters" rather than "radii".

```
    gg_geom_obj *goPOS=makebox("POS",_world_media_type
                            ,d_full(spec->_dx+2*spec->_lgheight)
                            ,d_full(spec->_dy+2*spec->_lgheight)
                            ,d_full(__max(spec->_lgheadd,spec->_dz)));
```

The POS detector has a cuboid in the middle that acts as active material. Therefore we create a box containing the active material.

```
    gg_geom_obj *goActive=makebox("POS", spec->_media_type,d_full(spec->
        _dx)
                            ,d_full(spec->_dy),d_full(spec->_dz) );
```

Around the cuboid, there are four trapetzoid lightguides that transmit light emitted from the active volume to photo multipliers. Since volumes can be rotated, it is enough to create two volumes.

```
    gg_geom_obj *goLgHorz = maketrd2("TRD1", spec->_media_lgtype,d_full(
        spec->_dz)
                                    ,d_full(spec->_lgheadd), d_full(spec
                                        ->_dy)
                                    ,d_full(spec->_lgheadd)
                                    ,d_full(spec->_lgheight));

    gg_geom_obj *goLgVert = maketrd2("TRD2", spec->_media_lgtype,d_full(
        spec->_dz)
                                    ,d_full(spec->_lgheadd),d_full(spec->
                                        _dx)
                                    ,d_full(spec->_lgheadd)
                                    ,d_full(spec->_lgheight));
```

Now place and rotate all volumes into the mother volume. Note that the rotation matrices are owned by GGLAND.

```
    posvol(goActive,4,goPOS,0.,0.,0.);

    gg_rot_obj  *lg0rot=makezyzrotm(M_PI/2, 0.,  0.);
    posvol(goLgHorz,0,goPOS,1*spec->_dx/2 +1*spec->_lgheight/2,0.,0.,
        lg0rot);

    gg_rot_obj  *lg1rot=makezyzrotm(-M_PI/2, 0.,  0.);
    posvol(goLgHorz,1,goPOS,-1*spec->_dx/2 -1*spec->_lgheight/2,0.,0.,
        lg1rot);

    gg_rot_obj  *lg2rot=makezyzrotm(M_PI/2,-M_PI/2,0.);
```

```
posvol(goLgVert,2,goPOS,0.,−1∗spec−>_dy/2 −1∗spec−>_lgheight/2,0.,
    lg2rot);

gg_rot_obj  ∗lg3rot=makezyzrotm(−M_PI/2,−M_PI/2,0.);
posvol(goLgVert,3,goPOS,0.,1∗spec−>_dy/2 +1∗spec−>_lgheight/2,0.,
    lg3rot);
```

Place the mother volume into the world. The argument `name_no` contains a unique identifier identifying this detector.

```
place_in_world(goPOS,loc_rot,name_no);
```

Finally, make GGLAND collect events detected in this detector, and return its mother volume.

```
collect_tree_vol_info ∗collect_info=register_collect_tree_id(name_no
    ,1);
collect_tree_reduced_vars(collect_info
    ,COL_TREE_VAR_T | COL_TREE_VAR_E | COL_TREE_VAR_X |
        COL_TREE_VAR_Y);

vect_step_copyno_path path;

register_step(goActive,NULL,collect_info,&path);

return goPOS;
}
```

C. Obstacles Defined in GGLAND

In this Appendix, obstacles are presented as they are defined in GGLAND along with a list of variables with default values. The obstacles presented are those implemented as a part of this project, hence the exclusion of LAND and XB. The illustrations are constructed to show all features of the geometry of an obstacle, rather than being scale accurate.

The obstacles in GGLAND are only approximations of the actual obstacles using simple geometric shapes. Most of them lack geometry for read-out electronics and other non-active parts. Obstacles that have such features are ALADiN, which only consists of non-active material, and POS, whose lightguides are implemented.

Given that not all specifications are well documented, some data has been taken from personal communications with Ronja Thies. Information given by her has been marked with a †. Some measurements have been improvised, these have been marked with a *.

C.1. ALADiN — A LArge DIpole magNet

ALADiN is a large dipole magnet with a core made of iron, surrounding a tube for particles to pass through. The tube can be filled with gas other than air to make interaction less likely. In reality, the tube is a trapezoid. In the model, the trapezoid is approximated by a cuboid with a width taken as the average width of the trapezoid.

Measurements for ALADiN were obtained by combining pixel counts from two pictures. For the top view, a technical drawing with a resolution of 59 px/m was used [22]. For the front view, a photograph with ALADiN in the background was used [23]. To get something meaningful from the picture, it was deformed to compensate for the perspective view. The width and depth of ALADiN were then measured and the height was calculated to preserve the aspect ratio for the perspective corrected image. From this procedure, it follows that the values of the width and depth of ALADiN are more accurate than those of the height.

66
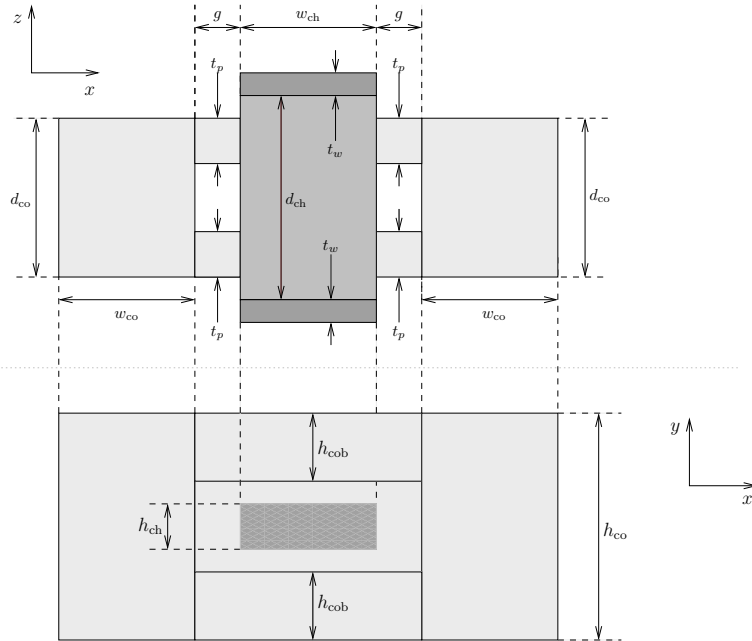
Key	Parameter	Default value
w_{co}	core_width	93 cm [a]
d_{co}	core_depth	176 cm [a]
h_{co}	core_height	266 cm [b]
h_{cob}	core_height_bar	50 cm [b]
t_p	core_thickness_plate	3 cm [a]
	core_type	Fe *
w_{ch}	chamber_width	138 cm [a]
d_{ch}	chamber_depth	242 cm [a]
h_{ch}	chamber_height	81 cm [b]
g	chamber_gap	46 cm [a]
	chamber_type	He *
t_w	chamber_window_thickness	0.0005 cm *
	chamber_window_type	plastic *

---

[a]This measurement was from reference [22].

[b]This measurement was from reference [22] and [23].

C.2. DTF — Dicke ToFWand

DTF is a row of vertical scintillator paddles inside a thin wrapping. Data without note are taken from *land02 — the unofficial guide* [24].
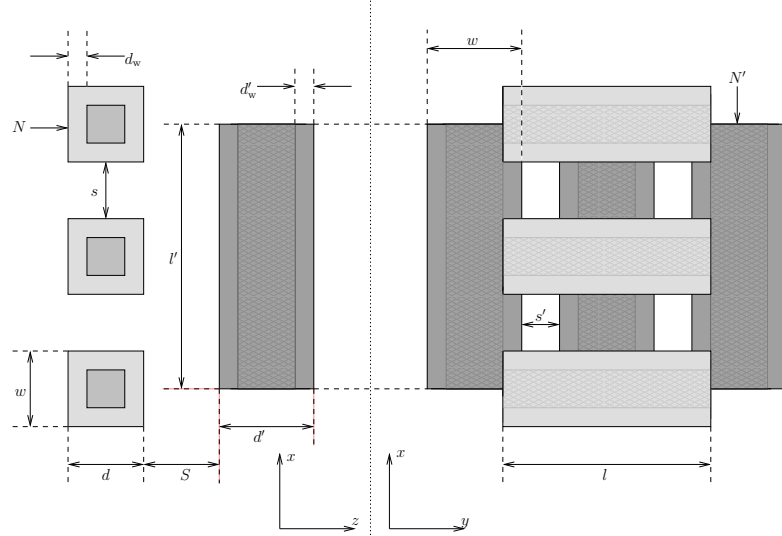
Key	Parameter	Default value
w'	paddle_width1	20 cm
d'	paddle_depth1	1.5 cm
l'	paddle_length1	120 cm
s'	paddle_spacing1	0.3 cm [a]
d'_{w}	paddle_wrapping1	0.3 cm *
N'	paddles1	6
■	type1	plastic *
■	wrapping_type1	plastic *
w	paddle_width2	10.4 cm
d	paddle_depth2	0.5 cm
l	paddle_length2	140 cm
s	paddle_spacing2	43 cm [a]
d_{w}	paddle_wrapping2	0.2 cm *
N	paddles2	3
■	type2	plastic *
■	wrapping_type2	plastic *
S	plane_spacing	1 cm *

---

[a]This measurement approximated from pictures at *land02 — the unofficial guide* [22] using similar techniques as mentioned in Section C.1.

C.3. GFI — Großer FIberdetektor

GFI is a row of vertical scintillator fibers inside a thin wrapping. Data without note are taken from Cuba et.al. [25].

Key	Parameter	Default value
w	fiber_width	0.1 cm
d	fiber_depth	0.1 cm
h	fiber_height	50 cm
d_s	fiber_spacing	0.005 cm [†]
N	fibers	475
▨	type	plastic [†]
▧	wrapping_type	plastic [†]

C.4. NTF — New Time-of-Flight wall

NTF is a row of vertical scintillator paddles inside a thin wrapping. Data without note are taken from *land02 — the unofficial guide* [26].
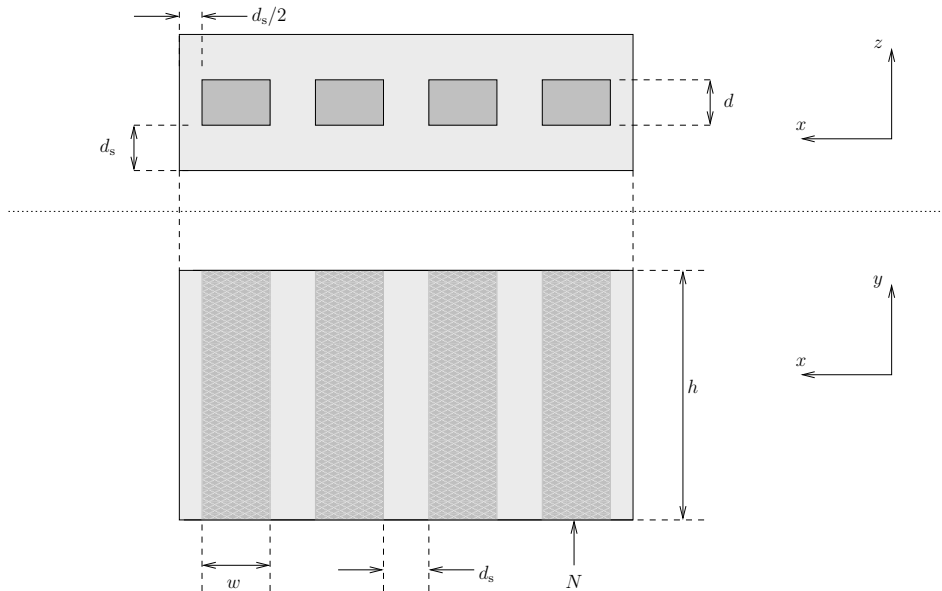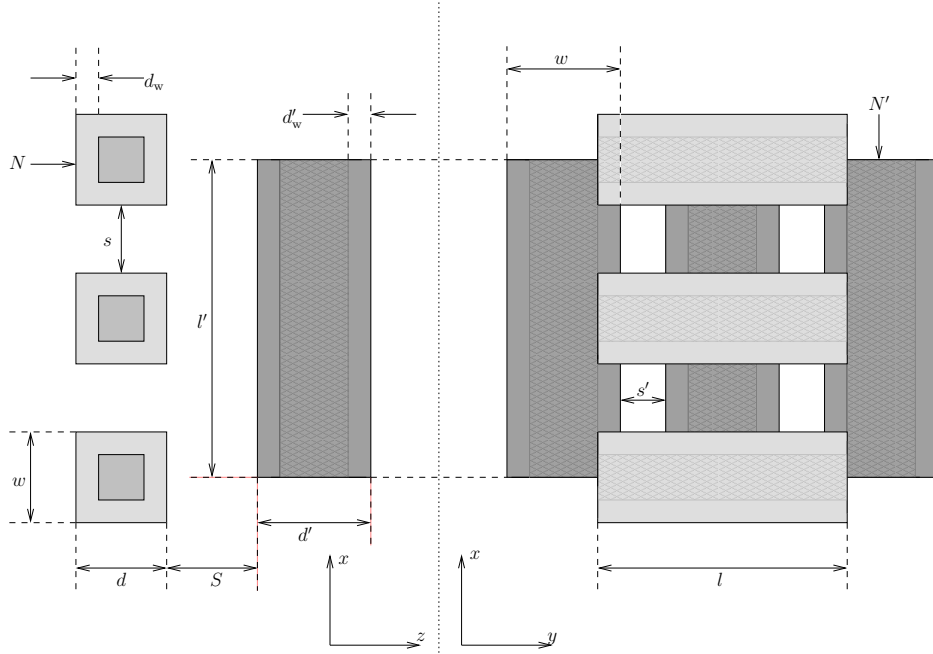

Key	Parameter	Default value
w'	paddle_width1	6 cm
d'	paddle_depth1	0.5 cm
l'	paddle_length1	48 cm
s'	paddle_spacing1	0.2 cm *
d'_{w}	paddle_wrapping1	0.05 cm *
N'	paddles1	8
■	type1	plastic †
■	wrapping_type1	plastic *
w	paddle_width2	6 cm
d	paddle_depth2	0.5 cm
l	paddle_length2	48 cm
s	paddle_spacing2	0.2 cm *
d_{w}	paddle_wrapping2	0.05 cm *
N	paddles2	8 □
■	type2	plastic †
■	wrapping_type2	plastic *
S	plane_spacing	1 cm *

C.5. PDC — Proton Drift Chamber

A PDC is a collection of charged long wires in a hexagonal pattern inside a gas chamber. The thicker wires are positively charged to attract released electrons from ionized atoms in the gas. The field near the wires is strong enough to accelerate the electrons sufficiently to ionize other atoms, causing detectable current pulses in the thicker, positively charged wires.

In reality, the active gas volume is surrounded by dead material to contain the gas and regulate the preassure. There are also two sets of wires, turned about 90° around the beam axis relative to each other in order to give the x and y coordinates of a particle passing through.

The square grid in the illustration represents the repeated building blocks of the detector. Data without note are taken from *PDC_LAND02_workshop-2* [27].
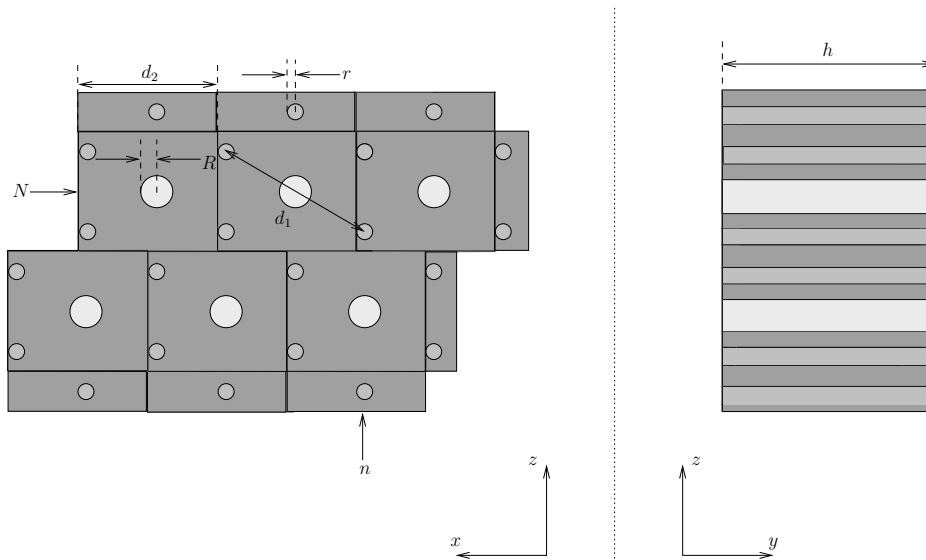
Key	Parameter	Default value
d_1	d1	1.6 cm
d_2	d2	1.6 cm
h	cell_height	80 cm
n	n_cells_plane	144
N	n_planes	2
r	r_w1	0.01 cm
▦	type_w1	Cu *
R	r_w2	0.02 cm
▢	type_w2	Cu *
▦	type_cell	Ar

C.6. POS — POSition detector

The POS detector is a thin sheet of scintillator material with a lightguide at each end orthogonal to the beam axis. Data without note is taken from *land02 — the unofficial guide* [28].
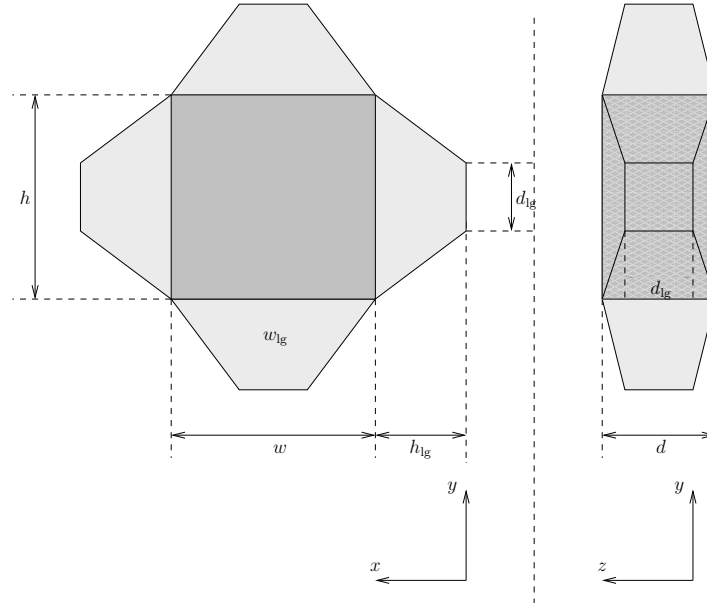
Key	Parameter	Default value
w	dx	2.5 cm
h	dy	2.5 cm
d	dz	0.03 cm [†]
d_{lg}	lgheight	0.1 cm [*]
h_{lg}	lgheadd	0.04 cm [*]
▮	type	plastic
▯	lgtype	plastic [*]

C.7. ROLU — Rechts, Oben, Links, Unten

ROLU are two pairs of scintillator plates that can be moved independently to define a gap which the beam has to pass through. The measurements are taken from *land02 — the unofficial guide* [29].

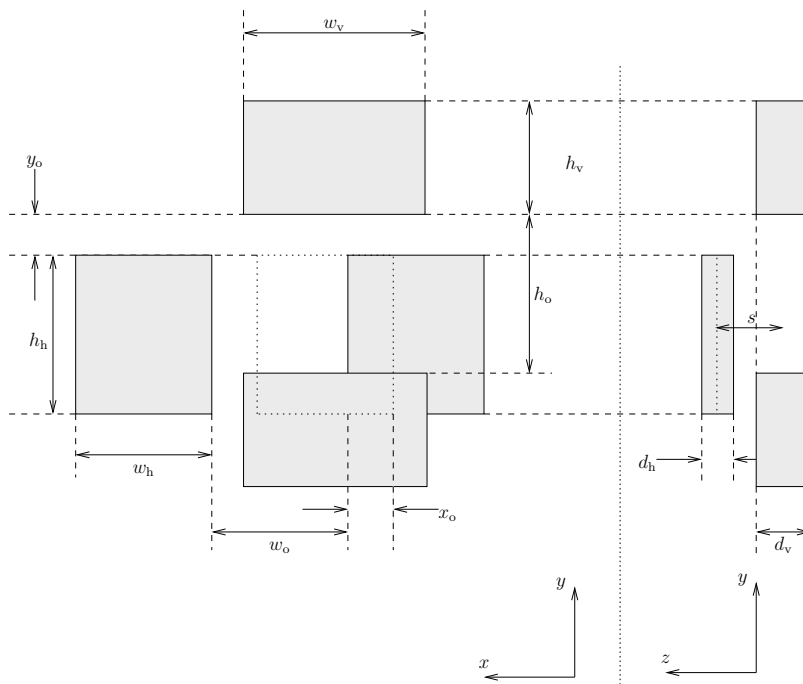| Key	Parameter	Default value
w_{v}	`dx_v`	$10\,\mathrm{cm}$
h_{v}	`dy_v`	$9.5\,\mathrm{cm}$
d_{v}	`dz_v`	$0.5\,\mathrm{cm}$
w_{h}	`dx_h`	$9.5\,\mathrm{cm}$
h_{h}	`dy_h`	$10\,\mathrm{cm}$
d_{h}	`dz_h`	$0.5\,\mathrm{cm}$
x_{o}	`offset_x`	$0\,\mathrm{cm}$
y_{o}	`offset_y`	$0\,\mathrm{cm}$
s	`space`	$1\,\mathrm{cm}$
h_{o}	`opening_v`	$2\,\mathrm{cm}$
w_{o}	`opening_h`	$2\,\mathrm{cm}$
	`type`	plastic

C.8. SST — Silicon STrip detecors

SST is a thin slab of silicone divided into many sections by the segmentation of the read-out electrodes. This segmentation is represented by the square grid in the illustration. The material surrounding the grid on the right hand side of the illustration is a dead-layer. The measurements are taken from *land02 — the unofficial guide* [30].
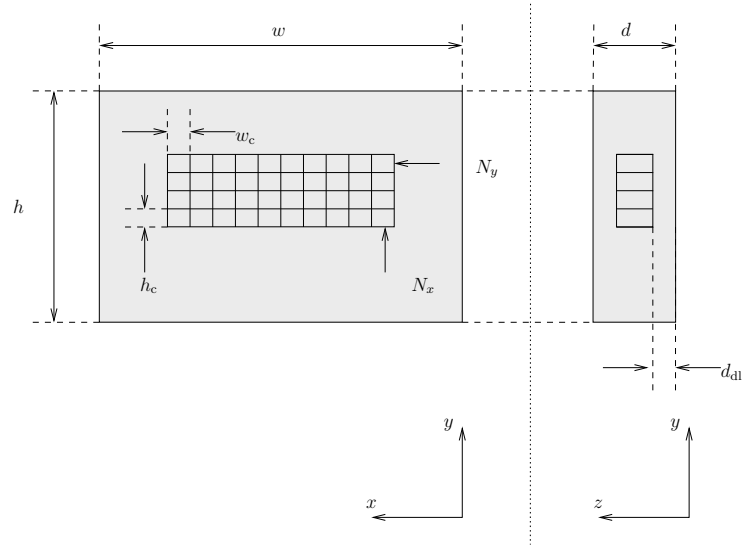
Key	Parameter	Default value
w	width	7.2 cm
h	height	4.0 cm
d	thickness	0.03 cm
d_{dl}	deadlayer	0.001 cm *
w_{c}	pitchx	0.0104 cm
h_{c}	pitchy	0.00275 cm
N_y	stripsx	384
N_x	stripsy	640
▢	type	Si

C.9. TFW — Time of Flight Wall

The TFW consists of 2 planes of scintillator paddles. One plane has horizontal paddles while the other has vertical, giving the x and y coordinates of the detected particles.
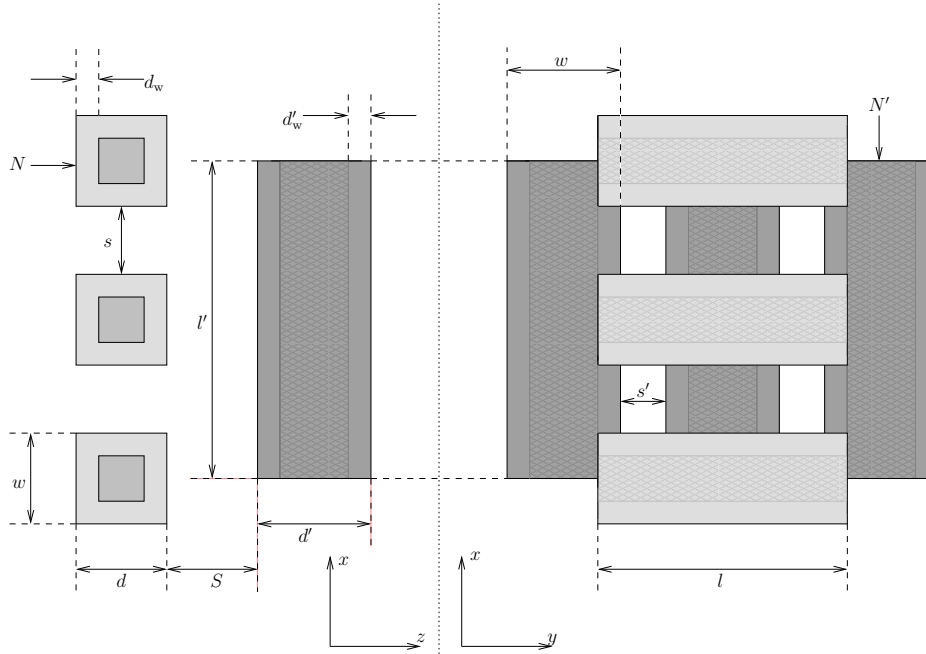
Key	Parameter	Default value
w'	paddle_width1	10 cm †
d'	paddle_depth1	0.5 cm †
l'	paddle_length1	147 cm †
s'	paddle_spacing1	0.2 cm †
d'_w	paddle_wrapping1	0.001 cm *
N'	paddles1	18 †
■	type1	plastic *
■	wrapping_type1	plastic *
w	paddle_width2	10 cm †
d	paddle_depth2	0.5 cm †
l	paddle_length2	189 cm †
s	paddle_spacing2	0.2 cm †
d_w	paddle_wrapping2	0.001 cm *
N	paddles2	14 †
■	type2	plastic *
■	wrapping_type2	plastic *
S	plane_spacing	1 cm *

D. Function Used to Calibrate RALF'S TRACKER

Below is a C++ function that can be used to run our calibration scheme found in Section 5.3.2, where all steps listed below are described in common language. `output` is a handle to a log file. The `ProgramData` object contains information used to communicate with the tracker as well as, nuclei masses, and methods for calling the tracker. The `string_format` function is a `sprintf` variant for C++ strings. `ResourceManager` is a class that helps to clean up resources.

```cpp
bool calibrate(FILE* output, ProgramData& data, unsigned int Z, unsigned
    int A)
{
```

D.1. Preparation

```cpp
    std::string filename_in=...; //your file that contains data to
        calibrate for
    std::string filename_out=...; //temporary output file

    double mass=data.masses->massGet(Isotope(Z,A))/Constants::mev;
    double brho=8.7; //Tm
    double beta=betaGet(Z,mass*Constants::u,brho);
    data.experiment->variableCustomGet("Inbeta").x=beta;
    data.experiment->variableCustomGet("Truebeta").x=beta;
    data.experiment->variableCustomGet("Truebeta_valid").x=1;
//Save current configuration before toutching it.
    {
    std::string experiment_file_in=...;
        ,Constants::elements[Z],data.experiment->variableGet("I").value)
            ;
    data.experiment->save(experiment_file_in.c_str());
    }
```

D.2. Step 1

```cpp
    {
```

76

```
std::string options=string_format("--track-forward␣--output=%s␣--
    ignore-tof␣%s␣>␣/dev/null␣2>&1"
    ,filename_out.c_str(),filename_in.c_str());

double m=1;
for(unsigned int k=0;k<4 && m>fabs(1e-5); ++k)
    {
    data.tracker->commandBuild(*data.experiment,options.c_str());
    fprintf(output,"Starting␣tracker\n{\n%s\n}\n",data.tracker->
        commandGet());
    if(system(data.tracker->commandGet()))
        {
        return 0;
        }
    data.tracker->clear();
    m=getMean(filename_out.c_str(),"h509","fres_ftft");
    fprintf(output,"<m␣%.15g>\n",m);
    double offset=atof(data.experiment->variableGet("OFFSET_FTFT").
        value);
    offset+=m;
    sprintf(data.experiment->variableGet("OFFSET_FTFT").value,"%.15g"
        ,offset);
    remove(filename_out.c_str());
    }

if(m>fabs(1e-5))
    {return 0;}
}
```

D.3. Step 2

```
{
std::string options=string_format("--output=%s␣--track-backward␣%s␣
    >␣/dev/null␣2>&1"
    ,filename_out.c_str(),filename_in.c_str());

double m=1;
for(unsigned int k=0;k<4 && m>fabs(1e-5); ++k)
    {
    if(k)
        {remove(filename_out.c_str());}
    data.tracker->commandBuild(*data.experiment,options.c_str());
    fprintf(output,"Starting␣tracker\n{\n%s\n}\n",data.tracker->
        commandGet());
    if(system(data.tracker->commandGet()))
        {
        return 0;
        }
    data.tracker->clear();

    //By definition fres_gfi1x and fres_gfi2x are 0 when running the
        tracker
    //with --track-backward. Extract them for the sake of consistensy
```

```
      double m_1=getMean(filename_out.c_str(),"h509","fres_gfi1x");
      double m_2=getMean(filename_out.c_str(),"h509","fres_gfi2x");
      double m_3=getMean(filename_out.c_str(),"h509","fres_ftfx");
      data.experiment->objectGet("GFI1").ofs_x+=m_1;
      data.experiment->objectGet("GFI2").ofs_x+=m_2;
      data.experiment->objectGet("FTF").ofs_x+=m_3;
      m=std::max(std::max(fabs(m_1),fabs(m_2)),fabs(m_3));
      fprintf(output,"<m %.15g>\n",m);
      }

  if(m>fabs(1e-5))
    {return 0;}
}
```

D.4. Step 3

```
  {
  double m_have=findPeak(filename_out.c_str(),"h509","fra_A");
  fprintf(output,"<m_have %.15g>\n",m_have);
  double beta_have=getMean(filename_out.c_str(),"h509","fra_beta");
  fprintf(output,"<beta %.15g>\n",beta);
  remove(filename_out.c_str());

  std::string options=string_format("--have=%.15g,%u,%.15g "
    "--want=%.15g,%u,%.15g "
    "--output=%s "
    ">/tmp/tracker-calib-result-%p.txt 2>/dev/null"
    ,m_have,Z,beta
    ,mass,Z,beta
    ,filename_out.c_str()
    ,data.experiment);

  data.tracker->commandBuild(*data.experiment,options.c_str());
  fprintf(output,"Starting tracker\n{\n%s\n}\n",data.tracker->
      commandGet());
  system(data.tracker->commandGet());

  std::string cmdbuff=string_format("/bin/bash -c \"grep beta\\ at -
      A3 "
    "/tmp/tracker-calib-result-%p.txt\" | grep OFFSET",data.
        experiment);

  FILE* new_offsets=popen(cmdbuff.c_str(),"r");
  if(new_offsets==NULL)
    {
    return 0;
    }
  ResourceManager<FILE*,int (*)(FILE*)> rm(new_offsets,pclose);
  ExperimentAbstract* e_clone=data.experiment->clone();
  e_clone->load(new_offsets);
  data.experiment->objectGet("GFI1").ofs_x=e_clone->objectGet("GFI1")
      .ofs_x;
```

```
  data.experiment−>objectGet("GFI2").ofs_x=e_clone−>objectGet("GFI2")
      .ofs_x;
  data.experiment−>objectGet("FTF").ofs_x=e_clone−>objectGet("FTF").
      ofs_x;
  e_clone−>cloneDestroy();
  }
std::string experiment_file_out=...;//Your file for the calibrated
    tracker
  ,Constants::elements[Z],data.experiment−>variableGet("I").value);
data.experiment−>save(experiment_file_out.c_str());

return 1;
}
```

E. Changes Made to RALF'S TRACKER

Before the tracker can be used, changes have to be made to its source code. These changes are made to tell the tracker to skip events which do not fulfill certain conditions. In this Appendix, the modified source file is listed.

In `experiment_specific.hh`:

```
#ifndef EXPERIMENT_SPECIFIC_HH
#define EXPERIMENT_SPECIFIC_HH

#define TRACK_EXP -1          // <—— make sure here is your experiment
    number!!!!
                              //      e.g. 393 for s393

#ifdef EXTEND_EVENT_DATA

#include <cmath>

bool Event_data::init_cuts()
{
  // load your graphical cuts here if needed. Return false if loading
  // failed.
  return true;
}

void Event_data::track_event()
{
  // apply your own cuts here
  // Tpat, incoming, charge (energy) on tof-wall, SSTs, ...
  // leave this function with return; if the event is not good. This
      section
  // could be similar to the following (adjust to your needs):

  // outgoing charge
  if ((Tfmul<1) || (Tfe[0]<10) ) return;

  // *** you might want to keep the stuff below: ***

  // check GFI positions
  if ((Gf1n<1) || (Gf2n<1)) return;
```

```
if (isnan(Gf1x[0]) || isnan(Gf2x[0])) return;
if (Gf1x[0]<-25.0 || Gf1x[0]>25.0 || Gf2x[0]<-25.0 || Gf2x[0]>25.0)
    return;

// check SSTs
if (SS01SMUL==0 || SS02SMUL==0) return;
if (SS01KMUL==0 || SS02KMUL==0) return;

//OK, since calibrating with B14. Used as first guess?
Inz=5;
Inaoverz=14./5.;

//Inbeta is used as start approximation of beta when calibrating the
    FTF (--ignore-tof).
//Use the value from config file.
Inbeta=MY_X("Inbeta");

//outz=5;

//calculate Z from energy range in TFW.
//uses known beta to cheat some more.
if(MY_X("Truebeta_valid"))
  {
  double beta=MY_X("Truebeta");
  double IionE=9.352906073747982e-07;//mean ionization energy (MeV)
  double C_tfw=0.060319339946223; //MeV
  double BConst=C_tfw*(log( 1.022/( IionE*(pow(beta,-2) - 1) ))*pow(
      beta,-2) - 1);
  double Z=sqrt(Tfe[0]/BConst);
  unsigned int Z_int=(unsigned int)( Z + 0.5 );
  if(fabs(Z-Z_int)>0.25)
     {return;}
  outz=Z_int;
  }

// here we assign the chosen hits to the corresponding detector
    planes.
// detectors before aladin (and after target):
track->ftrack_before.set_measured(SS01X(0),SS01Y(0),&sst1,
                                  SS02X(0),SS02Y(0),&sst2);

// detectors after aladin:
track->ftrack_after.set_measured( Gf1x[0]  ,Tfy[0]  ,&gfi1,
                                  Gf2x[0]  ,Tfy[0]  ,&gfi2,
                                  Tfx[0]   ,Tfy[0]  ,&ftf);

T0 = 0;

// track it!
track_fragment(0,0,0,0,0);

}
```

```
#else
   #define EVENT_DATA_OMITTED
#endif

#endif //EXPERIMENT_SPECIFIC_HH
```

F. Energy Depositions for Z

By Equation 5.3, there is a relation between the Z and β of a charged particle passing through a thin detector and its energy loss, but in order to use this relation, the material specific parameters of Equation 5.3, C and I, need to be determined. These parameters were determined for the TFW by observing the amount of energy deposited in the TFW by most particles with $Z \in \{7, 6, 5, 4, 3, 2\}$ and $\beta \approx 0.761$; $Z \in \{5,4,3,2\}$ and $\beta \approx 0.745$; and $Z \in \{8, 7, 6, 5, 4, 3, 2\}$ and $\beta \approx 0.859$. The different Z for a given β come from particles undergoing charge-changing reactions. Regardless of whether the particle changed charge or not, the β at the TFW was assumed to be the same β as the particle of the fired particle. The $\beta \approx 0.761$ simulation was made with ^{20}N, the $\beta \approx 0.745$ simulation with ^{15}B and the $\beta \approx 0.859$ simulation with ^{16}O. The most likely energy deposits for particles of different Z in the mentioned simulations are presented in Table F.1, together with the energies predicted by Equation 5.3 with $C_{\text{TFW}} = 0.060319339946223\,\text{MeV}$ and $I_{\text{TFW}} = 9.352906073747982 \times 10^{-7}\,\text{MeV}$.

These values of C_{TFW} and I_{TFW} were found by minimising the 2-norm of the difference between vectors of the most likely energy deposits in the TFW for a given Z and the values predicted by Equation 5.3. This was done using MATLABs `fminsearch`-function. The MATLAB code used can be found in Section F.2.

With these values for C_{TFW} and I_{TFW}, Equation 5.3 was used to predict the energies that particles of a given Z and β would deposit in the TFW, which in turn was used to determine a best-match Z given the energy the particle deposited and the β of the particle.

In order to verify our method for determining the energy deposition ranges of ions with a given β and Z, an additional simulation with ^{17}C at $\beta = 0.764$ was used. The resulting simulated energy depositions are presented in Figure F.1, and the positions of the peaks corresponding to different Z are presented in Table F.2 alongside the predicted values by Equation 5.3 with the constants delivered from MATLABs `fminsearch`.

F.1. Energy Ranges

From for example Figure F.1, depicting the energy depositions in the TFW, it is clear that particles of a given charge and β mostly deposit their energy the TFW in a narrow range. However, the energy depositions are not wholly restrained to a certain range, and there are several particles depositing energies far away from the predicted peak. This

Table F.1.: *The simulated most likely energy peaks for different Z and β compared to the values given by Equation 5.3 with $C_{TFW} = 0.060319339946223$ MeV and $I_{TFW} = 9.352906073747982 \times 10^{-7}$ MeV. These values where obtained by minimising the 2-norm between the simulated and calculated values with MAT-LABs* ***fminsearch.***

β	Z	Simulated energy (MeV)	Bethe energy (MeV)
0.761	7	70	69.7
0.761	6	52	51.2
0.761	5	36	35.5
0.761	4	22	22.7
0.761	3	12	12.8
0.761	2	6	5.69
0.745	5	36	36.9
0.745	4	23	23.6
0.745	3	13	13.3
0.745	2	6	5.90
0.859	8	74.1	74.3
0.859	7	56.9	56.9
0.859	6	42.0	41.8
0.859	5	29.1	29.0
0.859	4	18.7	18.6
0.859	3	10.1	10.5
0.859	2	4.85	4.65

Table F.2.: *The positions of the peaks for different Z in Figure F.1 presented alongside the calculated values using Equation 5.3 with the values of the constant given by MATLABs* ***fminsearch.*** *Each value is in agreement within 1 MeV, which is considered good enough given the width and spacing of the peaks to predict the energy deposition of fired particles in the TFW.*

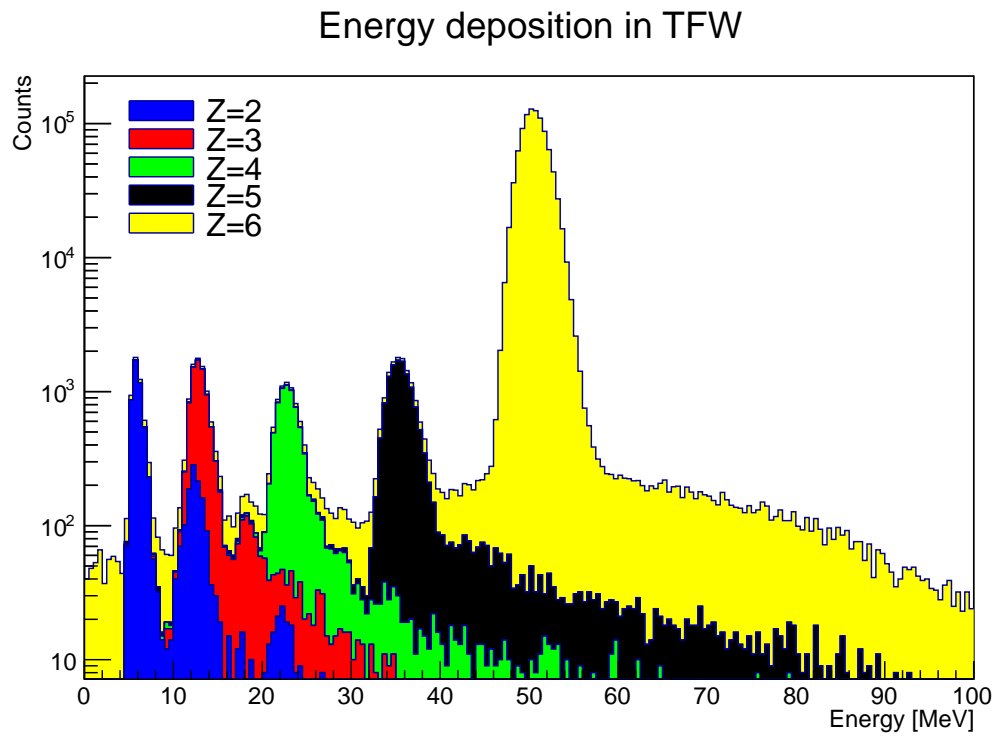| Actual peak	Calculated value
50.6	50.9
35.6	35.3
23.0	22.6
13.0	12.7
5.95	5.65

Figure F.1.: *A stacked histogram of the major energy depositions in TFW for ions of a given charge when ^{17}C were fired with $\beta = 0.764$. The peaks for each Z agree with the energy deposit predicted by Equation 2.4.*

makes it somewhat more difficult to identify charges of individual particles from their energy deposition alone; since the peaks will overlap, mistakes are unavoidable. Because A is determined from the charge-to-mass ratio, this also means that the mass will be incorrectly identified by the tracker in these cases. The amount of incorrectly identified particles can however be minimised by only accepting particles of a given β with energy deposits closely matching integer values of Z. Thus, Z calculated from Equation 5.3 were only accepted if they deviated from an integer value Z_i by less than 0.25, that is, $|Z - Z_i| \leq 0.25$. If so, then Z from Equation 5.3 was identified as Z_i, otherwise the particle responsible for the energy deposition was rejected by the tracker since it could not be identified with sufficient certainty. The value 0.25 was chosen arbitrarily, but was found to yield accurate results without rejecting overly many events. More accurate energy ranges could possibly account for the fact that the peaks are not symmetric, and that particles tend to deposit energy above the peak value.

In all the energy deposition spectra in the TFW when a single particle was fired, the charge of the fired particle can be determined with certainty since particles of that charge give a dominating contribution to the total number of events within it is energy range, as shown in Figure F.1. The charge-changed particles can also be identified, but doing so requires more statistics, as those events are orders of magnitude rarer.

F.2. MATLAB Code

```
%preamble
format long
u=1.6605389e−27;
c=299792458;
e=1.6021765e−19;
brho=10.4;

%function giving beta^2 for a previously defined !!! fixed brho !!!
beta2=@(A,Z)[1./(1+(brho.*Z.*e./(u.*A.*c)).^(−2))];
%Z, A and simulated E−peaks of sim1
Z=[7 6 5 4 3 2];
A=[20 17 18 10 8 6];
E=[70 52 36 22 12 6];
%beta^2 of sim1
bet21=beta2(20,7);
%beta^2 of sim2
bet22=beta2(15,5);

%beta^2 of both sim1 and sim2
bet2all=vertcat(bet21*ones(6,1),bet22*ones(4,1));
%Z of sim2
Z2=[5 4 3 2];
%Z of both sim
Zall=horzcat(Z,Z2)';
%E of sim2
E2=[36 23 13 6];
%E of both sim
```

```
Eall=vertcat(E',E2');

%E of sim3 (more decimals then before since I used to be lazy)
E3=[74.1 56.9 42.0 29.1 18.7 10.1  4.85];
%beta^2 of sim3
bet23=beta2(16,8);
%Z of sim3
Z3=[8 7 6 5 4 3 2];
%all Z, E and beta
Zall=vertcat(Zall,Z3');
Eall=vertcat(Eall,E3');
bet2all=vertcat(bet2all,bet23*ones(7,1));

%function giving predicted energy deposit for these values of Z and beta^2
%with material parameters as argument
h=@(x)[x(1).*(log((1.022./x(2))*1./((1./bet2all)-1)).*(Zall.^2./bet2all)  ...
    - Zall.^2 )];
%initial guess, based on previous experience
x0=[0.8;0.013e-3];
%find optimal material parameters with fminsearch by minimising 2norm of
%calculated and simulated energies
X=fminsearch(@(x)[norm(h(x)-Eall)],x0)
%calculated energies with these parameters
EallCalc=h(X)

%to test the parameters with additional data:
%most likeley energies and Z and beta^2 of sim4
E4sim=[50.6 35.6 23.0 13.0 5.95]';
Z4=[6 5 4 3 2]';
bet24=ones(5,1)*beta2(17,6);
%calculated energies and difference check
E4calc=[X(1).*(log((1.022./X(2))*1./((1./bet24)-1)).*(Z4.^2./bet24) - Z4.^2 )]
E4calc-E4sim
norm(E4calc-E4sim)
```

G. Software Resources

This appendix contains links to and resources on the not-commonly available software products that were used for simulation and analysis during this project. Many of the links are password protected.

G.1. GGLAND

GGLAND can be downloaded by running:
```
export CVS_RSH=ssh
cvs -d :ext:land@lx-pool.gsi.de:/u/johansso/CVS co land02 (17-05-2013)
```
A write-up and some simple examples may be found at: `http://fy.chalmers.se/~f96hajo/ggland/`

G.2. RALF'S TRACKER

The main version of RALF'S TRACKER can be gotten by:
```
git clone land@lx-pool.gsi.de:/u/rplag/tracker (17-05-2013)
```
The version used in this project is a slightly modified version, available at the computer network of the subatomic physics group from:
```
git clone /net/home/htj/tracker.git (17-05-2013)
```
Documentation on how to use the tracker may be found at: `http://ralfplag.de/tracker/` (17-05-2013).

H. Svensk Sammanfattning

H.1. Inledning

Tvärsnittet för en reaktion σ, defineras enligt

$$\sigma = \frac{R}{N\Phi} \quad , \tag{1}$$

där Φ är intensiteten hos den inkommande partikelstrålen ([antal partiklar]/[area × tid]), R är antal reaktioner r per tidsenhet och N är antalet partiklar som bestrålas. Tvärsnittet kan ses som en proportionalitetskontant mellan intensiteten hos strålen och antalet reaktioner normerat med antalet bestrålade partiklar. Ett exempel på en reaktion skulle kunna vara att en atomkärna absorberar en extra neutron då den bestrålas av neutroner, eller att kolliderande kärnor fusioneras. Tvärsnitten för sådana reaktioner är av stort intresse, då de kan förklara hur de olika grundämnena uppstår och varför de finns i de proportioner som de gör.

För att räkna ut absoluta tvärsnitt för kärnreaktioner krävs det att antalet reaktioner kan räknas. Detta görs genom att detektera produkterna av dessa reaktioner. För att ta hänsyn till att inte alla produkter kan detekteras, defineras acceptansen α hos en uppställning som

$$\alpha = \frac{\mathrm{E}[N_{\text{detekterade händelser}}]}{\mathrm{E}[N_{\text{händelser}}]}, \tag{2}$$

med vilken det går att kompensera för att inte allting detekteras. Då antal händelser inte är känt i praktiken krävs det i regel simuleringar för att bestämma α.

Denna kandidatarbetesrapport beskriver Monte-Carlo-simuleringar av delar av *S393*-experimentet som har utförts vid *GSI Helmholtz Centre for Heavy Ion Research* i tyska staden Darmstadt. Huvudfokus har legat på hur bra analysverktygen beter sig under olika omständigheter. Testfallen har varit enstaka joner, som från strålmålets position avfyrats frammåt med en magnetisk rigiditet på 8,8 Tm.

En del av analysen består i att finna partiklars väg, massa och laddning. Det har undersökts hur många detektorhändelser som identifierats korrekt och om det finns några situationer där detta inte går. En viktig del av experimentuppställningnen är ett magnetfält, som ser till så att laddade partiklar avviker från sin ursprungliga väg.

Ett resultat som presenteras är hur väl experimentuppställningen tillsammans med analysverktyg kan identifiera frammåtgående joner om skillnaden mellan det riktiga

magnetfältet och det magnetfält som används i analysen varierar. Ett annat resultat beskriver hur utgångsvinkeln mellan partikelbanan och strålaxeln påverkar mängden detekterade partiklar.

Vid sidan om ovannämnda resultat, presenteras också resultat i form av detektordefinitioner, som skapades inom ramen för detta projekt. Dessa definitioner har genomgående använts i, och var nödvändiga för, simuleringarna som genererade den data som analyserades.

H.2. Kort om detektorprinciper

Det finns olika typer av detektorer. I projektet har främst så kallade scintillatorer simulerats. I en sådan blir valenselektronerna närmast den passerande partikeln händelsevis exciterade till en högre energinivå [5]. De exiterade elektronerna kommer tillslut att återgå till ledningsbandet via spontan relaxation varpå en foton emitteras. På grund av ytterligare energinivåer orsakade av materialdefekter mellan banden, kan elektroner återgå i flera steg med energier som inte kan excitera elektroner i valensbandet. De sistnämnda elektronerna har därför låg sannolikhet att absorberas. Istället kan elektronerna detekteras med hjälp av en fotomultiplikator, vilket skapar en elektrisk signal [5].

Från energiprincipen följer att laddade partiklar som passerar detektormaterialet måste deponera energi lika stor som den energi som används till att excitera elektronerna, varför energidepositionen från partikeln kan mätas [5].

H.3. *S393*-Experimentet

I figur H.1 presenteras en schematisk bild av experimentuppställningen i *Cave C* med ingående detektorer.

Instabila joner kommer in i *Cave C* från FRS[1], där de skapats i kollisioner och filtrerats beorende på deras laddning och massa via magnetfält och *degraders*. De inkommande jonernas hastighet bestäms genom att en timer som startats i FRS stoppas då jonerna passerar POS[2]. En ny timer startas även då jonerna åker igenom POS.

Efter att jonerna passerat POS kommer de till ROLU[3], som består av fyra scintillatorplattor som definerar en öppning för strålen att åka igenom. Om strålen blir för ofokuserad detekterar ROLU detta och skickar en signal, som säger åt systemet att inte lagra data kring tillhörande händelser.

Efter ROLU går strålen in i XB[4]-detektorn. Denna detektor består av pentagonala och hexagonala NaI-kristaller placerade i ett sfärisk skal, med öppningar för inkommande stråle och framåtgående produkter.

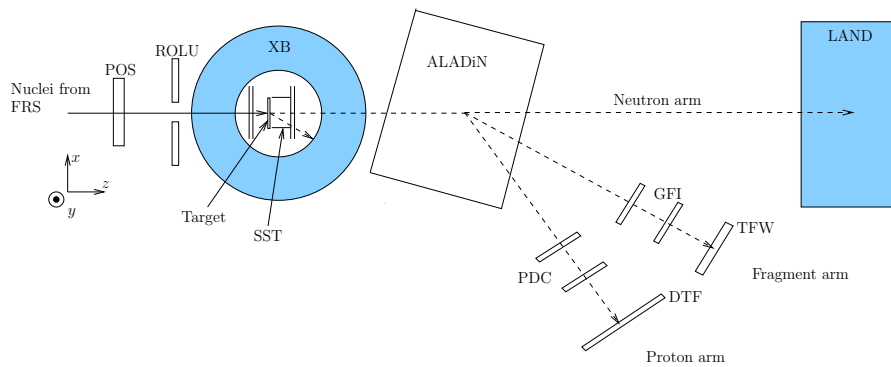Inuti XB omringas strålmålet av 8 SST[5]:er. Dessa kan användas tillsammans med

---

[1]FRagment Separator
[2]POSition
[3]Rechts, Oben, Links, Unten
[4]Crystal Ball
[5]Silicon STrip detector

Figur H.1.: *Experimentuppställningen för* S393 *i* Cave C *vid* GSI *[7]. Strålen med joner kommer från vänster (från FRS) och träffar strålmålet (Target) innanför detektorn XB. Resulterande partiklar detekteras sedan antingen av XB, eller separeras beroende på laddning av ett magnetfält innuti ALADiN och detekteras i de olika* armarna. *Alternativt detekteras de inte alls. De i fyllda hindrena definerades i* GGLAND *som en del av detta arbete.*

varandra eller XB beroende på vilken riktning SST:n är i, för att bestämma infallsvinkeln hos strålen och utgående vinklar hos produkterna.

De produkter som lämnar XB i framåtriktningen når ALADiN[6]. ALADiNs magnetfält får produkterna att böja av beroende på kvoten mellan deras massa och laddning. Detta får produkterna att åka in i en av tre olika *armar*:

- Protoner som har ett lågt förhållande mellan massa och laddning påverkas starkt av magnetfältet. På grund av detta hamnar de i PCD[7]:erna. Dessa består av en uppsättning laddade vertikala och horisontella trådar vilka genererar ett elektriskt fält som gör det möjligt att detektera laddade partiklar genom att samla in frigjorda elektroner i deras väg. Efter PDC:erna träffar protonerna DTF[8], som är en scintillator.

  Efter dessa når protonerna DTF[9], vilken mäter x och y positionen hos protonerna samt stoppar den timer som startats av POS, vilket ger medelhastigheten genom uppställningen hos de enskilda protonerna.

- De tyngre laddade produkterna hamnar i fragment-armen, där de träffar de två GFI[10]:erna. Dessa består av vertikala parallella scintillator-fibrer, vilka kan ge en x-position för fragmenten.

  Efter detta träffar de TFW[11], vilken består av två plan av parallella scintillator

---

[6]A LArge DIpole magNet
[7]Proton Drift Chamber
[8]Dicke ToF-wall
[9]Dicke ToF-wall
[10]Großer FIberdetektor
[11]Time of Flight Wall

plattor, vridna 90° grader relativt varandra. Denna detektor ger x, y samt energi-depositionen, och stoppar timern startad av POS, vilket ger medelhastigheten för enskilda fragment genom uppställningen.

- Neutroner, som är oladdade, böjs inte av av magnetfältet och fortsätter rakt fram in i LAND[12], där de detekteras och en POS-timern stoppas för att ge deras medelhastighet.

Detta beskriver hur experimentuppställningen idealt ska fungera. I verkligheten beter sig laddade partiklar stokastiskt, och på grund av växelverkan med till exempel luften kommer de inte att åka helt rakt. Detta är anledningen till att experimentet behöver simuleras.

H.4. Mjukvara

För att utföra simuleringarna användes GEANT4 tillsammans med en wrapper, GGLAND. Detaljer om dessa återfinns i avsnitt H.4.1 och avsnitt H.4.2. Datan analyserades med RALF'S TRACKER och ROOT, vilka presenteras i avsnitt H.4.3 avsnitt H.4.4.

H.4.1. GEANT4

GEANT4 är ett toolkit för att simulera växelverkan av partiklar med materia. De fysikaliska processer och tillhörande modeller som en simulering ska ta hänsyn till defineras i GEANT4 av en *physics list*, vilket ger vilkor och sannolikheter för att vissa fysikaliska processer ska inträffa. Vid en simulering slumpar GEANT4 fram tider då olika händelser inträffar utgående från dessa modeller, och om partikeln i simuleringen är kvar då denna tid inträffar så inträffar händelsen. I våra simuleringar användes *physics list*:an *QGSP_BERT*, vilken är standardalternativet i GGLAND.

H.4.2. GGLAND

Då GEANT4 är väldigt allmän krävs det mycket arbete för att få GEANT4 att simulera ett specifikt experiment, varför det är önskvärt att använda en wrapper. GGLAND är ett kommandoradsverktyg, som använder GEANT4, för simulering av subatomära partikelexperiment [16]. GGLAND låter användaren snabbt ställa upp vissa typer av vanliga simuleringar genom att användaren kan placera ut fördefinierade hinder[13] och simulera av användaren specifierade spektrum av partiklar mot dessa. Vidare går det att modifiera mått på definierade hinder via kommandoraden. När detta inte räcker till kan helt egna hinder specifieras i en modul som placeras i GGLAND:s källkodsträd. Som utdata genererar GGLAND filer som kan analyseras med samma metoder som verkliga experimentdata.

---

[12]Large Area Neutron Detector
[13]Ett hinder är en del av experimentuppställningen som en partikel måste passera.

H.4.3. RALF'S TRACKER

RALF'S TRACKER är ett program som försöker återskapa partikelbanor (*tracks*) genom att kombinera data ifrån enskilda detektorer. Dessa partikelbanor används sedan för att bestämma andra egenskaper hos partiklarna. Detta görs i princip genom att lösa rörelseekvationen för laddade partiklar genom ALADiNs magnetfält och försöka hitta den bana som ger minst avvikelse från de experimentellt uppmäta positionerna i detektorerna. Detta ger kvoten mellan en partikels massa och laddning. För att få massan och laddningen räcker det således med att utöver detta bestämma partikelns laddning, vilket kan göras med Bethes formel och energidepositioner i en detektor. För att göra allt detta behöver RALF'S TRACKER även partikelns hastighet, vilket den kan få genom tiden det tar för partikeln att nå TFW.

För att spåra partiklar ges RALF'S TRACKER information om experimentuppställningen i en konfigurationsfil. För att få indatan att stämma bra med det trackern beräknar kan trackern tillåtas manipulera sin experimentuppställning, vilket görs då den kalibreras. Detta kan motiveras med att det inte går att få perfekt information om den verkliga experimentuppställningen, varpå trackern försöker lista ut denna från sin indata under kalibrering.

H.4.4. ROOT

För att analysera den stora mängden data som simuleringarna och RALF'S TRACKER genererar används det för ändamålet framtagna C++-ramverket ROOT. ROOT är framtaget för att hantera de stora datamängder som är typiska för experiment inom subatomär fysik. Vidare kan både GGLAND och RALF'S TRACKER ge utdata i form av ROOT-filer, varför det är lämpligt att använda ROOT.

H.5. Simulering

Den delen av figur H.1 som simulerats är de två SST:erna efter strålmålet, ALADiN samt fragmentarmen. Detta möjliggör undersökandet av hur olika framåtgående fragment kan detekteras givet förutsättningarna i simuleringen. I Table H.1 presenteras placeringen av de olika detektorerna i simuleringen.

Vid simuleringarna användes ALADiN med en ström på $I = 2500\,\mathrm{A}$, vilket är den högsta ström för vilken magnetfältet uppmätts. Detta svarar ungefär mot den ström som användes vid det faktiska experimenten. För att få partiklarna att träffa fragmentarmen avfyrades de iväg med en magnetisk rigiditet på $b\rho = 8{,}8\,\mathrm{Tm}$, vilket ungefär svarar mot att partiklarna träffade GFI1, GFI2 och TFW i mitten.

Nedan presenteras vad som avfyrades i olika simuleringar och vad som undersöktes i dessa simuleringar:

- Olika partiklar avfyrades med en slumpmässig spridningsvinkel $\alpha \leq 8°$ från z-axeln. Detta för att undersöka hur olika spridningsvinklar påverkar uppställningens förmåga att detektera partiklar samt RALF'S TRACKERs förmåga att analysera resultaten. Endast en sorts partikel användes per simulering.

- Olika $5 \leq Z \leq 9$ joner avfyrades med en slumpmässig vinkel $\alpha \leq 0{,}016$ rad från z-axeln. Detta användes för att undersöka hur ofta RALF'S TRACKER korrekt kan identifiera olika partiklar beroende på med vilken ALADiN ström den kalibrerats. Endast en sorts partikel användes per simulering.

Den analys som gjordes på de olika simuleringarna presenteras i avsnitt H.6. Resultaten för de olika simuleringarna efter analys återfinns i avsnitt H.7.

H.5.1. Kalibrering av RALF'S TRACKER

Trackern kalibererades för fragment i den grad det var möjligt enligt den procedur som finns beskriven på trackerns hemsida [18]. Då proton- och neutronarmen inte simulerats kunde inte vinkel kalibreras, varför detta steg hoppades över. Kalibreringen gjordes med indata från en simulering då ^{14}B med $b\rho = 8{,}8$ Tm avfyrades från strålmålets position i z-axelns riktning med en spridning på $0{,}016$ rad och ALADiN hade en ström på $I = 2500$ A. Utöver detta gavs trackern andra ALADiN strömmar än den som använts i simuleringen, detta för att med facit i hand undersöka hur osäkerheter i ALADiNs magnetfält påverkar trackerns förmåga att efter kalibrering identifiera olika partiklar. Vidare gavs trackern Z hos partikeln som användes för kalibrering.

Kalibreringen kan kort beskrivas enligt följande:

1. Tracka i *forward*-läge med avfyrade partikelns β givet till trackern för att se hur tiden för att nå TFW enligt trackern skiljer sig från tiderna i indatan. Addera medelvärdet av denna skillnaden som kompensering och iterera tills felet blivit litet.

2. Tracka i *backward*-läge och låt trackern denna gång avgöra hastigheten från tiden det tar att nå TFW. Addera medelvärdet av avvikelsen mellan den trackade x-koordinaten för energidepositioner i TFW och den i indatan och iterera tills felet är litet.

Tabell H.1.: *Hinderplacering använd vid simulering. Placeringen är given som (x, y, z)-koordinater relativt strålmålet. Rotationen ges med avseende på hindrens negativa y-axel.*

Hinder	Placering/cm	Rotation/grader
ALADiN	$(0, 0, 255)$	7
FTF	$(-232{,}94, 0, 1124.33)$	15
GFI1	$(-56{,}94, 0, 467.504)$	15
GFI2	$(-72{,}469, 0, 525.450)$	15
SST1	$(0, 0, 11)$	0
SST2	$(0, 0, 14)$	0

3. Notera toppen i masspektrumet som trackern gav från den tidigare gjorda simuleringen. Detta är massan trackern identifierat. Låt trackern köra en simulering med denna massa och med den faktiska massan hos den avfyrade partikeln. Trackern kan sedan ges instruktioner för att flytta detektorerna i sin uppställning för att få en partikel med den korrekta massan att träffa detektorerna på samma ställen som partikeln med den identifierade massan har träffat.

När trackern är kalibrerad kommer den således ha en annan experimentuppställningen än den som användes i simuleringen. Med denna experimentuppställning kommer partikeln som trackern kalibrerats för, trots felaktig ALADiN ström, att få den track som bäst matchar indatan.

H.6. Analys

En träff är i föreliggande arbete definerat som det kluster av energidepositioner grupperade av GGLAND som tillsammans gav den största energidepositionen. Denna definition görs då laddade partiklar som färdas genom ett medium joniserar närliggande atomer och därför ger upphov till sekundära partiklar i form av frigjorda elektroner kring partikelns spår. Då dessa elektroner oftast deponerar mindre energi än den primära partikeln kan deras bidrag filtreras genom att bara betrakta den största gruppen av depositioner.

Den primära partikelns typ kan sedan fås från GGLANDs utdata genom att se vilken sorts partikel som gav största bidraget till den primära energidepositionen.

H.6.1. Vinkelberoende hos detekterade händelser

För att få beroendet mellan detekterade händelser och vinkeln α, definerat som vinkeln mellan utgående fragmentets ursprunliga riktning och strålaxeln, görs ett histogram med $\cos \alpha$ mot antal träffar i detektorerna. Detta kan göras med vilkor för vilka typer av partiklar som ska ha detekterats samt vilken mängd energi som ska ha deponerats.

För att se hur bra trackern är på att identifiera olika partiklar utnyttjas GGLANDs förmåga att rapportera vilken partikel som ger största bidraget till den primära depositionen.

H.6.2. Utvärdering av trackerkalibrering

Hur bra en kalibrering är utvärderas genom hur bra den är på att identifiera partiklar korrekt. För att kunna testa detta kördes simulering på isotperna i mängden

$$S_B = \{^{10}\text{B}, ^{11}\text{B}, ^{12}\text{B}, ^{13}\text{B}, ^{14}\text{B}, ^{15}\text{B}, ^{17}\text{B}, ^{19}\text{B}\}$$

med en ström $I_0 = 2500\,\text{A}$ och ett $b\rho = 8.8\,\text{Tm}$. Orsaken till att isotoperna ^{16}B och ^{18}B exkluderades är att dessa är obundna.

Efter simuleringarna kalibrerades trackern med data från simuleringen av ^{14}B. Trackern kalibrerades åtta gånger, med åtta olika strömmar till trackern. De strömmar som användes var 2500 A, 2462,5 A, 2425 A, 2387,5 A, 2350 A, 2312,5 A, 2275 A, and 2237,5 A,

där strömmen $I_0 = 2500\,\text{A}$ är den ström som användes vid simulering och de övriga strömmar listats med ett stigande fel. För varje ström skapades en kalibreringsprofil.

Givet de skapade kalibreringsprofilerna spårades utdata från simuleringarna för alla isotoper i S_B. Detta gjordes för varje kalibreringsprofil. Kalibreringsprofilerna som skapats för S_B användes också för olika atomnummer med ett fixt masstal. Isotoperna ^{22}C , ^{22}N och ^{22}F simulerades och spårades.

Avvikelser kan också inträffa när trackern har kalibrerats men ges data insamlad vid en annan ström än den som användes vid kalibreringsförsöket. Därför gjordes simuleringar för alla isotoper i S_B med strömmen $I_{\text{sim}} = 2300\,\text{A}$. Sedan spårades utdata med samtliga kalibreringsprofiler fast med en ström

$$I_t = I_c \left(1 - \frac{I_0 - I_{\text{sim}}}{I_0} \right) \quad , \tag{3}$$

där I_c är den ström som skickades till trackern vid kalibrering och I_0 den ström som användes för att generera data till kalibreringen.

H.7. Resultat

H.7.1. Vinkelberoende hos detekterade händelser

I figur H.2 presenteras resultatet från en simulering där $2^{20}\,stycken$ ^{14}B avfyrats med $b\rho = 8.8\,\text{Tm}$ och en maximal spridningsvinkel α på $8°$. Figuren illustrerar hur antalet avfyrade partiklar som uppfyller olika vilkor varierar med avseende på vinkeln.

I figur H.3a visas antalat partiklar som gav upphov till energidepositioner överskridande vissa tröskelvärden i olika detektorer. Låga tröskelvärden i förhållande till de mest troliga energidepositionerna i de olika detektorerna visar sig inte förstöra vinkelberoendet i antalet detekterade händelser.

Figur H.3b visar antalet partiklar som ger upphov till träffar i de olika detektorerna för olika $\cos\alpha$. Ifrån detta verkar det som att GFI2 är den detektorn som partiklarna börjar missa först.

Då partiklar kan missa olika detektorer före andra kan de olika spårningsmetoderna användas för olika mängder av partiklar. Partiklar som kan spåras med de olika metoderna visas i figur H.3c, där det syns att flera partiklar kan trackas med framåtspårning.

Slutligen visar figur H.3d den andel primära energidepositioner i TFW som tillskrivs olika partiklar för olika $\cos\alpha$. Från denna figur är det tydligt att en andel av de ^{14}B som avfyras når TFW som andra fragment, samt att främst elektroner når TFW för stora α.

Med simuleringsresultaten som bakgrund kan trackern utvärderas genom att jämföra dess resultat med simuleringens. Trackerns förmåga att identifiera partiklar avfyrade vid olika vinklar presenteras i figur H.3. De olika figurerna visar bland annat antal korrekt identifierade partiklar för olika vinklar givet extra filter med avseende på energidepositioner i olika detektorer, svarande mot olika histogram i figur H.3a. I figur H.3d visas

antal identifierade partiklar med det striktare vilkoret att $|A - 14| < 0{,}1$ för att en partikel ska anses vara korrekt identifierad. Med detta vilkor identifierar trackern avsevärt färre partiklar vid stora α.

H.7.2. Inverkan av felaktig ström hos partikelspårning

I figur H.4 visas resultatet när olika kalibreringsprofiler har använts på utdata från simuleringar med strömmen $I_0 = 2500\,\text{A}$ för isotoperna i S_B, som definieras i avsnitt H.6.2. Det är tydligt att alla istotoper har identifierats korrekt och att absolutbeloppet av massavvikelsen är mindre än $0{,}04\,\text{u}$. Man ser även att massavvikelsen tycks öka när A ökar.

Genom att försöka spåra utdata från simulering med $A = 22$ och $Z \in \{6, 7, 8, 9\}$ vid samma ström, erhölls resultatet i figur H.5. Även i detta fall har samtliga isobarer identifierats korrekt med en maximal massavvikelse mindre än $0{,}06\,\text{u}$.

När annan ström användes vid simulering och trackern körs på genererade utdata med de tidigare kalibreringsprofilerna och en ström som beräknats enligt ekvation 3 erhölls resultatet i figur H.6. Även i detta fall har samtliga isotoper identifierats korrekt men nu överstiger absolutbeloppet av massavvikelsen $0{,}09\,\text{u}$.

Som illustreras i figur H.7 flyttar trackern detektorerna under kalibrering på ett sätt som gör att linjen från ALADiNs mitt genom detektorernas, roteras med en vinkel som kompenserar för avvikelsen i ström. Vinkeln har beräknats enligt

$$\theta_{\text{off}} = \arctan\left(\frac{x_{\text{off}}}{z_{\text{dist}}}\right) \tag{4}$$

Eftersom trackern enbart ändrar detektorernas x-koordinat (i detektorsystemet) blir armen något längre eller kortare, och själva detektorerna roteras inte. Denna inverkan hos en inkorrekt ström stämmer överrens med vad Ralf Plag har presenterat på *S393/land02 Workshop 2011* [17].
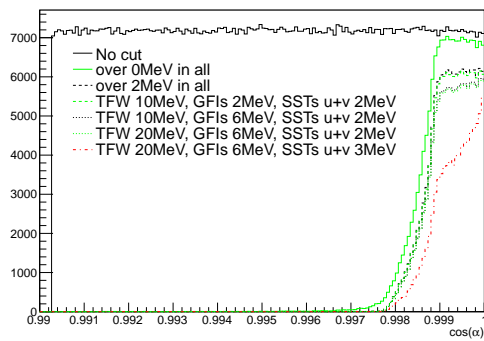
H.8. Diskussion

H.8.1. Spridning och antalet träffar

Som synes i figur H.3 och figur H.2 lyckas trackern korrekt identifiera stora delar av de avfyrade ^{14}B som alla träffar de detektorer som används för fragment-identifiering. En del av de partiklar den inte lyckas identifiera kan också tillskrivas till det faktum att alla ^{14}B som avfyras inte når TFW som ^{14}B.

I figur H.3b syns det att GFI2 är den detektor som missas för minst vinkel, vid $\alpha \approx 2{,}5°$. Detta svarar mot vinkeln då antal partiklar trackern lyckas rekonstruera minskar, varför det verkar som att partiklar som missar GFI2 är orsaken till att trackern ofta inte kan identifiera partiklar med $\alpha > 2{,}5°$.

Något som inte lyckats förklaras är varför antal partiklar som träffar TFW:n inte uppvisar samma beteende som de som träffar de andra detektorerna. Övergången mellan
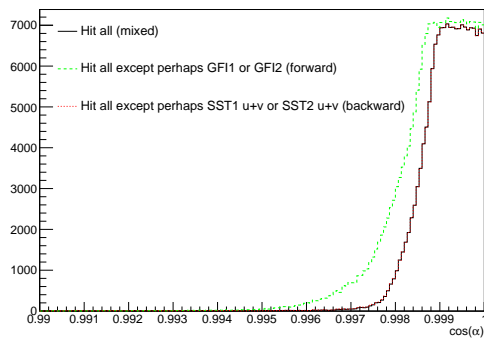
Figur H.2.: *Antal partiklar i en simulering där 2^{20} ^{14}B avfyrats med $b\rho = 8,8\,\mathrm{Tm}$ och en spridningsvinkel α på $8°$ för olika $\cos\alpha$ som...*
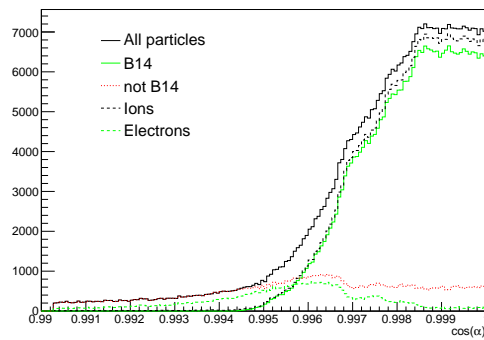

(a) ...orsakade energidepositioner över visa värden i alla detektorer. "No cut" visar alla avfyrade partiklar.
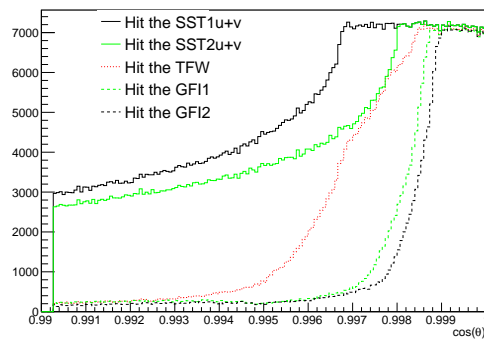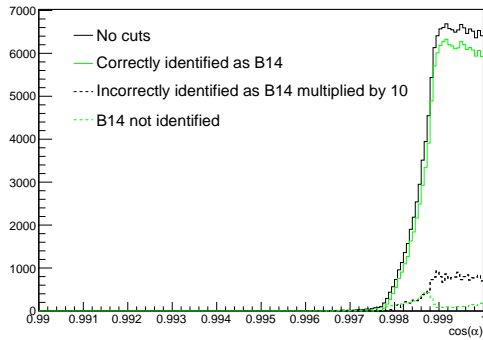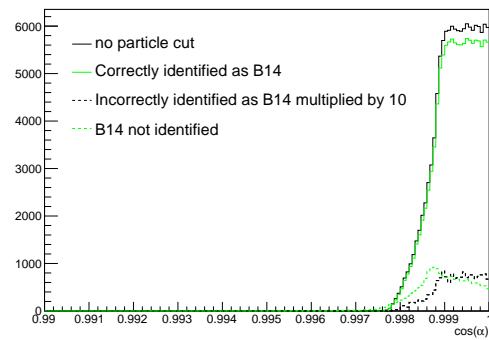

(b) ...träffade de olika detektorerna.

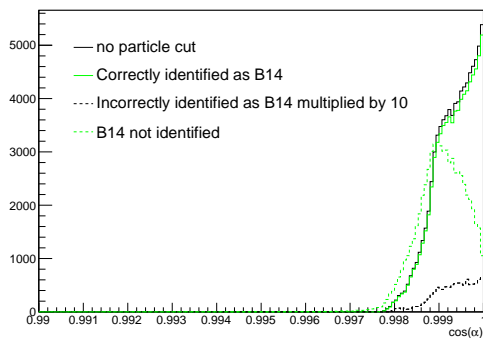(c) ...vore möjliga att tracka med de olika track-metoderna i RALF'S TRACKER.

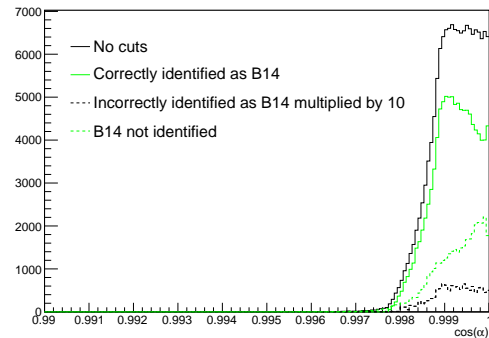(d) ...orsakad primära energidepositionerna till-skrivna olika partiklar.

(a) Över 0 MeV i alla detektorerna

(b) Över 2 MeV i alla detektorerna

(c) Över 20 MeV i TFW, 6 MeV i GFI:erna 3 MeV i SST:erna (u+v)

(d) Över 0 MeV i alla samt $|A-14| < 0.1$

Figur H.3.: *Antal av RALF'S TRACKER identifierade partiklar från en simulering där 2^{20} ^{14}B avfyrats med $b\rho = 8{,}8$ Tm och en spridningsvinkel på $8°$ för olika $\cos\alpha$. Olika underfigurer visar hur trackern presterade då händelser ytterligare filtrerats. "B14 not identified" histogramet inkluderar ^{14}B som uteslutits av dessa extra filter. Energi filtreringarna i de olika delfigurerna svarar mot de olika histogrammen i figur H.3a. Underfigur (d) är med ett striktare vilkor för att A ska anses vara korrekt identifierat, i övrigt användes vilkoret $|A-14| < 0{,}5$.*
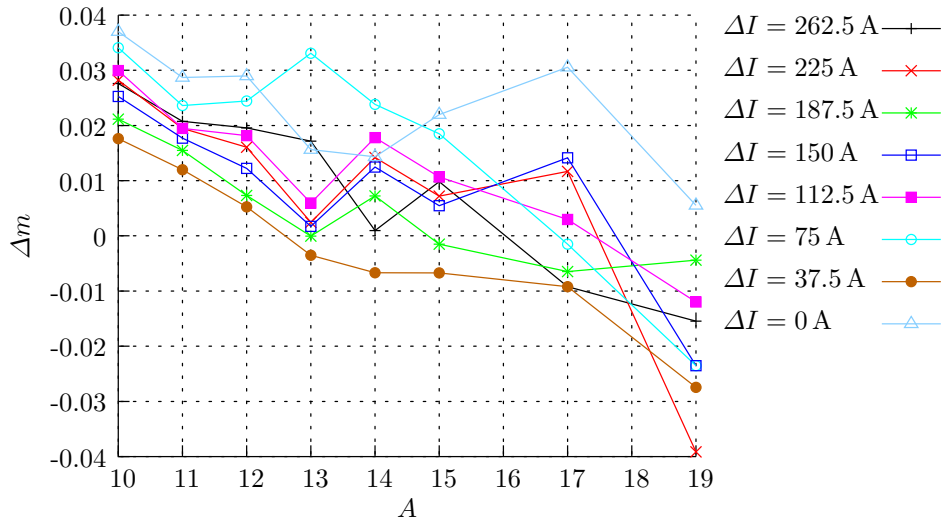
Figur H.4.: *Massavvikelse mellan simulerad och spårad massa för $Z = 5$ som funktion av A för olika $\Delta I = I_0 - I_c$. Resultatet erhölls genom att köra trackern med samtliga kalibreringsprofiler på utdata från simulering vid samma ström som användes vid kalibrering. Storheterna I_0 och I_c definieras i avsnitt H.6.2.*
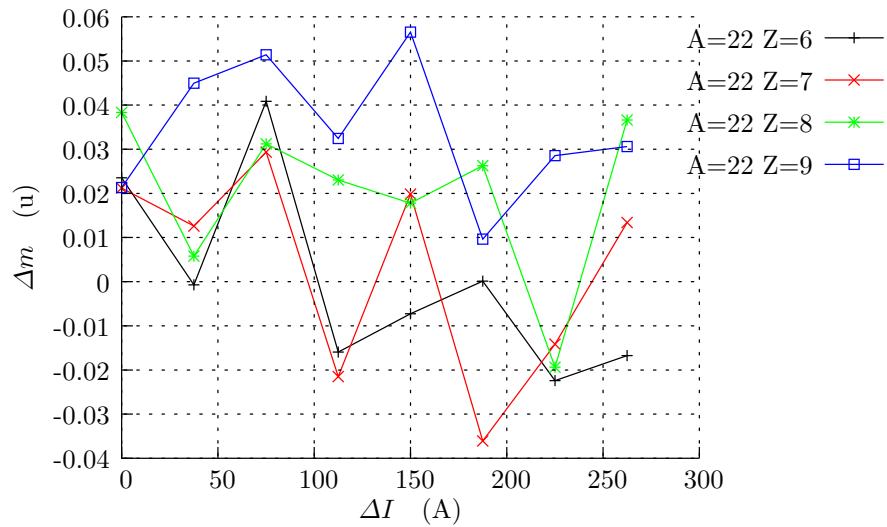
Figur H.5.: *Massavvikelse mellan simulerad och spårad massa för $A = 22$ och olika Z funktion av $\Delta I = I_0 - I_c$. Resultatet erhölls genom att köra trackern med samtliga kalibreringsprofiler på utdata från simulering vid samma ström som användes vid kalibrering. Storheterna I_0 och I_c definieras i avsnitt H.6.2*
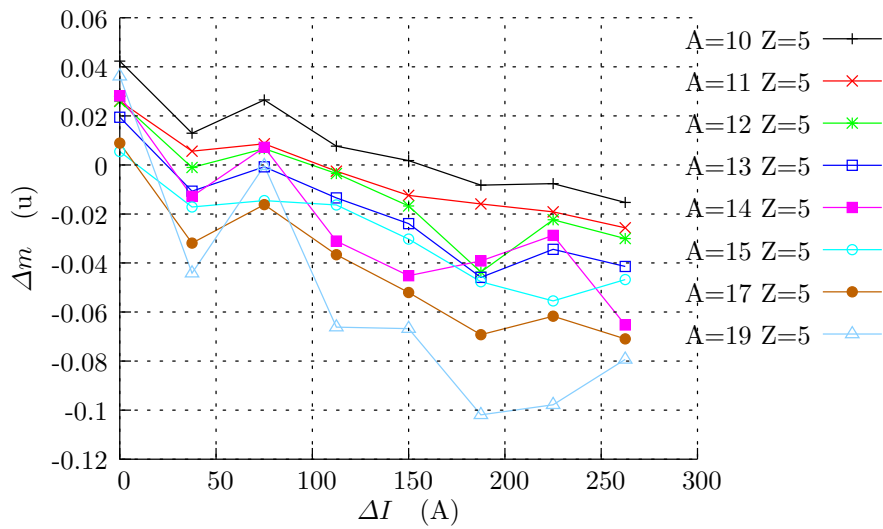
Figur H.6.: *Massavvikelse mesllan simulerad och spårad massa för olika A och Z = 5 som funktion av $\Delta I = I_0 - I_c$. Simuleringarna gjordes med en ström på 2300 A och strömmen som skickades till trackern beräknades ur ekvation 3. Storheterna I_0 and I_c definieras i avsnitt H.6.2.*
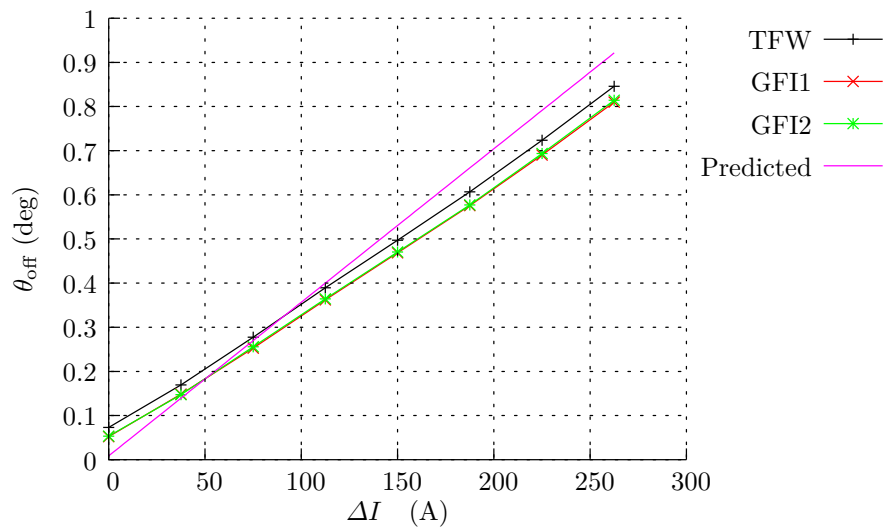
Figur H.7.: *Fragmentarmens rotation efter kalibrering som funktion av $\Delta I = \Delta I = I_0 - I_c$. Rotationsvinkeln har beräknats ur ekvation 4. Linjen "Predicted" är den beräknade skillanden mellan vinkeln för utgående fragment och fragmentarmens vinkel vid efter kalibrering vid felaktig ström. Storheterna I_0 och I_c definieras i avsnitt H.6.2.*

att partiklar missar och träffar TFW:n är mycket mjukare än för GFI:erna. Förklaringar skulle kunna vara att ALADiNs magnetfält får partiklar att inte nå den avlägsna TFW:n.

H.8.2. Kompensering för inkorrekt kalibreringsström

Trackern lyckas kompensera för felaktiga strömmar under kalibreringen genom att flytta på detektorerna i fragmentarmen på ett sätt som ungefär svarar mot att rotera armen kring ALADiNs centrum, vilket ses i figur H.7. Detta medför visa fel, förutom i detektorpositioner. För det första kommer inte detektorerna vara riktade mot ALADiNs mitt, vilket förstör strålens skärning med detektorerna något. För det andra blir armen lite längre. Dessa effekter är dock små för de ΔI som undersökts, och ger inte upphov till fel stora nog för att orsaka att partiklar felidentifieras.

Det faktum att trackern flyttar detektorerna till felaktiga positioner kanske utgör ett problem, även om det inte påvisats i de simuleringar vi har utfört. Det vore då kanske bättre att korrigera för strömmen istället. En indikation på att så vore fallet är om trackern flyttar detektorerna så att arctan (`x förflyttning`/`avstånd från ALADiN`) är lika för de olika detektorerna. Om så är fallet bör förflyttningen inte utföras, utan istället bör ett nytt I för trackern beräknas.